A FINITE VOLUME METHOD FOR THE ANALYSIS OF THE THERMO-FLOW FIELD OF A SOLAR CHIMNEY COLLECTOR

Johannes Henricus Meiring Beyers

Thesis presented in partial fulfillment of the requirements for the degree of Master of Engineering at the University of Stellenbosch

Thesis supervisors:
Doctor T.M. Harms
Department of Mechanical Engineering

Professor D.G. Kröger
Department of Mechanical Engineering

December 2000

DECLARATION

I, Johannes Henricus Meiring Beyers, the undersigned, hereby declare that the work contained in this thesis is my own original work and that I have not previously, in its entirety or in part, submitted it at any university for a degree.

ABSTRACT

This study investigates the implementation of the finite volume numerical method applicable to non-orthogonal control volumes and the application of the method to calculate the thermo-flow field within the collector area of a solar chimney power generating plant. The discretisation of the governing equations for the transient, Newtonian, incompressible and turbulent fluid flow, including heat transfer, is presented for a non-orthogonal coordinate frame. The standard $k-\varepsilon$ turbulence model, modified to include rough surfaces, is included and evaluated in the method.

An implicit solution procedure (SIP-semi implicit procedure) as an alternative to a direct solution procedure for the calculation of the flow field on non-staggered grids is investigated, presented and evaluated in this study. The Rhie and Chow interpolation practice was employed with the pressure-correction equation to eliminate the presence of pressure oscillations on non-staggered grids.

The computer code for the solution of the three-dimensional thermo-flow fields is developed in FORTRAN 77. The code is evaluated against simple test cases for which analytical and experimental results exist. It is also applied to the analysis of the thermo-flow field of the air flow through a radial solar collector.

KEYWORDS:
NUMERICAL METHOD, FINITE VOLUME, NON-ORTHOGONAL, $k-\varepsilon$ TURBULENCE MODEL, SIP

OPSOMMING

Die studie ondersoek die implementering van 'n eindige volume numeriese metode van toepassing op nie-ortogonale kontrole volumes asook die toepassing van die metode om die termo-vloei veld binne die kollekteerder area van 'n sonskoorsteen krag aanleg te bereken. Die diskretisering van die behoudsvergelykings vir die tyd-afhanlike, Newtonse, onsamedrukbare en turbulente vloei, insluitende hitteoordrag, word beskryf vir 'n nie-ortogonale koordinaatstelsel. Die standaard $k-\varepsilon$ turbulensiemodel, aangepas om growwe oppervlakrandvoorwaardes te hanteer, is ingesluit en geevalueer in die studie.

'n Implisiete oplossings metode (SIP-semi implisiete prosedure) as alternatief vir 'n direkte oplossingsmetode is ondersoek en geimplimenteer vir die berekening van die vloeiveld met nie-verspringde roosters. 'n Rhie en Chow interpolasie metode is gebruik tesame met die drukkorreksie-vergelyking ten einde ossilasies in die drukveld in die nie-verspringde roosters te vermy.

Die rekenaarkode vir die oplossing van die drie dimensionele termo-vloeiveld is ontwikkel in FORTRAN 77. Die kode is geevalueer teen eenvoudige toetsprobleme waarvoor analitiese en eksperimentele resultate bestaan. Die kode is ook gebruik om die termo-vloeiveld binne 'n radiale son kollekteerder te analiseer.

SLEUTELWOORDE:
NUMERIESE METODE, EINDIGE VOLUME, NIE-ORTOGONAAL, $k-\varepsilon$ TURBULENSIE MODEL, SIP

DEDICATION

To my parents

ACKNOWLEDGEMENTS

I would like to thank the following persons for their contributions during the course of this study:

Dr. T.M Harms, as supervisor and teacher, for his advice, support and patience.

Professor D.G. Kröger, as supervisor, for suggesting this thesis and his essential guidance.

CONTENTS Page

LIST OF SYMBOLS

Symbols

Component of $\vec{A}$	A
Influence coefficient matrix	A
Adjugate Jacobian matrix	A
Interfacial surface area vector	$\vec{A}$
Influence coefficient	a
Pressure correction influence coefficient	a^p
Empirical constant	B
Control volume corner vectors	$\vec{C}$
Specific heat	C_p
$k - \varepsilon$ turbulence model constant	C_μ
$k - \varepsilon$ turbulence model constant	$C_{\varepsilon 1}$
$k - \varepsilon$ turbulence model constant	$C_{\varepsilon 2}$
Diameter	d
Effective diameter	d_e
Absolute local inter-nodal distance	$d\xi$
Fanning friction factor	f
Apparent Fanning friction factor	f_{app}
Darcy friction factor	f_D
Interpolation factor	f_n
Matrix multiplier	G
Solar energy flux per unit area	G
Gravitational acceleration	g
Height	H
Interfacial nodal vector	$\vec{I}$
Cartesian unit vector	$\underline{i}$
Turbulence intensity	i_k
Component of $\vec{J}$	J

Jacobian matrix	J
Flux vector	$\vec{J}$
Inverse Jacobian matrix	$\bar{J}$
Cartesian unit vector	$\underline{j}$
Pressure loss coefficient	K_o
Thermal conductivity, specific turbulent kinetic energy	k
Cartesian unit vector	$\underline{k}$
Thermal conductivity	$k_{laminar}$
Roughness length scale	k_s
Dimensionless roughness parameter	k_s^+
Turbulent eddy conductivity	k_t
Length, distance from entrance region	L
Length scale, one-dimensional index	ℓ
Mean Nusselt number	Nu_m
Local coordinate normal to a wall	n
First node dimensionless distance from wall	n^+
Unit normal vector	$\vec{n}$
Roughness parameter	n_0
Mass flow rate	$\dot{m}$
Production of turbulent kinetic energy	P_k
Local Peclét number	Pe
Prandtl number	Pr
Turbulent Prandtl number	Pr_t
Pressure	p
Mean pressure	$\bar{p}$
Pressure correction	p'
Previous iteration pressure value	p^*
Source term matrix	Q
Total energy	Q
Heat transfer rate	q
Heat source per unit area	q''

Heat source per unit volume	q'''
Reynolds number	Re
General nodal source term, source term matrix	S
Strain rate tensor	S
Primary source term	S_1
Secondary source term	S_2
Tertiary source term	S_3
Source term	S'
Temperature, time	T
Time	t
Instantaneous orthogonal, Cartesian velocity components	U,V,W
Instantaneous orthogonal, Cartesian velocity components	u,v,w
Mean orthogonal, Cartesian velocity components	$\overline{u},\overline{v},\overline{w}$
Instantaneous orthogonal, Cartesian velocity components	u',v',w'
First node dimensionless velocity parallel to wall	u^+
First node mean velocity parallel to wall	$\overline{u}$
Shear velocity	u_τ
Volume of a control volume	Vol
General velocity vector	$\vec{V}$
Component of $\vec{V}$	V
Width	W
Cartesian coordinate	x
Cartesian coordinate	y
First node dimensionless distance from wall	y^+
Cartesian coordinate	z

Greek Symbols

Pressure correction relaxation factor	α_p
Velocity relaxation factor	α_v
Temperature relaxation factor	α_T

Turbulent kinetic energy relaxation factor	α_k
Rate of dissipation relaxation factor	α_p
Thermal expansion coefficient	β
Rate of dissipation	ε
Dynamic viscosity	μ
Turbulent eddy viscosity	μ_t
Effective dynamic viscosity	μ_e
Diffusion coefficient	Γ
Density	ρ
Von Karman constant	κ
Instantaneous transported scalar	ϕ
Mean transported scalar, linear weighted interpolation	$\bar{\phi}$
Transported scalar fluctuation, correction	ϕ'
Reynolds stress tensor	τ_{ij}
Wall shear stress	τ_w
Turbulent Prandtl number	σ_t^k
$k-\varepsilon$ turbulence model constant	σ_k
$k-\varepsilon$ turbulence model constant	σ_ε
Viscous dissipation function	Φ
Local coordinate	ξ
Local orthogonal directional vector	$\vec{\xi}$
Local coordinate	η
Local non-orthogonal directional vector	$\vec{\eta}$
Flux blending factor	γ

Subscripts

Air	air
Ambient	a
Chimney	chim

Collector	coll
Fluid	f
Cartesian index	i,j,k
Inner position	i
Inlet	in
Central node number	N
Neighbouring node number	NN
Interface	n
Outer position	o
Outlet	out
Solar	solar
Wall	w

Superscripts

Cartesian index	i,j,k
Component or projection in the direction of the ξ coordinate	ξ
Component or projection in the direction of the η coordinate	η
Current time-step	new
Previous time-step	old

LIST OF FIGURES

LIST OF TABLES

1. INTRODUCTION.

1.1 The Numerical Modeling Field.

The numerical analysis of fluid dynamics and heat transfer mechanisms associated with fluid flows forms an integral part of the modern study of fluids. This field of research, also known as Computational Fluid Dynamics (CFD), contributes to our understanding of the phenomena and interactions involved by providing field solutions of the properties of fluid flow in the flow domain. The analytical approach to solve fluid dynamic fields usually requires simplifications and assumptions regarding the properties of the flow and its behaviour and interaction with domain boundaries. Although this often leads to accurate predictions and valuable engineering insights into many problems, it becomes mathematically challenging to obtain results for problems in complex domains and where detailed visualization is required of the fluid flow and the heat transfer mechanisms at work.

CFD provides field solutions for complex computational domains and enables a more detailed evaluation of the field behaviour if required. This is only possible by numerically solving the governing equations in the computational domain. Furthermore, the numerical modeling is neither a more expensive nor a more time consuming alternative as compared to experimental work. It is by no means a tool to replace experimental or analytical work but rather a method to complement the existing research in fluid dynamics and heat transfer.

The present study implements a general three-dimensional non-orthogonal finite volume numerical method in a FORTRAN 77 computer code to solve fluid dynamic and heat transfer problems. This code is similar to software codes found in various commercially available CFD software. The performance of the present code is evaluated against simple test cases and also applied to a typical large scale solar collector such as the collector found in solar chimney technology. The numerical modeling of a solar collector is intended to complement the concurrent analytical and experimental research being done on solar chimney technology.

1.2 Numerical Analysis of Solar Collector.

The solar chimney power generating principle is currently under investigation as a potential economical and renewable energy source. A typical solar chimney power generating plant is depicted in Figure 1.1. It consists of mainly three components namely a solar collector and a central chimney with a turbo-generator at its base. The solar collector consists of a circular glass cover supported above the ground surface. The glass cover allows solar radiation to pass through and to be absorbed in the ground. This absorbed solar energy leads to an increase in the soil temperature which in turn results in the heating of the surrounding air through convection. The change in air temperature near the bottom surface results in an upward buoyancy force in the air due to a density gradient in the air. Air rises as a result of this buoyancy force generating a draft of air from the outer perimeter of the glass collector, through the collector area and up the chimney.

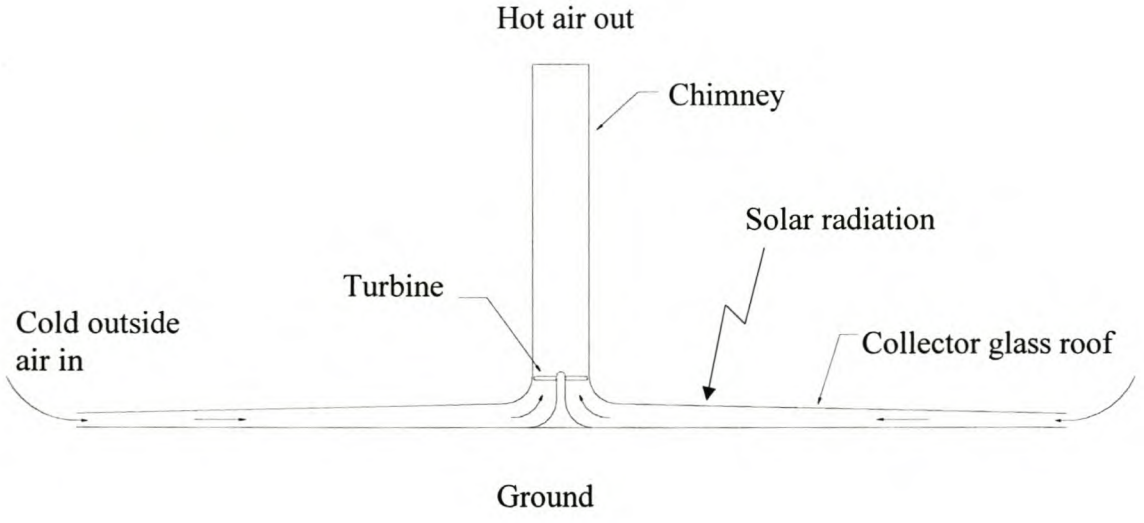

Figure 1.1. The solar chimney power plant

Essentially the principle can be simplified as illustrated by Von Backström (1999). Two columns of air, one representing the outside air and the other representing the air inside the chimney, are connected by a channel represented by the collector. A difference in density

exists between the two columns due to temperature differences of the fluid contained in the two columns: the fluid contained in the column of outside air being colder and therefore more dense. This density difference manifests itself as an available potential head pressure driving the flow between the two columns and along the channel or collector. By placing a turbine in the channel, one may capitalise on this available pressure difference to generate power, similar to a hydro-power plant. It is evident that the performance of the plant as a power generating mechanism depends on the performance and power output of the turbine which in turn relies upon the efficiency of the collector and chimney or in other words, its capability to transform solar energy into a draft of heated air. Typical dimensions proposed for a large scale solar chimney power plant includes a collector diameter of 4000 meters, raised 10 meters above the ground, a chimney diameter of 160 meters and a chimney height of more than 1000 meters.

The present study focuses on establishing a general numerical model and CFD code and the application of this code to solve the thermo-flow field in a solar collector. It is meant to provide insights into the complexity of numerical modeling, in particular the modeling of the thermal behaviour of a solar collector of the dimensions envisaged.

1.3 Contents of the Thesis

In the following chapter (Chapter 2) the governing equations related to the numerical modeling of fluid flows and heat transfer are discussed. It also presents the forms of these equations which lend themselves to the finite volume numerical method.

In Chapter 3 the finite volume discretization scheme employed is presented as well as the interpolation practices associated with this procedure. This study is meant to result in the generation of a general computational fluid dynamics code which can be applied and extended to model various fluid dynamic phenomena.

Chapter 4 contains the solution algorithm employed as well as an explanation of the strongly implicit iterative solver (SIP) employed to solve the sets of non-linear governing equations.

In Chapter 5 various grid dependent parameters and geometrical calculations are explained. The chapter also contains the description of the formulation of the code in a general non-orthogonal coordinate frame. This formulation assists the future extension of the code to other problems within more complex fluid domains.

Chapter 6 deals with the verification of the results found by applying the code to simple problems for which analytical, experimental or other numerical results are available. Each verification problem contains the key mechanisms incorporated in the code which need to be evaluated i.e., such as the modeling of turbulence and the prediction of the thermal and hydrodynamic boundary layer development.

Chapter 7 gives a more detailed description of the operating principles of the solar chimney. The application of the code to the solar collector model is discussed and the results from the field solution presented and evaluated.

In Chapter 8 the structure and contents of the general CFD code are presented and discussed.

Chapter 9 provides a conclusion to the present study as well as recommendations for future research.

2. GOVERNING DIFFERENTIAL EQUATIONS

2.1 The Basic Concepts of Fluid Flow

The basis for the understanding of the behaviour of fluid flow and its interaction with its surroundings is rooted in the assumption that it is a continuous medium. An Eulerian description of the continuum is followed in this study i.e. one where the attention is focused on the velocity field in a control volume rather than the displacement of the control volume in space, Frederick and Chang (1972). This Eulerian approach complements the finite volume method followed in this study.

Three-dimensional, incompressible, viscous fluid flow, characterised by the three basic conservation equations, is considered. These conservation equations are:

conservation of mass (continuity equations),
conservation of momentum (Newton's second law) and
conservation of energy (first law of thermodynamics).

Other important auxiliary relations describe the properties of the continuum such as density, viscosity, conductivity and enthalpy. Lastly, equations for turbulent kinetic energy and turbulent dissipation allow for the investigation of the turbulent behaviour of the fluid.

2.2 Conservation of Mass

The differential coordinate free form of the continuity equation for compressible, transient fluid motion is

$$\frac{\partial \rho}{\partial t} + \vec{\nabla}\left(\rho \vec{V}\right) = 0 \qquad (2.1)$$

For incompressible flow the equation becomes

$$\vec{\nabla} \cdot \vec{V} = 0 \qquad (2.2)$$

Although the flow considered may be assumed incompressible, equation (2.1) is employed in this study to allow for variable density due to changes in temperature.

2.3 Conservation of Momentum

The three-dimensional momentum conservation or Navier Stokes equations for a general, incompressible and Newtonian fluid are derived from Newton's second law which expresses the proportionality between a force applied to a particle and the resulting acceleration of that particle. In a Cartesian coordinate frame these equations for transient fluid flows, as presented by White (1991), are,

x-momentum conservation equation :

$$\rho\frac{\partial u}{\partial t}+\rho u\frac{\partial u}{\partial x}+\rho v\frac{\partial u}{\partial y}+\rho w\frac{\partial u}{\partial z}= -\frac{\partial p}{\partial x}+\frac{\partial}{\partial x}\left(2\mu\frac{\partial u}{\partial x}\right)+\frac{\partial}{\partial y}\left[\mu\left(\frac{\partial u}{\partial y}+\frac{\partial v}{\partial x}\right)\right]+\frac{\partial}{\partial z}\left[\mu\left(\frac{\partial w}{\partial x}+\frac{\partial u}{\partial z}\right)\right]+\rho g_x \tag{2.3}$$

y-momentum conservation equation :

$$\rho\frac{\partial v}{\partial t}+\rho u\frac{\partial v}{\partial x}+\rho v\frac{\partial v}{\partial y}+\rho w\frac{\partial v}{\partial z}= -\frac{\partial p}{\partial y}+\frac{\partial}{\partial x}\left[\mu\left(\frac{\partial v}{\partial x}+\frac{\partial u}{\partial y}\right)\right]+\frac{\partial}{\partial y}\left(2\mu\frac{\partial v}{\partial y}\right)+\frac{\partial}{\partial z}\left[\mu\left(\frac{\partial v}{\partial z}+\frac{\partial w}{\partial y}\right)\right]+\rho g_y \tag{2.4}$$

z-momentum conservation equation :

$$\rho\frac{\partial w}{\partial t}+\rho u\frac{\partial w}{\partial x}+\rho v\frac{\partial w}{\partial y}+\rho w\frac{\partial w}{\partial z}= -\frac{\partial p}{\partial z}+\frac{\partial}{\partial x}\left[\mu\left(\frac{\partial w}{\partial x}+\frac{\partial u}{\partial z}\right)\right]+\frac{\partial}{\partial y}\left[\mu\left(\frac{\partial v}{\partial z}+\frac{\partial w}{\partial y}\right)\right]+\frac{\partial}{\partial z}\left(2\mu\frac{\partial w}{\partial z}\right)+\rho g_z \tag{2.5}$$

The treatment of these Cartesian equations in a global coordinate free frame with non-orthogonal grids is discussed in chapter 5. These equations can be presented in the more convenient conservative form by employing the continuity equation

$$\frac{\partial}{\partial t}(\rho u)+\frac{\partial}{\partial x}(\rho uu)+\frac{\partial}{\partial y}(\rho vu)+\frac{\partial}{\partial x}(\rho wu)-\frac{\partial}{\partial x}\left(\mu\frac{\partial u}{\partial x}\right)-\frac{\partial}{\partial y}\left(\mu\frac{\partial u}{\partial y}\right)-\frac{\partial}{\partial z}\left(\mu\frac{\partial u}{\partial z}\right)= -\frac{\partial p}{\partial x}+\frac{\partial}{\partial x}\left(\mu\frac{\partial u}{\partial x}\right)+\frac{\partial}{\partial y}\left(\mu\frac{\partial v}{\partial x}\right)+\frac{\partial}{\partial z}\left(\mu\frac{\partial w}{\partial x}\right)+\rho g_x \tag{2. 6}$$

$$\frac{\partial}{\partial t}(\rho v)+\frac{\partial}{\partial x}(\rho uv)+\frac{\partial}{\partial y}(\rho vv)+\frac{\partial}{\partial x}(\rho wv)-\frac{\partial}{\partial x}\left(\mu\frac{\partial v}{\partial x}\right)-\frac{\partial}{\partial y}\left(\mu\frac{\partial v}{\partial y}\right)-\frac{\partial}{\partial z}\left(\mu\frac{\partial v}{\partial z}\right)= -\frac{\partial p}{\partial y}+\frac{\partial}{\partial x}\left(\mu\frac{\partial u}{\partial y}\right)+\frac{\partial}{\partial y}\left(\mu\frac{\partial v}{\partial y}\right)+\frac{\partial}{\partial z}\left(\mu\frac{\partial w}{\partial y}\right)+\rho g_y \tag{2. 7}$$

$$\frac{\partial}{\partial t}(\rho w)+\frac{\partial}{\partial x}(\rho uw)+\frac{\partial}{\partial y}(\rho vw)+\frac{\partial}{\partial x}(\rho ww)-\frac{\partial}{\partial x}\left(\mu\frac{\partial w}{\partial x}\right)-\frac{\partial}{\partial y}\left(\mu\frac{\partial w}{\partial y}\right)-\frac{\partial}{\partial z}\left(\mu\frac{\partial w}{\partial z}\right)= -\frac{\partial p}{\partial z}+\frac{\partial}{\partial x}\left(\mu\frac{\partial u}{\partial z}\right)+\frac{\partial}{\partial y}\left(\mu\frac{\partial v}{\partial z}\right)+\frac{\partial}{\partial z}\left(\mu\frac{\partial w}{\partial z}\right)+\rho g_z \tag{2. 8}$$

The terms on the left hand side of the momentum equations represents the time dependent velocity differential, the differentials of convection of momentum, normal and perpendicular to the flow direction, as well as the differentials of diffusion of momentum through normal stresses and Newtonian shear stresses. The terms on the right hand side represent the pressure gradient, additional differentials of normal stresses due to viscosity variations as well as other momentum sources. The velocity differentials present can be grouped in a viscous stress tensor defined as the product of the viscosity and a strain rate tensor. This grouping of differentials will be discussed later in this chapter in the context of turbulence modeling. An additional body force term such as that due to buoyancy effects is also included on the right hand side of these momentum equations.

The conservative form of the equations allows the rewriting of equations (2.6) to (2.8) as

$$\frac{\partial}{\partial t}(\rho u)+\vec{\nabla}\cdot(\rho\vec{V}u)-\vec{\nabla}\cdot(\mu\vec{\nabla}u)=-\frac{\partial p}{\partial x}+\frac{\partial}{\partial x}\left(\mu\frac{\partial u}{\partial x}\right)+\frac{\partial}{\partial y}\left(\mu\frac{\partial v}{\partial x}\right)+\frac{\partial}{\partial z}\left(\mu\frac{\partial w}{\partial x}\right)+\rho g_x \qquad (2.9)$$

$$\frac{\partial}{\partial t}(\rho v)+\vec{\nabla}\cdot(\rho\vec{V}v)-\vec{\nabla}\cdot(\mu\vec{\nabla}v)=-\frac{\partial p}{\partial y}+\frac{\partial}{\partial x}\left(\mu\frac{\partial u}{\partial y}\right)+\frac{\partial}{\partial y}\left(\mu\frac{\partial v}{\partial y}\right)+\frac{\partial}{\partial z}\left(\mu\frac{\partial w}{\partial y}\right)+\rho g_y \qquad (2.10)$$

$$\frac{\partial}{\partial t}(\rho w)+\vec{\nabla}\cdot(\rho\vec{V}w)-\vec{\nabla}\cdot(\mu\vec{\nabla}w)=-\frac{\partial p}{\partial z}+\frac{\partial}{\partial x}\left(\mu\frac{\partial u}{\partial z}\right)+\frac{\partial}{\partial y}\left(\mu\frac{\partial v}{\partial z}\right)+\frac{\partial}{\partial z}\left(\mu\frac{\partial w}{\partial z}\right)+\rho g_z \qquad (2.11)$$

or in a general form

$$\frac{\partial}{\partial t}(\rho\phi)+\vec{\nabla}\cdot\vec{J}(\phi)=S(\phi) \qquad (2.12)$$

$$\vec{J}(\phi)=\rho\vec{V}\phi-\Gamma\vec{\nabla}\phi \qquad (2.13)$$

where $\vec{J}$ is a flux vector with convection and diffusion parts, ϕ being the transported scalar and Γ being the diffusion constant.

This general form of equation (2.12) simplifies the discretization of the equations since the flux vector terms will contribute to the influence coefficients of the discretized equation while all other terms are classified as source terms and will be treated as explicit scalars.

2.4 Conservation of Energy

The energy conservation equation derived from the first law of thermodynamics and as presented by Rohsenow, Hartnett and Ganic (1985) is

$$\rho C_p \frac{DT}{Dt} + \beta T \frac{Dp}{Dt} = \vec{\nabla} \cdot \left(k \vec{\nabla} T \right) + \Phi + q''' \tag{2. 14}$$

where $\frac{D}{Dt} = \frac{\partial}{\partial t} + \vec{V} \cdot \vec{\nabla}$ denotes the substantial derivative, Φ is a viscous dissipation function and q''' is an energy source term. For incompressible flows with variable density from temperature changes, negligible transient pressure changes and in the absence of any energy sources such as radiation, equation (2.14) simplifies to

$$\rho C_p \frac{DT}{Dt} = \vec{\nabla} \cdot \left(k \vec{\nabla} T \right) + \Phi \tag{2. 15}$$

with the dissipation function being

$$\Phi = \mu \left[2\left(\frac{\partial u}{\partial x}\right)^2 + 2\left(\frac{\partial v}{\partial y}\right)^2 + 2\left(\frac{\partial w}{\partial z}\right)^2 + \left(\frac{\partial v}{\partial x} + \frac{\partial u}{\partial y}\right)^2 + \left(\frac{\partial w}{\partial y} + \frac{\partial v}{\partial z}\right)^2 + \left(\frac{\partial u}{\partial z} + \frac{\partial w}{\partial x}\right)^2 \right] - \frac{2}{3}\mu \left[\frac{\partial u}{\partial x} + \frac{\partial v}{\partial y} + \frac{\partial w}{\partial z} \right]^2 \tag{2. 16}$$

Considering continuity it is clear that the second group of terms in square brackets in equation (2.16) will disappear for incompressible flows.

2.5 Auxiliary Equations

The previous mass, momentum and energy conservation equations constitute primary and secondary variables. Primary variables are properties of the flow namely velocity (u, v and w), pressure (p) and temperature (T). Secondary variables constitute fluid properties such as density, viscosity and conductivity to be found from auxiliary relations of the form

$$\begin{aligned} \rho &= \rho(p, T) \\ \mu &= \mu(p, T) \\ k &= k(p, T) \end{aligned} \tag{2. 17}$$

2.6 Turbulence

2.6.1 Background

Turbulent fluid motion is characterized by fluctuations of field quantities, such as pressure, velocity and temperature, superimposed upon mean quantities, as well as the presence of eddies of variable size. The eddies present in the shear layer move in three-dimensional directions causing the rapid diffusion of mass, momentum and energy and leading to the increase in mixing and heat transfer associated with turbulent flows.

The presence of turbulence in fluid flows may prove advantageous where increased mixing and heat transfer is required but these mixing forces also contribute to an increase in the frictional forces with subsequent increase in pressure drop. Thus, turbulent modeling is an important aspect of understanding and solving engineering problems. Ferziger and Perić (1996) list a number of categories for predicting phenomena of turbulent fluid flows including empirical correlations, correlations derived from integral analysis, time averaging of the conservation equations, large eddy simulation (LES) and direct numerical simulation (DNS).

Our present understanding of turbulent motion leads us to the assumption that the Navier-Stokes equations include the momentum conservation of turbulent flows. The present study employs time averaging of the momentum conservation equations with a two equation, $k-\varepsilon$ turbulence model since it eliminates the need for supercomputing resources (DNS) and, as mentioned by Mohammadi and Pironneau (1994), presents a good compromise between simplicity and generality. The two equation turbulence models are usually found to be accurate for high Reynolds number flows and when they are not applied to predict near wall flows, Sarkar and So (1997), So, Zhang and Speziale (1991). However, the present $k-\varepsilon$ turbulence model, applied to large Reynolds numbers such as evaluated in this study, was found to be accurate and compares well with experimental results as well as with direct numerical simulation results, Henkes (1998).

2.6.2 Reynolds averaged Navier-Stokes (RANS) equations

Reynolds introduced averaging concepts for turbulent flows of which three are most pertinent to turbulent flows namely, the time average, the spatial average and the ensemble average, Wilcox (1994). For the purpose of this discussion we refer only to the time average. An instantaneous value of the general transported property $\phi(x_i,t)$ can be written as the sum of a mean and a fluctuating part

$$\phi(x_i,t) = \bar{\phi}(x_i) + \phi'(x_i,t) \tag{2.18}$$

The mean component in equation (2.18) is the time average of the transported scalar defined by

$$\bar{\phi}(x_i) = \lim_{T\to\infty} \frac{1}{T} \int_t^{t+T} \phi(x_i,t)dt \tag{2.19}$$

where the time averaging interval T, is large compared to the time scale of the fluctuations.

It can be shown that the time average of the mean scalar value is the same as the time-averaged value leading to the conclusion that the time average of the fluctuating part is zero

$$\overline{\phi'}(x_i,t) = \lim_{T\to\infty} \frac{1}{T} \int_t^{t+T} \left[\phi(x_i,t) - \bar{\phi}(x_i)\right]dt = \bar{\phi}(x_i) - \bar{\phi}(x_i) = 0 \tag{2.20}$$

For the purpose of time averaging the conservation equations, we need to consider the time average of two properties such as $\overline{u\phi}$. Since the product of a mean quantity and a fluctuating quantity has zero mean we can write this as

$$\overline{u\phi} = \overline{(\bar{u}+u')(\bar{\phi}+\phi')} = \overline{\bar{u}\bar{\phi} + \bar{u}\phi' + \bar{\phi}u' + u'\phi'} = \bar{u}\bar{\phi} + \overline{u'\phi'} \tag{2.21}$$

The last term in equation (2.21) is zero when the terms are said to be uncorrellated and since this is rarely the case, additional terms present themselves in the conservation equations.

By replacing the instantaneous variables in the continuity, conservation of momentum and general scalar transport equations by a mean variable quantity with a fluctuating part, one finds the Reynolds-averaged conservation equations which are similar to the equations for the instantaneous velocity except for additional Reynolds stress terms. These equations for incompressible flow in a Cartesian coordinate frame can subsequently be given as

$$\vec{\nabla}\cdot\vec{\bar{V}} = 0 \tag{2. 22}$$

$$\frac{\partial}{\partial t}(\rho\bar{u}) + \vec{\nabla}\cdot\left(\rho\vec{\bar{V}}\bar{u}\right) - \vec{\nabla}\cdot\left(\mu\vec{\nabla}\bar{u}\right) = -\frac{\partial p}{\partial x} + \frac{\partial}{\partial x}\left(\mu\frac{\partial\bar{u}}{\partial x}\right) + \frac{\partial}{\partial y}\left(\mu\frac{\partial\bar{v}}{\partial x}\right) + \frac{\partial}{\partial z}\left(\mu\frac{\partial\bar{w}}{\partial x}\right) +$$

$$+\left(\frac{\partial}{\partial x}\left(-\rho\overline{u'u'}\right) + \frac{\partial}{\partial y}\left(-\rho\overline{u'v'}\right) + \frac{\partial}{\partial x}\left(-\rho\overline{u'w'}\right)\right) + \rho g_x \tag{2. 23}$$

$$\frac{\partial}{\partial t}(\rho\bar{v}) + \vec{\nabla}\cdot\left(\rho\vec{\bar{V}}\bar{v}\right) - \vec{\nabla}\cdot\left(\mu\vec{\nabla}\bar{v}\right) = -\frac{\partial p}{\partial y} + \frac{\partial}{\partial x}\left(\mu\frac{\partial\bar{u}}{\partial y}\right) + \frac{\partial}{\partial y}\left(\mu\frac{\partial\bar{v}}{\partial y}\right) + \frac{\partial}{\partial z}\left(\mu\frac{\partial\bar{w}}{\partial y}\right) +$$

$$+\left(\frac{\partial}{\partial x}\left(-\rho\overline{v'u'}\right) + \frac{\partial}{\partial y}\left(-\rho\overline{v'v'}\right) + \frac{\partial}{\partial x}\left(-\rho\overline{v'w'}\right)\right) + \rho g_y \tag{2. 24}$$

$$\frac{\partial}{\partial t}(\rho\bar{w}) + \vec{\nabla}\cdot\left(\rho\vec{\bar{V}}\bar{w}\right) - \vec{\nabla}\cdot\left(\mu\vec{\nabla}\bar{w}\right) = -\frac{\partial p}{\partial z} + \frac{\partial}{\partial x}\left(\mu\frac{\partial\bar{u}}{\partial z}\right) + \frac{\partial}{\partial y}\left(\mu\frac{\partial\bar{v}}{\partial z}\right) + \frac{\partial}{\partial z}\left(\mu\frac{\partial\bar{w}}{\partial z}\right) +$$

$$+\left(\frac{\partial}{\partial x}\left(-\rho\overline{w'u'}\right) + \frac{\partial}{\partial y}\left(-\rho\overline{w'v'}\right) + \frac{\partial}{\partial z}\left(-\rho\overline{w'w'}\right)\right) + \rho g_z \tag{2. 25}$$

The additional terms are dependent on factors such as fluid properties, flow conditions, geometry, roughness and upstream history of the flow, all complicating our modeling since their solution is not known a priori. The basis for the $k-\varepsilon$ turbulence model is the

Boussinesq eddy-viscosity approximation of the Reynolds stress tensor as the product of an eddy viscosity μ_t and the mean strain rate tensor.

From the mixing length hypothesis of Prandtl (1925), as presented by Wilcox (1994), the specific turbulent kinetic energy (per unit mass) of the turbulent fluctuations may be used as basis for the velocity scale for turbulence i.e.

$$k = \frac{1}{2}\left(\overline{u'^2} + \overline{v'^2} + \overline{w'^2}\right) \tag{2. 26}$$

Equation (2.26) may be rewritten as

$$2\rho k = \rho\overline{u'u'} + \rho\overline{v'v'} + \rho\overline{w'w'} \tag{2. 27}$$

Following a Boussinesq approximation the Reynolds stress terms in equations (2.23) to (2.25) are written as a gradient diffusion or shear term, analogous to the laminar diffusion gradient, and the Reynolds stress tensor becomes, as given by Wilcox (1994) and presented in tensor notation for economy

$$\tau_{ij} = -\rho\overline{u_i'u_j'} = 2\mu_t S_{ij} - \frac{2}{3}\rho k\delta_{ij} \tag{2. 28}$$

where the mean strain rate tensor is given as

$$S_{ij} = \frac{1}{2}\left(\frac{\partial\overline{u_i'}}{\partial x_j} + \frac{\partial\overline{u_j'}}{\partial x_i}\right) \tag{2. 29}$$

and where the presence of the second term in equation (2.28) ensures that the condition of equation (2.27) is met. Since one has found substitutions for the Reynolds stress terms in equations (2.23) to (2.25) in terms of eddy viscosity and turbulent kinetic energy one finds, after some algebra, that the original form of the conservation equations, equations (2.9) to

(2.11), remains generally unchanged except for the substitution of the viscosity with an effective viscosity defined as

$$\mu_e = \mu + \mu_t \tag{2.30}$$

The resultant solution of the pressure field now contains an additional contribution evident from the pressure gradient in the primary source term given by

$$\frac{\partial p}{\partial x_i} = \frac{\partial}{\partial x_i}\left(\overline{p} + \frac{2}{3}\rho k\right) \tag{2.31}$$

The conservation equations can therefore be solved once a relation for the eddy viscosity and specific turbulent kinetic energy is established. A dimensional argument indicates that the eddy viscosity is proportional to the kinetic energy and a length scale,

$$\mu_t \propto \rho k^{\frac{1}{2}} \ell \tag{2.32}$$

Since we now have additional variables we require additional equations which can be found from taking moments of the Navier-Stokes equations i.e. multiplying the conservation equation by a fluctuating property and time averaging the result. Substituting the resulting double velocity fluctuations with equation (2.28) and assuming that

$$\frac{1}{2}\rho\overline{u_i' u_i' u_j'} + \overline{p' u_j'} = -\frac{\mu_t}{\sigma_k}\frac{\partial k}{\partial x_j} \tag{2.33}$$

where σ_k is a turbulent Prandtl number close to unity, one finds after considerable algebra as presented by Wilcox (1994) and explained by Thiart (1998)

$$\frac{\partial}{\partial t}(\rho k) + \vec{\nabla}\cdot\left(\rho\vec{\nabla}k\right) = \vec{\nabla}\cdot\left(\left(\frac{\mu + \mu_t}{\sigma_t^k}\right)\vec{\nabla}k\right) + P_k - \rho\varepsilon \tag{2.34}$$

The rate of production of turbulent energy P_k, or the rate at which kinetic energy is transferred from the mean flow to turbulence, is given by

$$P_k = \mu_t \left(2\left(\left(\frac{\partial \overline{u}}{\partial x}\right)^2 + \left(\frac{\partial \overline{v}}{\partial y}\right)^2 + \left(\frac{\partial \overline{w}}{\partial z}\right)^2 \right) + \left(\frac{\partial \overline{u}}{\partial y} + \frac{\partial \overline{v}}{\partial x}\right)^2 + \left(\frac{\partial \overline{v}}{\partial z} + \frac{\partial \overline{w}}{\partial y}\right)^2 + \left(\frac{\partial \overline{w}}{\partial x} + \frac{\partial \overline{u}}{\partial z}\right)^2 \right) \qquad (2.35)$$

The rate of dissipation ε, can be found from solving

$$\frac{\partial}{\partial t}(\rho\varepsilon) + \vec{\nabla}\cdot\left(\rho\vec{\overline{V}}\varepsilon\right) = \vec{\nabla}\cdot\left(\left(\frac{\mu + \mu_t}{\sigma_t^{\varepsilon}}\right)\vec{\nabla}\varepsilon\right) + \frac{\varepsilon}{k}(C_{\varepsilon 1}P_k - C_{\varepsilon 2}\rho\varepsilon) \qquad (2.36)$$

and introducing the turbulent Prandtl /Schmidt number

$$\sigma_t^k = \frac{\mu_t}{\Gamma_t^{\phi}} \qquad (2.37)$$

From a dimensional argument the eddy viscosity equals

$$\mu_t = \rho C_{\mu}\frac{k^2}{\varepsilon} \qquad (2.38)$$

After the solution of the discretized momentum conservation and pressure correction equations, the k and ε nodal values are found from the solution of equations (2.34) and (2.36). The momentum and pressure correction equations are solved with previous iteration values of effective viscosity calculated from k and ε. The five parameters encountered in the $k-\varepsilon$ equations are given commonly accepted values namely

$$C_{\mu} = 0.09 \quad C_{\varepsilon 1} = 1.44 \quad C_{\varepsilon 2} = 1.92 \quad \sigma_t^k = 1.0 \quad \sigma_t^{\varepsilon} = 1.3 \qquad (2.39)$$

To ensure that k and ε remain positive during the solution one can simply linearise the source terms in equations (2.34) and (2.36) as follows

$$-\rho\varepsilon = -\left(\rho\frac{\varepsilon^*}{k^*}\right)k \tag{2.40}$$

and

$$-\frac{\varepsilon}{k}\left(C_{\varepsilon 2}\rho\varepsilon\right) = -\left(\frac{C_{\varepsilon 2}\rho\varepsilon^*}{k^*}\right)\varepsilon \tag{2.41}$$

where the terms in brackets on the right hand side of equations (2.40) and (2.41) are added to the implicit nodal influence coefficient in the discretised equation as discussed in chapter 3.

The boundary conditions for the $k-\varepsilon$ turbulence model require careful consideration. For high Reynolds numbers as expected for the flows considered in this study, the viscous sublayer of the boundary layer is extremely thin requiring many grid points to resolve. One may employ wall functions to approximate the logarithmic region of the turbulent velocity profile defined as

$$u^+ = \frac{\bar{u}_w}{u_\tau} = \frac{1}{\kappa}\ln\left(n^+\right) + B \tag{2.42}$$

where $\bar{u}_w$ is the mean velocity parallel to the wall, $u_\tau = \sqrt{\frac{\tau_w}{\rho}}$ is the shear velocity, τ_w is the shear stress at the wall, $\kappa \approx 0.41$ is the Von Karman constant, $B \approx 5.2$ is an empirical constant and $n^+ = \frac{u_\tau y_w}{\nu}$ is the dimensionless distance from the wall. By assuming that the rate of dissipation of turbulent kinetic energy equals the rate of production at the first node from the wall one may find the boundary conditions for the turbulence quantities. Furthermore it is assumed that all the mean velocity gradients, except for $\frac{\partial \bar{u}_w}{\partial n}$, are zero at the wall ($\partial n$ being the normal distance from the wall). It can be shown that these assumptions lead to

$$P_k = \rho\varepsilon_w = \mu_t\left(\frac{\partial \bar{u}_w}{\partial n}\right)^2 = \frac{\tau_w^2}{\mu_t} = \frac{u_\tau^4}{C_\mu k_w^2}\rho\varepsilon_w \qquad (2.43)$$

by employing a simplification of the Boussinesq approximation of equation (2.28) at the wall i.e.

$$\tau_w = \mu_t \frac{\partial \bar{u}_w}{\partial n} \qquad (2.44)$$

Rewriting equation (2.43) one finds

$$k_w = \frac{u_\tau^2}{\sqrt{C_\mu}} \qquad (2.45)$$

Furthermore, by differentiating equation (2.42) in terms of normal distance from the wall (n), the velocity gradient at and normal to the wall may be defined as

$$\frac{\partial \bar{u}_w}{\partial n} = \frac{u_\tau}{\kappa n} \qquad (2.46)$$

which together with equations (2.43) and (2.45) may be used to provide a second equation namely

$$\varepsilon_w = \frac{u_\tau^3}{\kappa n} \qquad (2.47)$$

Equations (2.45) and (2.47) now provides the turbulent dissipation and production rates at the first node from the wall. The shear velocity term in each of these is found by iteratively solving equation (2.42). Thus, one can solve the field kinetic energy and dissipation rates with wall boundary conditions at the first node away from the wall and subsequently calculate the field effective viscosity. Since the turbulent computational domain excludes the wall nodes

one finds the effective viscosity at the wall as the larger value of the laminar viscosity or the viscosity calculated from

$$\tau_w = u_\tau^2 \rho = \mu_w \frac{\partial \overline{u}_w}{\partial n} \qquad (2.48)$$

It should be noted that the normal velocity gradient terms at the wall found in the turbulent conservation equations should be replaced by equation (2.46). This will ensure that the gradients are consistent with the law of the wall definition. The above formulation of the $k-\varepsilon$ turbulence model is valid if the first node lies within the logarithmic region ($30 < n^+ < 100$), White (1991). Various authors have studied other turbulence models that introduce other modeling functions directly into the $k-\varepsilon$ equations to predict the turbulence near and at the walls, Chien (1982), Nisizima and Yoshizama (1986) and So, Zhang and Speziale (1991). The application of such methods was beyond the scope of the present study. Henkes (1998) also showed that for high Reynolds number flows with zero pressure gradient the present $k-\varepsilon$ turbulence model gives accurate results and compares well with direct numerical simulation.

For turbulent flows over rough surfaces the logarithmic law, equation (2.42), still holds for the velocity distribution outside the viscous sublayer, Schlichting (1968). However the empirical constant, $B \approx 5.2$, requires modification to represent flow across rough surfaces. The modifications to the logarithmic law and its application to turbulence modeling are extensively studied and applied by various authors, Nikuradse (1933), Schlichting (1968), White (1991), Yoon et. al. (1996), Sajjadi and Waywell (1997), Lakehal (1999). The wall roughness length, k_s, may be grouped in a dimensionless term, White (1991) i.e.

$$k_s^+ = \frac{k_s u_\tau}{\nu} \qquad (2.49)$$

which is a Reynolds number formed from with the sand grain size and the shear velocity, Schlichting (1968). The roughness length in equation (2.49) is the equivalent sand roughness, i.e. the length value which is determined experimentally from actual measured friction

resistance values for a given rough surface, Schlichting (1968). For the present study this is assumed to be equal to the roughness height.

This Reynolds number given by equation (2.49) defines three roughness regimes:

Hydraulically smooth regime: $0 \le k_s^+ \le 5$

Transition regime: $5 \le k_s^+ \le 70$

Completely rough regime: $k_s^+ > 70$

Equation (2.42) may be re-written to incorporate k_s^+ and to facilitate its modification and application to the $k-\varepsilon$ turbulence model wall functions for rough surfaces, Sajjadi and Waywell (1997) i.e.

$$\frac{u}{u_\tau} = \frac{1}{\kappa} \ln\left(\frac{n}{n_0}\right) \qquad (2.50)$$

where

$$n_0 = \frac{\nu}{E C_\mu^{1/4} k^{1/2}} \qquad (2.51)$$

The roughness coefficient, E, is given by the following expression

$$E = \frac{\exp(\kappa B_s)}{k_s^+} \qquad (2.52)$$

where the new empirical constant, B_s, for an equivalent sand roughness, Nikuradse (1933), is given by Sajjadi and Aldridge (1995) and Sajjadi and Waywell (1997) i.e.

$$B_s\left(k_s^+\right)=\left(5.5+2.5\cdot\ln\left(k_s^+\right)\right)\cdot e^{-0.062\cdot\left(\ln\left(k_s^+\right)\right)^3}+8.5\cdot\left(1-e^{-0.062\left(\ln\left(k_s^+\right)\right)^3}\right) \tag{2.53}$$

White (1991) shows that for the completely rough regime equation (2.52) may be substituted with

$$E=e^{\kappa B_s} \tag{2.54}$$

where the empirical constant is given by

$$B_s\left(k_s^+\right)=5.2-\frac{1}{\kappa}\ln\left(1+0.3k_s^+\right) \tag{2.55}$$

Sajjadi and Waywell (1997) showed that the roughness method mentioned above combined with the $k-\varepsilon$ turbulence model gave excellent agreement with experimental results. Yoon and Patel (1996) also found good agreement with experimental results by combining the above method with the a $k-\omega$ turbulence method. Apart from the accuracy of the method, it is also simple to implement since the only the modification required is the calculation for the roughness coefficient, E, by employing equation (2.52).

2.6.3 Turbulent heat transfer

Similarly to the previously mentioned Boussinesq approximation applicable to the Reynolds Averaged Navier Stokes equations, one can formulate a Boussinesq analogy for eddy conductivity i.e.

$$q=-\left(k+k_t\right)\frac{\partial T}{\partial n} \tag{2.56}$$

As mentioned by White (1991) the turbulent eddy viscosity and conductivity are not physical flow properties but can be grouped in a dimensionless turbulent Prandtl number namely

$$Pr_t = \frac{C_p \mu_t}{k_t} \tag{2. 57}$$

Reynolds (1874), as mentioned by White (1991), postulated that the turbulent momentum and heat flux are equivalent phenomena of the same order of magnitude

$$Pr_t = f(Pr) = O(1) \tag{2. 58}$$

which is one form of the famous Reynolds analogy. The use of a constant turbulent Prandtl number in modeling turbulent flow has been very successful and is employed in many commercially available CFD codes such as CFX of AEA Technology. A value of Pr_t=0.9 is recommended for 0.7<Pr<1.0 by White (1992). This study found consistently accurate results with 0.7<Pr_t<1.0. With a known constant Pr_t and calculation of μ_t from the turbulence models one easily finds

$$k_t = \frac{C_p \mu_t}{Pr_t} \tag{2. 59}$$

and replace the conductivity values with an effective conductivity

$$k_e = (k + k_t) \tag{2. 60}$$

similar to the effective viscosity.

3. DISCRETIZATION OF THE GOVERNING EQUATIONS

3.1 Introduction

Various methods are available for the numerical solution of fluid flow problems and their associated heat transfer, the three most often encountered being the finite element, finite difference and finite volume approach. The finite volume method has been used extensively in computational fluid mechanics and complements the understanding and interpretation of fluid flows. It was selected for the present study based on comments made by Harms (1995) in this regard. The finite volume approach is an essentially simple mathematical approach whereby the strong coupling between the mathematical model and the physical nature of the problem can easily be recognised. The method is also widely used in commercially available computational flow software such as, among others, CFX of AEA Technology. The computational grid defines control volume boundaries rather than nodes. In the finite volume approach the governing equations are integrated over a finite number of control volumes. These integrals are then discretized in terms of nodal values represented by the centres of the control volume, and interfacial values at control volume boundaries. The interfacial values required may be found from a suitable interpolation between neighbouring nodal values.

3.2 Interpolation Schemes

The numerical approach of the finite volume method requires the approximation of a transported scalar ϕ, and the derivatives at control volume interfaces. The interpolation scheme selected for this study is a central difference, flux blended, deferred correction approach as suggested by Perić (1985) and based on a similar concept by Khosla and Rubin (1974). As pointed out by Perić (1985), the finite discretization requires that the discretized equations satisfy certain conditions of an exact solution of the governing equations namely,

Conservativeness:

Conservativeness of a discretization scheme refers to the conservation of properties within control volumes. The finite volume discretization employs integration over discrete control

volumes resulting in cell face fluxes. When summed, these interfacial fluxes, as well as the addition of possible internal sources should cancel, leading to the conservation of a property such as heat or mass. This conservative condition should be reflected in the numerical scheme in order to achieve realistic results.

Boundedness:

The set of discretized conservation equations are bounded by the scalar properties on the domain boundaries. Thus, in the absence of source terms in these equations, the converged results should be within the minimum and maximum limits set by the boundary conditions. The diagonally dominant coefficient matrix generated by a discretized conservation equation should also satisfy the bounded condition ensuring that all the neighbouring coefficients are of the same sign. A change in the scalar property at one neighbouring node with other neighbouring nodes constant, would subsequently be reflected in a central node property change in the same direction i.e., if the temperature at only one neighbouring node increases, then the central nodal temperature would also increase. A discretization scheme that does not satisfy the boundedness condition is said to be unbounded and would tend to produce overshoots, undershoots or 'wiggles' in the solution. The boundedness criterion is a powerful code evaluation parameter whereby discretization and programming errors may be traced.

Transportiveness:

The propagation of properties in a given flow field is dependent on the ratio of convection and diffusion i.e., by the local Peclét number

$$Pe_n = \frac{\rho_n V_n^{\xi} \delta\xi}{\Gamma_n} \qquad (3.1)$$

V_n^{ξ} is the projection of the interfacial velocity vector in the direction of the nodal vector as discussed in chapter 5. This implies that all interfacial velocities entering the control volume will be negative since all nodal vectors have been assigned direction of positive outward. For high Peclét numbers, convection processes start to dominate and the influence of diffusion

becomes smaller. Thus at high Peclét numbers the behaviour of the central node N will have little effect on its upstream neighbours. The discretized equations should reflect this behaviour.

The general central difference interpolation scheme is

$$\phi_n = (1 - f_n)\phi_N + f_n\phi_{NN} \tag{3. 2}$$

where f_n is a linear interpolation factor and the subscripts N and NN denote the central node and neighbouring node respectively. The interpolation factor can be found from

$$f_n = \frac{\delta(\xi_N)}{\delta(\xi_N) + \delta(\xi_{NN})} = \frac{\delta(\xi_N)}{\delta\xi} \tag{3. 3}$$

where $\delta(\xi_N)$ and $\delta(\xi_{NN})$ denote the absolute distances from nodes N and NN respectively, along the local nodal vector $\vec{\xi}$, to the interpolation point at the control volume interface as per figure 3.1.

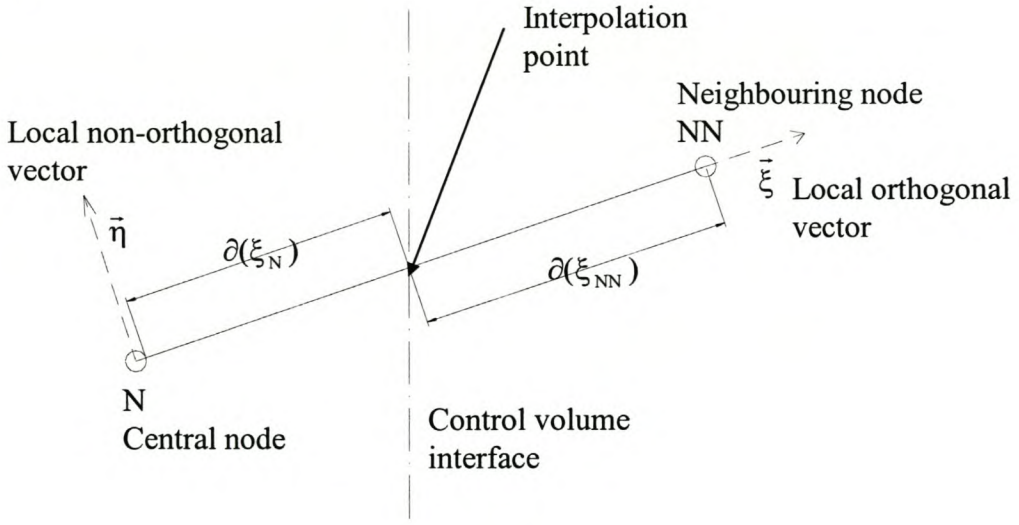

Figure 3.1. The formulation of the interpolation function

The central difference scheme is widely used but has an inherent weakness since transportive conditions are not always realistically met, as indicated by Perić (1985). Even at high Peclét numbers ($Pe \rightarrow \infty$), equation (3.2) allows upstream propagation of properties at downstream nodes which is physically unrealistic. However, the scheme is conservative and for small Peclét numbers stable and accurate.

An upwind scheme approximates the interfacial scalar value by the upwind nodal value only. Although a robust scheme, it lacks accuracy and is not an appropriate scheme where diffusion processes dominate. The formulation of such an interpolation scheme is

$$\phi_n = \left[\left|\ V_n^{\xi}\ ;\ 0.0\ \right|\right]\frac{1}{V_n^{\xi}}\phi_N + \left[\left|\ -V_n^{\xi}\ ;\ 0.0\ \right|\right]\frac{1}{-V_n^{\xi}}\phi_{NN} \qquad (3.4)$$

The $\left[\left|\ \right|\right]$-operator denotes the maximum of the values within the brackets similar to the Fortran function AMAX1[a_1,a_2,a_3,...,a_n] as suggested by Patankar (1980). The disadvantage of the upwind scheme is that it is due to lead to false diffusion where the flow is not grid aligned. In such a situation an unrealistic diffusion "like" solution would result.

Spalding (1972) showed that a stabilizing feature of fluid flows, due to convection, is that downstream events in flows become less influential than upstream ones when the local Peclét number exceeds approximately 2, Harms, von Backström and du Plessis (1996). A deferred correction scheme combines a higher order scheme such as the central difference scheme with a lower order scheme such as the upwind scheme. The lower order scheme is usually treated implicitly while the higher order scheme is treated explicitly or 'deferred' to the source terms in the discretized equation, Khosla and Rubin (1974). The explicit term may also be multiplied by a factor $0.0 \leq \gamma \leq 1.0$, thus blending the two schemes.

The formulation is

$$\phi_n = \left[\left|V_n^{\xi};0.0\right|\right]\frac{1}{V_n^{\xi}}\phi_N + \left[\left|-V_n^{\xi};0.0\right|\right]\frac{1}{-V_n^{\xi}}\phi_{NN}$$

$$+\gamma\left\{(1-f_n)\phi_N + f_n\phi_{NN} - \left[\left|V_n^{\xi};0.0\right|\right]\frac{1}{V_n^{\xi}}\phi_N - \left[\left|-V_n^{\xi};0.0\right|\right]\frac{1}{-V_n^{\xi}}\phi_{NN}\right\} \qquad (3.5)$$

or,

$$\phi_n = \left[\left|V_n^{\xi};0.0\right|\right]\frac{1}{V_n^{\xi}}\phi_N + \left[\left|-V_n^{\xi};0.0\right|\right]\frac{1}{-V_n^{\xi}}\phi_{NN} + S_2 \qquad (3.6)$$

$$S_2 = \gamma\left\{(1-f_n)\phi_N + f_n\phi_{NN} - \left[\left|V_n^{\xi};0.0\right|\right]\frac{1}{V_n^{\xi}}\phi_N - \left[\left|-V_n^{\xi};0.0\right|\right]\frac{1}{-V_n^{\xi}}\phi_{NN}\right\} \qquad (3.7)$$

where S_2 is the interfacial secondary source term arising from the deferred correction approach. The first two terms in equation (3.6) represent an upwind scheme and the remaining source terms account for a central difference scheme and upwind corrections. From the equation it is evident that the upwind scheme corresponds to $\gamma = 0.0$ and a purely central

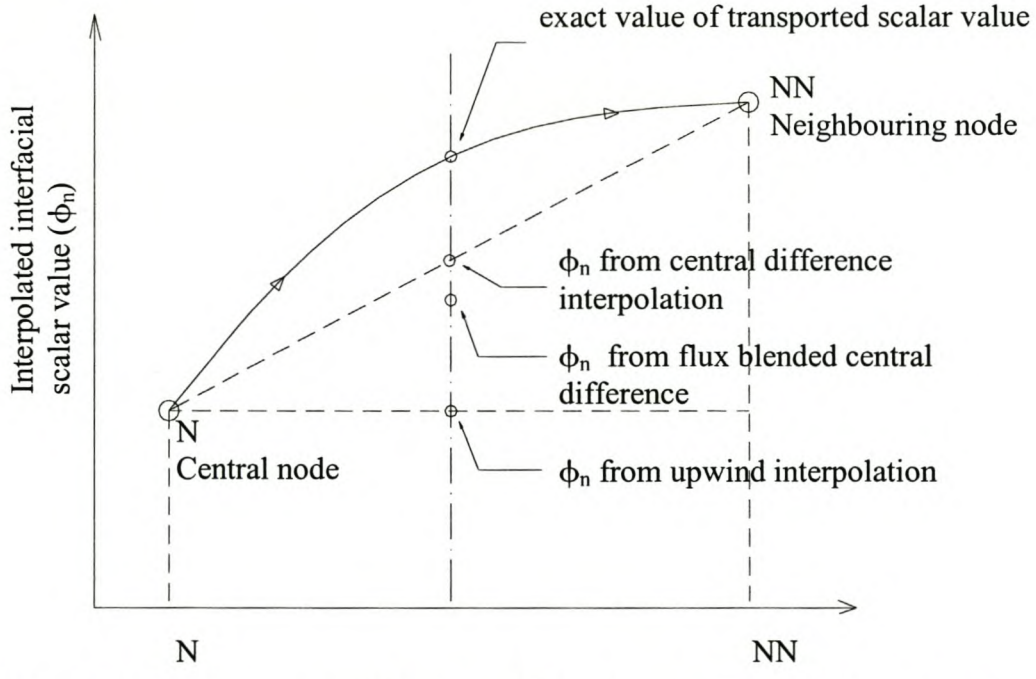

Figure 3.2. Upwinding, central difference and flux blending interpolation schemes.

difference scheme corresponds to $\gamma = 1.0$. Usually values of $\gamma = 0.9$ would suffice. During discretization, the secondary source terms are treated explicitly while the calculation of the implicit influence coefficients employs the upwind scheme. Figure 3.2 is a graphical representation of the interfacial scalar value obtained with the three interpolation schemes mentioned above.

Timin and Esmail (1983) presented a similar scheme where the convective terms are approximated by partial upwind differencing, leading to accurate and stable simulations for $\gamma = 0.9$ i.e. a small upwind contribution balanced by the predominantly central differenced approximation.

The interfacial values of all the explicit quantities, with exception of the interfacial velocity V_n^{ξ}, are found from a central difference approximation. For the Navier-Stokes equations they include the interfacial density

$$\rho_n = (1 - f_n)\rho_N + f_n\rho_{NN} \tag{3. 8}$$

and the interfacial diffusion coefficient

$$\Gamma_n = (1 - f_n)\Gamma_N + f_n\Gamma_{NN} \tag{3. 9}$$

3.3 Discretization of the Momentum Conservation Equations

While most references consulted and listed below always illuminate one aspect or another relation to the subject, the main sources here are Patankar (1980), Perić (1985), Harms (1995) and Ubbink (1997).

3.3.1 Discretization of the flux vector

By employing the integral divergence theorem of Gauss as presented by Greenberg (1998) a volume integral of the divergence of the flux vector $\vec{J}(\phi)$ in equation (2.12) may be transformed into a surface integral of its projection normal to that surface. Equation (2.12) may then be rewritten for a steady state solution as

$$\int_V \vec{\nabla} \cdot \vec{J}(\phi)\ dV = \int_A \vec{J}(\phi) \cdot \vec{n}\ dA = \int_V S(\phi)\ dV \tag{3. 10}$$

where $\vec{n}$ is an unit normal vector to surface A. Thus, for a hexahedral control volume the volume integral is converted into six surface integrals, one for each face of the control volume. These flux vector surface integrals can be approximated for the orthogonal control volume as

$$\int_A \vec{J}(\phi) \cdot \vec{n}\ dA = \sum_{n=1}^{6} \vec{J}(\phi) \cdot \vec{n}\ A_n = \sum_{n=1}^{6} J_n^{\xi}(\phi)\ A_n^{\xi} \tag{3. 11}$$

where $J_n^{\xi}(\phi)$ is the projection of the interfacial flux vector in the direction of the nodal vector $\vec{I}_n^{\xi}$ as per equation (5.16) and A_n^{ξ} denotes the projection of the area vector in the direction of the nodal vector as per equation (5.21). For the non-orthogonal formulation the only addition is a second component or projection of the area and flux vectors along a directional vector ($\vec{\eta}$) normal to the nodal vector ($\vec{\xi}$). This non-orthogonal formulation will be discussed in chapter 5. The interfacial terms in equation (3.11) are subsequently discretized in terms of nodal properties by means of an interpolation scheme.

The nodal positioning system used in this study follows the B-type grids as per Patankar (1980) and as shown in figure 3.3.

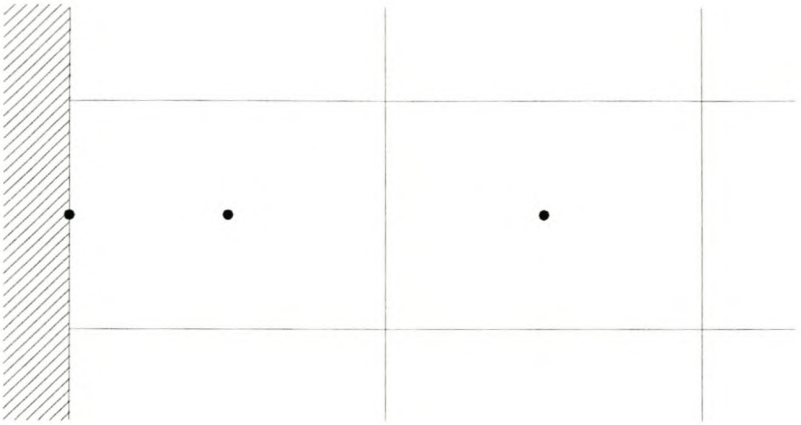

Figure 3.3. B-type grids

For the purpose of the discretization of the momentum equations, assume that a suitable approximation of the interfacial velocity V_n^{ξ} exists. The detailed approximation of this term will be discussed together with the pressure-velocity coupling. The approximation of the interfacial flux scalar is as follows.

The flux scalar as per equation (3.11) is

$$J_n^{\xi} = \rho_n V_n^{\xi} \phi_n - \Gamma_n \nabla \phi_n \tag{3. 12}$$

Since integration takes place along the nodal vector one can approximate the interfacial diffusion term by

$$\Gamma_n \nabla \phi_n = \Gamma_n \frac{\phi_{NN} - \phi_N}{\delta \xi} \tag{3. 13}$$

where $d\xi$ denotes the magnitude of the distance between the central node and the neighbouring node along the interpolation line in question as per Figure 3.1. This formulation ensures the correct sign for the gradient term since the local coordinate system has its zero reference at the central node. Substituting equations (3.1), (3.6), (3.8), (3.9) and (3.13) into equation (3.12) one finds

$$J_n^{\xi} = \left(\left[\left|-Pe_n;0.0\right|\right] + 1.0\right)\frac{\Gamma_n}{\delta\xi}\left(\phi_N - \phi_{NN}\right) + \rho_n V_n^{\xi}\left(\phi_N + S_2\right) \qquad (3.14)$$

where the Pe_n denotes the local interfacial Peclét number.

3.3.2 Discretization of the source terms

The source term in equation (2.12), the primary source term, contains a pressure gradient, cross diffusion terms and additional body force terms as discussed in chapter 2. All source terms are treated explicitly during the solution algorithm, implying that each term within the primary source term needs to be expressed in terms of fluid and flow properties at control volume nodes which remain constant within each iteration. Approximations for the first derivative of nodal pressure (nodal pressure gradient) as well as second derivative terms for nodal diffusion contained within the primary source are to be found from local transformations of projection formulas dealt with in chapter 5.

Approximation of first derivative of pressure.

Each of the three Cartesian momentum conservation equations contains a pressure gradient term in global Cartesian coordinates. Since these terms are integrated over the control volume one needs to find the Cartesian pressure gradient at each node for a given pressure field. At this stage it is necessary to assume that a pressure field was solved by means of a suitable pressure-velocity coupling scheme as discussed later in the text. All the local pressure gradients are found by using equation (5.10) which are then, in turn, used in equation (5.9) to transform the local pressure gradient into a global Cartesian pressure gradient $\frac{\partial p}{\partial x^i}$ at each node. Thus after finite volume integration the pressure gradient term in the primary source term is

$$\int_V \frac{\partial p}{\partial x^i} dV = \left(\frac{\partial p}{\partial x^i}\right)_N Vol_N \qquad (3.15)$$

where the superscript (i) denotes the Cartesian index.

Approximation of second and mixed differentials

The primary source term in the momentum conservation equations (2.9) to (2.11) also contains second derivatives and mixed derivatives. These account for additional normal stresses due to viscosity gradients. These terms are treated explicitly and are found as derivatives of derivatives as per equation (5.11). The momentum contribution from these terms are usually negligible but are relevant for boundary layer flows as well as for turbulent flows where severe viscosity gradients might occur in the vicinity of wall regions.

3.3.3 The discretized equation

After some algebra, the steady state momentum conservation equation for a hexahedral control volume can be written in the following form

$$a_N \phi_N = \sum_{n=1}^{6} a_{NN} \phi_{NN} + S_1 + S_2 \tag{3. 16}$$

where the influence coefficients a_N and a_{NN} denote central node and neighbouring node coefficients defined as

$$a_{NN} = \frac{\Gamma_n}{\delta\xi}\left(\left[\left|-Pe_n;0.0\right|\right] + 1.0\right)A_n^{\xi} \tag{3. 17}$$

$$a_N = \sum_{n=1}^{6} a_{NN} \tag{3. 18}$$

The primary source term derived from the pressure gradient and secondary diffusion terms, can be written as

$$S_1^i = \left(-\frac{\partial p}{\partial x^i}\right) Vol_N + \frac{\partial}{\partial x^j}\left(\Gamma_N \frac{\partial \phi^j}{\partial x^i}\right) Vol_N \tag{3. 19}$$

Furthermore, the secondary source term arising from the deferred correction interpolation can by written as

$$S_2^i = \sum_{n=1}^{6}\left(\left((1-f_n)Pe_n - \left[|Pe_n;0.0|\right]\right)\gamma + Pe_n\right)\frac{\Gamma_n}{\delta\xi}\phi_N^i A_n^\xi$$

$$+ \sum_{n=1}^{6}\left(f_n Pe_n + \left[|-Pe_n;0.0|\right]\right)\frac{\Gamma_n}{\delta\xi}\phi_{NN}^i A_n^\xi \gamma \tag{3. 20}$$

The algebra involved in the above discretization can be found in appendix A. The only additional terms required in equation (3.16) are those arising from the inclusion of the transient terms which will be dealt with below as well as additional interfacial convection and diffusion terms arising from a non-orthogonal control volume formulation. These non-orthogonal convection and diffusion terms are included as tertiary source terms and are explained later in the text.

3.3.4 Discretization of the Transient Term

The transient term in equation (2.12) when integrated over time and volume is

$$\int_V \int_t^{t+\Delta t} \frac{\partial}{\partial t}(\rho\phi)dtdV = \left[(\rho_N\phi_N)^{new} - (\rho_N\phi_N)^{old}\right] Vol_N \tag{3. 21}$$

assuming isentropic nodal property values of ρ and ϕ throughout the control volume.

When integrating the remainder of equation (2.12) across the control volume and over time we need to make an assumption as to the time dependent behaviour of the nodal and interfacial properties. Various possibilities exist but the one used in the present study follows

an implicit scheme i.e. one where the "new" values of ϕ prevail at time $t+\Delta t$. Such integration of equation (2.12) can be written as

$$\int_V \int_t^{t+\Delta t} \frac{\partial}{\partial t}(\rho\phi)\,dt\,dV + \int_V \int_t^{t+\Delta t} \vec{\nabla}\cdot\vec{J}(\phi)\,dt\,dV = \int_V \int_t^{t+\Delta t} S(\phi)\,dt\,dV \tag{3.22}$$

or ultimately using equation (3.21) as

$$\left[\left(\rho_N \phi_N^i\right)^{new} - \left(\rho_N \phi_N^i\right)^{old}\right] Vol_N + \sum_{n=1}^{6} J_n^{\xi}\left(\phi^i\right)^{new} A_n^{\xi}\Delta t = S\left(\phi^i\right)^{new} Vol_N \Delta t \tag{3.23}$$

Again after discretization and grouping similar terms, the discretized governing equation for a transient solution of the momentum equation becomes

$$a_N \phi_N^i = \sum_{n=1}^{6} a_{NN}\phi_{NN}^i + S_1^i + S_2^i \tag{3.24}$$

$$a_{NN} = \frac{\Gamma_n}{\delta\xi}\left(\left[\left|-Pe_n;0.0\right|\right] + 1.0\right) A_n^{\xi} \tag{3.25}$$

$$a_N = \sum_{n=1}^{6} a_{NN} + \frac{\rho^{new} Vol_N}{\Delta t} \tag{3.26}$$

$$S_1^i = \left(-\frac{\partial p}{\partial x^i}\right) Vol_N + \frac{\partial}{\partial x^j}\left(\Gamma_N \frac{\partial \phi^j}{\partial x^i}\right) Vol_N + \frac{\left(\rho_N \phi_N^i\right)^{old} Vol_N}{\Delta t} \tag{3.27}$$

$$S_2^i = \sum_{n=1}^{6}\left(\left((1-f_n)Pe_n - \left[\left|Pe_n;0.0\right|\right]\right)\gamma + Pe_n\right)\frac{\Gamma_n}{\delta\xi}\phi_N^i A_n^{\xi}$$

$$+ \sum_{n=1}^{6}\left(f_n Pe_n + \left[\left|-Pe_n;0.0\right|\right]\right)\gamma\,\frac{\Gamma_n}{\delta\xi}\phi_{NN}^i A_n^{\xi} \tag{3.28}$$

where an explicit transient term containing "old" scalar properties was added to the primary source term and the contribution from the "new" values added to the nodal influence coefficient.

3.4 The Pressure-Velocity Coupling

3.4.1 Background

The general momentum conservation equations provide the set of equations required to solve the velocity field assuming that a pressure field is known. This pressure field can be indirectly specified via the continuity equation as mentioned by Patankar (1980). Thus a coupling should be established between the momentum and mass conservation equations to ensure that once convergence is reached, the velocity field determined by means of the momentum conservation equations, satisfies continuity and presents an exact pressure field. The present study implements a pressure-velocity coupling algorithm employing the Rhie and Chow (1983) interpolation method as presented by Burns and Wilkes (1987).

3.4.2 The pressure correction equation

The discretization of the momentum conservation equations establishes a relation for the nodal transported scalar value, equation (3.24) which can be rewritten as

$$\phi_N^i = \sum_{n=1}^{6} \frac{a_{NN_n} \phi^i_{NN_n}}{a_N} + S' - G_i^j \frac{\partial p}{\partial \xi^j} \qquad (3.29)$$

where S' are the remaining source terms from equation (3.24) after terms containing the Cartesian pressure gradient source term have been extracted and the remainder divided by the nodal influence coefficient a_N. The remaining source terms are terms arising from the deferred correction practice and terms from a non-orthogonal formulation. The coefficient G_i^j are the matrix multiplier or the inverse Jacobian matrix $\bar{J}_i^j$, found from the local transformation of the physical space derivative of pressure, as described in chapter 5, divided by the nodal influence coefficient a_N and integrated over the control volume i.e.,

$$G_i^j = \frac{\bar{J}_i^j}{a_N} Vol_N \qquad (3.30)$$

where subscripts i and j indicate the Cartesian index.

Assuming that a suitable approximation of the interfacial velocity components exists and discretizing the momentum equation on a staggered grid i.e. one where the control volume centers are the faces of the scalar mass control volumes, one finds

$$\left(\phi_N^i\right)_n = \left(\sum_{n=1}^{6} \frac{a_{NN_n}\phi^i_{NN_n}}{a_N}\right)_n + (S')_n - \left(G_i^j \frac{\partial p}{\partial \xi^j}\right)_n \tag{3.31}$$

The crux of the Rhie and Chow method is approximating the interface velocity components on a collocated grid and this will be discussed later. Assuming for the moment that a suitable approximation exists we employ another approximation

$$\left(\frac{\partial \phi}{\partial\left(\frac{\partial p}{\partial \xi^j}\right)}\right)_n \approx \left(\frac{\phi'}{\frac{\partial p'}{\partial \xi^j}}\right)_n \tag{3.32}$$

and differentiate equation (3.31) in terms of pressure changes to find

$$\phi_n'^i = \phi_n^i - \phi_n^{i\,*} = \left(-G_i^j \frac{\partial p'}{\partial \xi^j}\right)_n \tag{3.33}$$

$$p_N = p_N^* + p_N' \tag{3.34}$$

As proposed by Rhie and Chow (1983), the cross differentials appearing in equation (3.33) disappear for nearly orthogonal grids leaving us with

$$\phi_n'^i = \left(-G_i^i \frac{\partial p'}{\partial \xi^i}\right)_n \tag{3.35}$$

thus equation (3.33) but without summation convention. In this study the cross differentials were kept during the update of the interfacial velocity values according to equation (3.33).

The Rhie and Chow interpolation scheme approximates the interfacial properties of equation (3.35) by linear weighted interpolation i.e.

$$\left(-G_i^i \frac{\partial p'}{\partial \xi^i}\right)_n = -\left[(1-f_n)\left(G_i^i \frac{\partial p'}{\partial \xi^i}\right)_N + f_n\left(G_i^i \frac{\partial p'}{\partial \xi^i}\right)_{NN}\right] \tag{3.36}$$

Rewriting the discrete continuity equation in terms of interfacial velocity corrections we have

$$\sum_{n=1}^{6} \rho_n \left(V_n^{*\xi} + V_n'^{\xi}\right) A_n^{\xi} + \sum_{n=1}^{6} \rho_n V_n^{\xi} A_n^{\xi} = 0 \tag{3.37}$$

where the second summation term accounts for non-orthogonal mass flux terms which remain uncorrected. The magnitude of the component of the interfacial velocity correction vector in the direction of the nodal interface vector are found from the scalar product

$$V_n'^{\xi} = \frac{\vec{V}_n' \bullet \vec{I}_n^{\xi}}{\left|\vec{I}_n^{\xi}\right|} \tag{3.38}$$

Substitution of equation (3.36) and (3.38) into (3.37) leads to the discrete pressure correction equation

$$a_N^P p_N' = \sum_{n=1}^{6} Pe_n \frac{\Gamma_n}{\delta\xi} A_n^{\xi} + \sum_{n=1}^{6} a_{NN_n}^P p_{NN}' + \sum_{n=1}^{6} \rho_n V_n^{\eta} A_n^{\eta} \tag{3.39}$$

$$a_{NN_n}^p = \rho_n A_n^{\xi}\left(a_N^{pu} + a_N^{pv} + a_N^{pw}\right) \tag{3.40}$$

$$a_N^p = \sum_{n=1}^{6} a_{NN_n}^p \tag{3.41}$$

$$a_{N_n}^{pu} = -\left[(1-f_n)G_{1N}^1 + f_n G_{1NN}^1\right]\frac{I_{nx}^{\xi}}{\left|\vec{I}_n^{\xi}\right|\delta\xi} \tag{3.42}$$

$$a_{N_n}^{pv} = -\left[(1-f_n)G_{2N}^2 + f_n G_{2NN}^2\right]\frac{I_{ny}^{\xi}}{\left|\vec{I}_n^{\xi}\right|\delta\xi} \tag{3.43}$$

$$a_{N_n}^{pw} = -\left[(1-f_n)G_{3N}^3 + f_n G_{3NN}^3\right]\frac{I_{nz}^{\xi}}{\left|\vec{I}_n^{\xi}\right|\delta\xi} \tag{3.44}$$

3.4.3 The Rhie and Chow interpolation method

The above discrete form of the pressure correction equation, equations (3.39) to (3.44), relies upon the suitable approximation of the interfacial velocity vector. A traditional approach to find the interfacial velocity values contained in equation (3.31) would be simply a linear weighted interpolation scheme namely

$$\phi_n = \overline{\phi_n} = (1-f_n)\phi_N + f_n\phi_{NN} \tag{3.45}$$

Such an approximation of the interfacial velocity components with linear weighted interpolation is well known to lead to pressure and velocity oscillations since it effectively decouples the pressure gradients at even and odd grids. However, the Cartesian velocity components at control volume centers satisfy the momentum conservation as per equation (3.29). These can be written for a control volume with center at node N and for a neighbouring control volume with center node NN

$$\left(\phi_N^i\right)_N = \left(\sum_{n=1}^{6}\frac{a_{NN_n}\phi_{NN_n}^i}{a_N}\right)_N + S_N' - \left(G_i^j\frac{\partial p}{\partial \xi^j}\right)_N \tag{3.46}$$

$$\left(\phi_N^i\right)_{NN} = \left(\sum_{n=1}^{6} \frac{a_{NN_n}\phi^i_{NN_n}}{a_N}\right)_{NN} + S'_{NN} - \left(G_i^j \frac{\partial p}{\partial \xi^j}\right)_{NN} \tag{3.47}$$

or in short hand as

$$\phi_N + (B\nabla P)_N = (A\phi)_N + S_N \tag{3.48}$$

$$\phi_{NN} + (B\nabla P)_{NN} = (A\phi)_{NN} + S_{NN} \tag{3.49}$$

The chequerboarding phenomena can be avoided by using a staggered grid on which velocity components are obtained by discretizing the momentum equations on control volumes whose centers are the faces of the mass control volumes. This leads to a discretized equation of the form

$$\phi_n + (B\nabla P)_n = (A\phi)_n + S_n \tag{3.50}$$

similar to our equation (3.31) already established in determining the pressure correction equation.

The staggered grid has the distinct disadvantage in that it makes discretisation more difficult for complex, non-orthogonal three-dimensional grids. The Rhie and Chow interpolation method overcomes this by maintaining the collocated computational grid by employing weighted linear interpolation of terms in equations (3.46) and (3.47) to approximate the terms on the right hand side of equation (3.50)

$$\phi_n + (B\nabla P)_n = (1-f_n)(A\phi)_N + f_n(A\phi)_{NN} + (1-f_n)S_N + f_n S_{NN} = \overline{\phi_n} + \overline{(B\nabla P)_n} \tag{3.51}$$

where the overbar denotes weighted linear interpolation. Assuming that $B_n = \overline{B_n}$ and that $\overline{(B\nabla P)_n} \approx \overline{B_n}\ \overline{\nabla P_n}$ we find the Rhie and Chow interpolation

$$\phi_n = \overline{\phi_n} + \overline{B_n}\left(\overline{\nabla P_n} - (\nabla P)_n\right) \tag{3. 52}$$

or

$$\phi_n = \overline{\phi_n} + \overline{G^j_{in}}\left(\overline{\left(\frac{\partial p}{\partial \xi^j}\right)_n} - \left(\frac{\partial p}{\partial \xi^j}\right)_n\right) \tag{3. 53}$$

Equation (3.53) is used to update the interfacial velocity values after the new nodal values were calculated from the discretized momentum equations. It was found that this formulation effectively eliminated the appearance of a pressure-velocity decoupling or chequerboarding, as present when a purely central difference interpolation scheme was employed.

4. SOLUTION ALGORITHM

4.1 Solving the Discretized Equations

The preceding chapters dealt with the discretization of the governing transport equations and the conservation of mass by means of a pressure-velocity coupling scheme. The result of the discretization of the conservation equations is a set of non-linear algebraic equations which needs to be solved repeatedly by means of some iterative scheme. Various methods exist to compute the field solution and these methods may be divided into direct and iterative methods. Direct methods such as Gauss elimination, LU-decomposition and the Thomas Algorithm (TDMA) can be employed to solve systems of linear equations but are usually computationally intensive. The solution of non-linear equations require iterative methods but these methods may be applied to linear sets as well. As mentioned by Ferziger and Perić (1996), the discretization errors arising from different interpolation schemes are usually much higher than the accuracy of the computer arithmetic and an iterative solution may be used as an alternative to the direct solution. The present study employs the strongly implicit procedure (SIP) of Stone (1968) as extended and presented by Leister and Perić (1994) and as explained in this chapter. This extended iterative solver is applicable to seven-diagonal influence coefficient matrices arising from the central difference approximations employed in the discretization of the three-dimensional governing equations. Due to the non-linear coupling of the set of partial differential equations, outer iterations are required to update the influence coefficients and the source terms. Solutions for each of the primary field variables are iteratively calculated within inner iterations within the solver. As available in many commercial CFD codes, the code presented here employs the SIMPLE algorithm with the SIP solver to calculate the primary field variables.

4.2 The SIP Solver

The linear algebraic set of equations resulting from the discretization of the three-dimensional conservation equations for a hexahedral control volume has the general form

$$a_N \phi_N + \sum_{NN=1}^{6} a_{NN} \phi_{NN} = Q_N \tag{4. 1}$$

or

$$A(\phi) = Q \tag{4. 2}$$

where a_{NN} denotes the influence coefficient for neighbouring node NN, A is the square matrix of influence coefficients, (ϕ) is the vector matrix of the transported scalar while the primary, secondary and tertiary source terms are grouped in matrix Q.

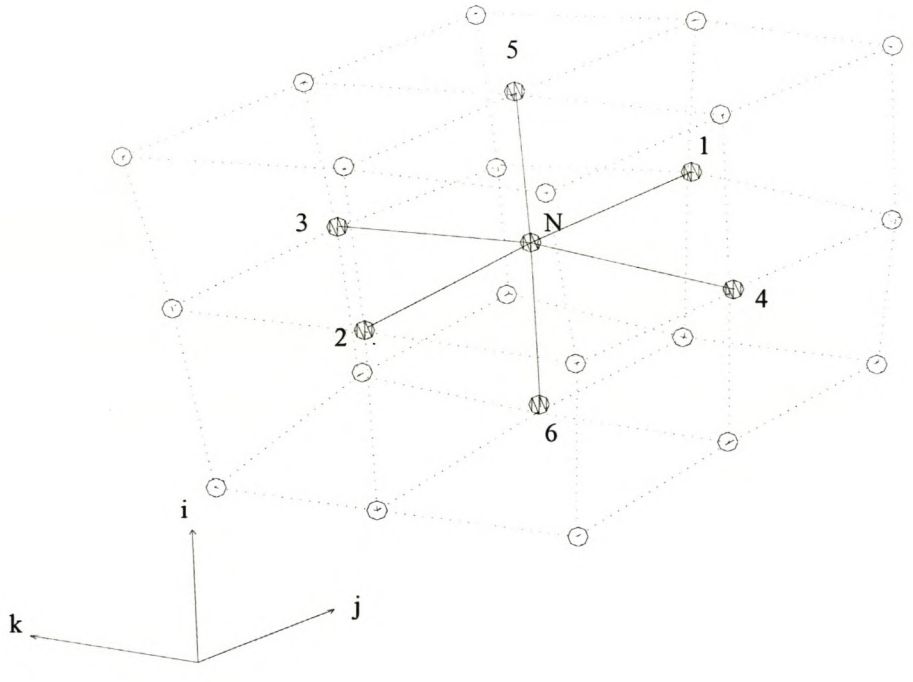

Figure 4.1. Computational molecule

All the terms with a similar neighbouring index number may be stored in a one-dimensional vector according to a index numbering scheme given by Ferziger and Perić (1996) namely,

$$\ell = (i-1)N_j N_k + (k-1)N_j + j \qquad (4.3)$$

where N_j and N_k denote the maximum number of nodes in the j and k direction respectively. As illustrated by figure 4.1, node 1 of the computational molecule lies in the direction of increasing j-index, node 3 along increasing k-index and node 5 along increasing i-index. The conversion of grid indices (j,k,i) into one-dimensional storage locations for the vectors are as per table 4.1

Table 4.1 Conversion of grid indices

Grid location	Corresponding face number	Storage location
j,k,i	P	ℓ =(i-1)$N_j N_k$+(k-1)N_j+j
j+1,k,i	1	ℓ+1
j-1,k,i	2	ℓ-1
j,k+1,i	3	$\ell+N_j$
j,k-1,i	4	$\ell-N_j$
j,k,i+1	5	$\ell+N_j N_k$
j+1,k,i-1	6	$\ell-N_j N_k$

Other formulations are also possible. Equation 4.2 can be rewritten in terms of one-dimensional index numbering as

$$a_{\ell-N_k N_j}\phi_{\ell-N_k N_j} + a_{\ell-Nj}\phi_{\ell-N_j} + a_{\ell-1}\phi_{\ell-1} + a_\ell\phi_\ell + a_{\ell+1}\phi_{\ell+1} + a_{\ell+N_j}\phi_{\ell+N_j} + a_{\ell+N_k N_j}\phi_{\ell+N_k N_j} = Q_\ell \qquad (4.4)$$

This formulation for the ordering or indexing of matrix terms allows one to store the influence coefficient and nodal source term information in one-dimensional arrays rather than three-

dimensional arrays. Following the index ordering scheme as per table 4.1 and equation (4.4) the structure of equation (4.2) is as illustrated by figure 4.2, Leister and Perić (1994).

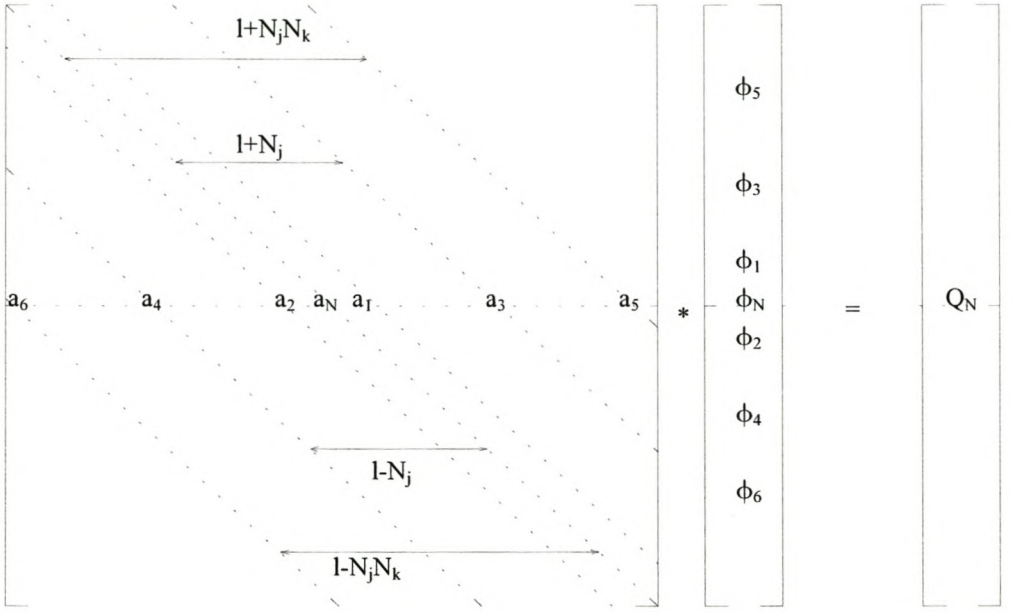

Figure 4.2. Structure of matrix for seven point computational volume

A general iterative scheme for a linear system of equations may be written as

$$M\phi^{n+1} = N\phi^{n} + B \qquad (4.5)$$

where n is the inner iteration counter. Equation (4.5) must satisfy equation (4.2) when convergence is reached. Since at convergence one finds

$$\phi^{n+1} = \phi^{n} = \phi \qquad (4.6)$$

one may write

$$A = M - N \text{ and } Q = B.$$

Equation (4.5) may also be written as

$$M\delta^n = \rho^n \tag{4. 7}$$

where

$$\delta^n = \left(\phi^{n+1} - \phi^n\right) \tag{4. 8}$$

denotes the change of the transported variable ϕ from iteration n to n+1 and

$$\begin{aligned}\rho^n &= B - (M - N)\phi^n \\ &= Q - A\left(\phi^n\right)\end{aligned} \tag{4. 9}$$

is the residual after the n^{th} iteration. An iteration matrix M needs to be approximated from matrix A. The closer the matrix M is to A, the more efficient the scheme will be. The SIP method of Stone, approximate the matrix A by means of an incomplete LU-decomposition

$$M = L \cdot U = A + N \tag{4. 10}$$

where L and U are the upper and lower triangular matrices which has non-zero diagonals only on the corresponding diagonals of matrix A. Setting the main diagonal on the upper triangular matrix U equal to unity, the elements of the L and U matrices can be calculated. Such an incomplete LU-decomposition results in extra diagonals in the $L \cdot U$ product matrix M. Therefore the resultant matrix N is not zero. The essence of the SIP solver of Stone is minimizing matrix N by providing a contribution in $N(\phi)$ such that the contribution of the additional non-zero diagonals in M, not present in A, is partially canceled leading to

$$N(\phi) \approx 0 \tag{4. 11}$$

The key to ensuring that the condition of equation (4.11) is met is to find the elements of N by approximating the additional nodal values found in M in terms of the principal nodal values. This gives the elements of matrix N in equation (4.11) in terms of the additional elements of M. Finally, since all the elements of M are found from the LU decomposition and by using equation (4.10) one finds the elements of L and U as given by Leister and Perić (1994)

$$
\left.
\begin{aligned}
L_{6,\ell} &= \frac{A_{6,\ell}}{\left[1+\alpha\left(U_{1,\ell-N_jN_k}+U_{3,\ell-N_jN_k}\right)\right]} \\
L_{4,\ell} &= \frac{A_{4,\ell}}{\left[1+\alpha\left(U_{1,\ell-N_j}+U_{3,\ell-N_j}\right)\right]} \\
L_{2,\ell} &= \frac{A_{2,\ell}}{\left[1+\alpha\left(U_{1,\ell-1}+U_{3,\ell-1}\right)\right]} \\
H_1 &= \alpha\left(L_{6,\ell}U_{1,\ell-N_jN_k}+L_{4,\ell}U_{1,\ell-N_j}\right) \\
H_2 &= \alpha\left(L_{6,\ell}U_{3,\ell-N_jN_k}+L_{2,\ell}U_{3,\ell-1}\right) \\
H_3 &= \alpha\left(L_{4,\ell}U_{5,\ell-N_j}+L_{2,\ell}U_{5,\ell-1}\right) \\
L_{N,\ell} &= A_{N,\ell}+H_1+H_2+H_3-L_{6,\ell}U_{5,\ell-N_jN_k}-L_{4,\ell}U_{3,\ell-N_j}-L_{2,\ell}U_{1,\ell-1} \\
U_{1,\ell} &= \frac{A_{1,\ell}-H_1}{L_{N,\ell}} \\
U_{3,\ell} &= \frac{A_{3,\ell}-H_2}{L_{N,\ell}} \\
U_{5,\ell} &= \frac{A_{5,\ell}-H_3}{L_{N,\ell}}
\end{aligned}
\right\} \qquad (4.12)
$$

where $0 \le \alpha \le 1$. These equations are solved in the order given above. The matrix M in equation (4.7) now consists of the upper and lower triangular matrices, L and U, and equation

(4.7) may be solved by the standard LU-decomposition solution procedure, firstly calculating the vector matrix

$$V^n = L^{-1}\rho^n$$

$$= \left(\rho_\ell^n - L_{6,\ell} V^n_{\ell-N_jN_k} - L_{4,\ell} V^n_{\ell-N_j} - L_{2,\ell} V^n_{\ell-1}\right) / L_{N,\ell} \qquad (4.13)$$

where the residual error is

$$\rho_\ell^m = Q_\ell - A_{N,\ell}\phi^n_\ell - A_{3,\ell}\phi^n_{\ell+N_j} - A_{4,\ell}\phi^n_{\ell-N_j} - A_{1,\ell}\phi^n_{\ell+1}$$

$$- A_{2,\ell}\phi^n_{\ell-1} - A_{5,\ell}\phi^n_{\ell+N_jN_k} - A_{6,\ell}\phi^n_{\ell-N_jN_k} \qquad (4.14)$$

and then calculating the increment vector matrix,

$$\delta^n = U^{-1}V^n$$

$$= \left(V^n_\ell - U_{1,\ell}\delta^n_{\ell+1} - U_{3,\ell}\delta^n_{\ell+N_j} - U_{5,\ell}\delta^n_{\ell+N_jN_k}\right) \qquad (4.15)$$

The primary variable required may now be found by employing equation (4.8) and (4.15). The elements of the upper and lower triangular matrices L and U are calculated once and then equations (4.13) to (4.15) are solved iteratively until the convergence criteria based on the residual error is met. It was found that the most accurate results were obtained when the inner iterations were continued until the residual error had decreased to approximately 10% of its initial value at the start of iterations.

4.3 The SIMPLE Algorithm

The solution algorithm applied in this study follows the Semi Implicit Method for Pressure-Linked Equations or SIMPLE algorithm as presented by Patankar (1980) and described by Patankar and Spalding (1972).

The sequence of operations performed during the calculation of the field solution is,

1. Assign initial field primary variables
2. Calculate the influence coefficients and source terms of the momentum equations and solve these to obtain the three Cartesian velocity components u^*, v^*, w^*.
3. Compute the interfacial velocity values
4. Calculate the pressure correction equation influence coefficients and source terms and solve the solution matrix to find the pressure correction values p'.
5. Update the pressure field with the new pressure correction values.
6. Calculate the interfacial velocity correction values and update the interfacial velocity values.
7. Solve the discretization equations for other variables such as temperature and turbulence quantities.
8. Evaluate the global convergence criteria and if they have not been met then return to step 2.

4.4 Boundary Conditions

The boundary conditions found and applied in this study includes boundary conditions for primary variables i.e. temperature, pressure, velocity, turbulent kinetic energy and turbulent dissipation rates. These boundaries are found at and classed as either inlet, outlet, wall or symmetry boundaries. The boundary conditions are updated after the momentum equations have been solved as well as after the new pressure field has been calculated during the solution algorithm.

4.4.1 Inlet boundary condition

The boundary values for all variables at the inlet are specified except for the pressure and the turbulent quantities. These Dirichlet type boundary conditions include the velocity components (u,v,w) and the inlet temperature (T). The pressure at the inlet node is found from a linear extrapolation of the pressure values at the two inner nodes. For inlet turbulence quantities Ferziger and Perić (1996) suggests that, in the absence of values found from

experimental measurement or full field numerical models, an assumption can be made that the inlet turbulent intensity is low and typically of the order $10^{-4}\bar{u}^2$. The inlet dissipation rate is then calculated from equation (4.12) such that the length scale, L, is approximately one tenth of the shear layer

$$\varepsilon = \frac{k^{1.5}}{L} \tag{4. 16}$$

The turbulence quantities employed in this study and found to be suitable is similar to those found in the CFX software from AEA Technology namely

$$k_{in} = 1.5\left(i_k u_{in}\right)^2 \tag{4. 17}$$

and

$$\varepsilon_{in} = \frac{k_{in}^{1.5}}{0.3 d_e} \tag{4. 18}$$

where i_k is the turbulence intensity with values typically between 1% and 10%.

4.4.2 Outlet boundary condition

Neumann boundary conditions are specified at the outlet for all variables. This study employs a forward difference interpolation for the approximation for the Neumann gradients. Zero gradients along grid lines are assigned for the velocity field. The velocity component in the direction of the flow is also mass flux corrected. This means that the velocity value at the outlet node is multiplied by the ratio of the mass flux at the inlet and the outlet mass flux. Pressure is again extrapolated from upstream values. Zero normal gradients are also specified for outlet temperature values and turbulent quantities.

4.4.3 Wall boundary condition

At the walls the no-slip boundary condition is applied which assumes that the fluid at the wall assumes the velocity of the wall. It was found to be adequately accurate to apply a Dirichlet type boundary condition, $u = v = w = 0$, for the velocity field at a stationary wall. The Neumann boundary condition of zero normal gradient is applied to the wall pressure, again using the forward difference interpolation for the approximation of the gradient. Wall thermal boundaries may either be isothermal, adiabatic or with given heat flux and energy source values. For adiabatic walls a zero normal temperature gradient is applied at the wall. For an isothermal wall, a Dirichlet type boundary assigns a temperature value to the wall node. With given heat flux and energy sources specified at the wall, the wall boundary condition is found from the application of an energy balance at the wall node.

4.4.4 Symmetry planes

Zero normal gradients are applied to all variables at symmetry planes. Furthermore, zero flux normal to the symmetry plane is enforced by assigning a zero magnitude to the interfacial velocity vector normal to the symmetry plane. To eliminate possible shear stresses at the symmetry plane a small viscosity value (1.0E-12) was assigned to the interfacial viscosity at the wall.

4.4.5 Solid regions

Only the energy equation is solved for solid regions. Therefore only temperature boundary conditions are required at solid/solid boundaries. At solid/fluid interfaces the temperature is either given or calculated as mentioned in paragraph 4.4.3 for wall boundary conditions. When a solid region temperature boundary is not explicitly given or calculated then the Neumann boundary condition of zero normal gradient is applied.

4.5 Relaxation

The relaxation factor employed for a typical transported variable ϕ is similar to suggestions by Patankar (1980) i.e.

$$\phi = \alpha\phi_{new} + (1-\alpha)\phi_{old} \tag{4. 19}$$

Multiplying equation (4.19) by a_N / ϕ_N and substituting the result into the discretized equation , equation (3.16), one finds, as presented by Harms (1995)

$$\frac{a_N\phi_N}{\alpha} = \sum_{n=1}^{6} a_{NN}\phi_{NN} + S_1 + S_2 + \frac{(1-\alpha)}{\alpha} a_N\phi_{N_{old}} \tag{4. 20}$$

which essentially introduces a larger central node influence coefficient into the solution matrix. The same relaxation may be achieved by employing small time steps when solving the transient state discretized momentum equation. This would also introduce larger central node influence coefficients in the solution matrix as mentioned above.

Relaxation for the pressure correction is applied as per Patankar (1980) and modifying equation (3.34) i.e.

$$p = p_N^* + \alpha p_N' \tag{4. 21}$$

No relaxation is applied to interfacial velocity corrections. It was found that the stability of the solution is enhanced by adding relaxation to the outlet flux corrected velocity boundary condition. This ensured that the upstream velocity field information has sufficient time to influence the outlet velocity field during early stages of the iterations.

Relaxation was also added to the turbulence parameters wall boundary conditions. This allowed the calculation of the wall kinetic energy and dissipation rates to be governed by the

field solution thus ensuring that high temporary kinetic energy and dissipation rate gradients at the walls are eliminated during early stages of the iterations.

The application of the SIMPLE algorithm with the SIP solver was found to be highly accurate requiring very few inner iterations to reach convergence during the solution of the general transport equations. These inner iterations rarely exceed 5 except during the solution of the pressure correction equation. The pressure correction equation as applied in the present study seemed highly susceptible to instabilities and difficulties were experienced in reaching convergence within the set number of inner iterations. Relaxation of the pressure correction central node influence coefficient relieved this problem at the cost of computing time. It is suggested that future studies investigate the implementation of a combination of a multi-grid method and the SIP solver. This may save considerable processing time and would not require serious modification to the present code. The addition of another solution algorithm such as SIMPLEC may also decrease the convergence time by establishing more effective coupling between pressure and velocity corrections. Although somewhat time-consuming the present solution algorithm, the SIP solver and the pressure correction scheme was found to be highly accurate and generally robust for all the numerical simulations presented in this study.

5. NON-ORTHOGONAL FINITE VOLUME FORMULATION

5.1 Introduction

The governing equations described in Chapter 2, are presented in the reference Cartesian coordinate frame (x,y,z), as opposed to a general non-orthogonal coordinate system (ξ,η,ζ). The latter coordinate system lends itself to the description of applications with complex boundaries and non-orthogonal grid formations whereas the first is restricted to the description of simple or simplified geometries. Since few of the problems encountered in the numerical modeling field poses simple geometries one needs to address the transformation of the governing equations to assist their solution in a non-orthogonal coordinate frame. The physical space is described by the boundaries and for complex geometries these are often discontinuous functions giving rise to difficulties in maintaining orthogonal control volumes. One approach deals with the global transformation of the discretised equations in physical space to a general, non-orthogonal space but has the limitation that the physical space or the boundaries must be represented by a continuous mathematical description. On the other hand the use of a Cartesian base vector system simplifies the discretised equations and facilitates our understanding and interpretation of the physical quantities contained in them. The global Cartesian coordinate frame can be maintained by employing a local transformation approach i.e. one where interfacial quantities are obtained from vector projections. The present study maintains a global Cartesian frame with local non-orthogonal transformations of control volume vectors and source terms present in the governing equations as outlined by Perić (1985) and Harms (1995)

5.2 The Control Volume Convention and Notation

The control volume conventions and notations used in this study are as illustrated by figure 5.1. The hexahedral control volume with central node (N) has six neighbouring control volumes, each with neighbouring node (NN). A primary interfacial vector or nodal vector $\vec{I}_n^{\xi}$ extends from the central node N outwards towards each of the neighbouring nodes NN. Six area vectors $\vec{A}_n$, describe the magnitude and direction of each of the six interfacial areas

encountered on the control volume. For an orthogonal control volume formulation these area vectors would have the same directions as the nodal vectors i.e. their scalar products would equal zero.

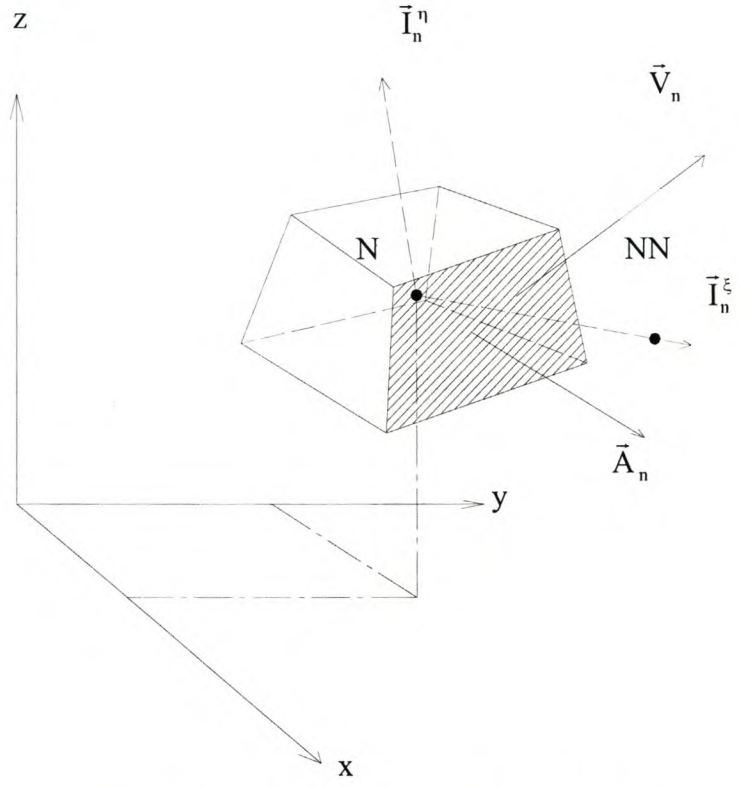

Figure 5.1. Control volume conventions and notations

For fluid flow, the interfacial velocity vector $\vec{V}_n$ describes the interfacial direction and velocity of the flow field in a global Cartesian coordinate frame. The coordinate convention follows a right handed system where (ξ) denotes the nodal vector direction and (η) a direction normal to that. Each local coordinate system has a zero reference position at the control volume central node N.

5.3 Vector Algebra Fundamentals

The basis for the local transformation approach lies in the fundamentals of vector algebra as described by various authors such as Kreyzig (1988) and Greenberg(1998). In this section the basic principles of vector algebra will be reviewed.

5.3.1 Divergence and the gradient vector

The divergence of a vector field $\vec{V}$, can be expressed in the form

$$\text{div}\phi = \vec{\nabla} \cdot \vec{V} \tag{5. 1}$$

with $\vec{\nabla}$ being the vector differential operator given in Cartesian coordinates by

$$\vec{\nabla} = \frac{\partial}{\partial x}\underline{i} + \frac{\partial}{\partial y}\underline{j} + \frac{\partial}{\partial z}\underline{k} \tag{5. 2}$$

It can also be shown that the gradient vector, $\vec{\nabla}\phi$, of the scalar field $\phi(x, y, z)$, points in the direction of maximum increasing ϕ, its magnitude being equal to the directional derivative $\frac{\partial \phi}{\partial n}$ in that direction.

The magnitude of the gradient in any direction from the maximum gradient vector is obtained from the scalar product of the gradient vector and a unit vector in the required direction ($\vec{\xi}$)i.e.

$$\vec{\nabla}\phi \cdot \vec{\xi} = \frac{\partial \phi}{\partial x}\xi_x + \frac{\partial \phi}{\partial y}\xi_y + \frac{\partial \phi}{\partial z}\xi_z \tag{5. 3}$$

This study employs the following tensor notation for our description of the local coordinate transformation as presented by Burns and Wilkes (1987).

$\left(x^i\right)$ = Cartesian physical space coordinates (5. 4)

$\left(\xi^i\right)$ = General non-orthogonal computational space coordinates (5. 5)

$$J^i_j = \frac{\partial x^i}{\partial \xi^j} = \begin{bmatrix} \frac{\partial x^1}{\partial \xi^1} & \frac{\partial x^2}{\partial \xi^1} & \frac{\partial x^3}{\partial \xi^1} \\ \frac{\partial x^1}{\partial \xi^2} & \frac{\partial x^2}{\partial \xi^2} & \frac{\partial x^3}{\partial \xi^2} \\ \frac{\partial x^1}{\partial \xi^3} & \frac{\partial x^2}{\partial \xi^3} & \frac{\partial x^3}{\partial \xi^3} \end{bmatrix} = \text{Jacobian matrix} \tag{5. 6}$$

$$\bar{J}^i_j = \frac{\partial \xi^i}{\partial x^j} = \left(J^{-1}\right)^i_j = \text{Inverse Jacobian matrix} \tag{5. 7}$$

The main importance of the Jacobian is that it relates geometrical derivatives in physical space to derivatives in computational space as follows

$$\frac{\partial \phi}{\partial \xi^i} = \frac{\partial x^j}{\partial \xi^i}\frac{\partial \phi}{\partial x^j} = J^j_i \frac{\partial \phi}{\partial x^j} \tag{5. 8}$$

and

$$\frac{\partial \phi}{\partial x^i} = \frac{\partial \xi^j}{\partial x^i}\frac{\partial \phi}{\partial \xi^j} = \bar{J}^j_i \frac{\partial \phi}{\partial \xi^j} \tag{5. 9}$$

of which equation (5.9) is the most important since it expresses derivatives in physical space, as used in the discretised equations, in terms of derivatives in computational space. Thus it is important to be able to obtain numerical approximations of the inverse Jacobian matrix. The derivation of equation (5.9) can be found in appendix B.

5.3.2 Obtaining first, second and mixed derivatives

Once the local geometrical gradients in equation (5.6) are found, it is a matter of obtaining the local nodal property gradients i.e. $\frac{\partial \phi}{\partial \xi^j}$, approximated by means of a suitable interpolation

scheme, and transform those to the physical space by means of equation (5.9). The approximation used in this study for the local nodal property gradients is a linear interpolation, for example

$$\frac{\partial \phi}{\partial \xi^1} = \frac{\phi_1 - \phi_2}{\Delta \xi^1} \tag{5. 10}$$

where ϕ_1 denotes the interfacial scalar property at face 1, ϕ_2 denotes an interfacial scalar property at face 2 and $\Delta\xi^1$ the magnitude of the distance between interpolation points on faces 1 and 2. The interfacial properties are again found from an approximation between neighbouring nodal values by means of a suitable interpolation scheme. All other local first derivatives present in equation (5.9) are found in a similar manner.

Second derivatives and mixed derivatives are found in the governing equations and may be obtained from derivatives of derivatives which are again generated by means of equation (5.9). Thus one initially finds the global Cartesian first derivative from equation (5.9), and then proceeds to find the local second derivative or mixed derivative of this value by employing equation (5.9) again. The resulting operation can be rewritten as,

$$\frac{\partial}{\partial x^k}\left(\frac{\partial \phi}{\partial x^j}\right) = \frac{\partial \xi^k}{\partial x^i} \frac{\partial\left(\frac{\partial \phi}{\partial x^j}\right)}{\partial \xi^k} = \bar{J}_i^k \frac{\partial\left(\frac{\partial \phi}{\partial x^j}\right)}{\partial \xi^k} \tag{5. 11}$$

5.3.3 Calculation of interface fluxes

The interface flux vector $\vec{J}$ in equation (2.12) contains interfacial convection and diffusion contributions. To ensure that the flux vector maintains the momentum conservation within the control volume one needs to account for orthogonal as well as non-orthogonal components. By aligning the interfacial area and velocity vector with the nodal vector there remains non-orthogonal flux contributions that need to be accounted for. For orthogonal grids these

contributions are eliminated since they lie in the interface plane and thus do not contribute to the flux passing through that plane. The total flux contribution across an interfacial area can be found from the scalar product of the flux vector and the vector normal to the area as per equation (3.11). Since the orthogonal flux components and area vectors are aligned with the interfacial nodal vectors, a non-orthogonal control volume requires a second non-orthogonal flux component to be added to equation (3.11) namely

$$\sum_{n=1}^{6} \vec{J}(\phi) \cdot \vec{n}\ A_n \cdot \vec{n} = \sum_{n=1}^{6} \vec{J}_n^{\xi}(\phi) A_n^{\xi} + \sum_{n=1}^{6} \vec{J}_n^{\eta}(\phi) A_n^{\eta} \qquad (5.12)$$

The additional non-orthogonal components represented by the second term on the right in equation (5.14) are treated explicitly as tertiary source terms in the discretized momentum equations. After integration over the control volume, the non-orthogonal interfacial convection contribution to the flux amounts to

$$\rho_n \phi_n V_n^{\eta} A_n^{\eta} = \rho_n \phi_n \frac{\vec{V}_n \bullet \vec{I}_n^{\eta}}{\left|\vec{I}_n^{\eta}\right|} \cdot \frac{\vec{A}_n \bullet \vec{I}_n^{\eta}}{\left|\vec{I}_n^{\eta}\right|} \qquad (5.13)$$

The interfacial scalar property ϕ_n in equation (5.13) is approximated by linear weighted interpolation.

Since the orthogonal diffusion contribution in the flux vector has already been dealt with, we only need to add the non-orthogonal component of the interfacial gradient vector to the tertiary source i.e. the magnitude of the component of $\vec{\nabla}\phi_n$ in the direction of the non-orthogonal vector. This is found from the scalar product

$$\Gamma_n \nabla\phi_n^{\eta} A_n^{\eta} = \Gamma_n \frac{\vec{\nabla}\phi_n \bullet \vec{I}_n^{\eta}}{\left|\vec{I}_n^{\eta}\right|} \cdot \frac{\vec{A}_n \bullet \vec{I}_n^{\eta}}{\left|\vec{I}_n^{\eta}\right|} \qquad (5.14)$$

The resultant tertiary source term that arises from the discretization can then be compiled as

$$S_3 = -\sum_{n=1}^{6} \rho_n \left[(1 - f_n)\phi_N + f_{NN}\phi_{NN} \right] V_n^{\eta} A_n^{\eta} + \sum_{n=1}^{6} \Gamma_n \nabla\phi_n^{\eta} A_n^{\eta} \qquad (5.15)$$

5.4 Calculation of Geometrical Parameters

5.4.1 Interfacial orthogonal and non-orthogonal directional vectors

As mentioned previously, one requires the interfacial directional vectors to facilitate the flux split method represented by equation (5.12). The global Cartesian components of the orthogonal interfacial vector $\vec{I}_n^{\xi}$ is found from geometrical differences between the control volume neighbouring node and the central node i.e.

$$\vec{I}_n^{\xi} = \left(x_{NN} - x_N ; y_{NN} - y_N ; z_{NN} - z_N \right) \qquad (5.16)$$

It has been shown by Jasak (1996), as reported by Ubbink (1997), that the non-orthogonal interfacial vector may be found from the following vector difference

$$\vec{I}_n^{\eta} = \vec{A}_n - \frac{\vec{A} \bullet \vec{I}_n^{\xi}}{\left| \vec{I}_n^{\xi} \right|} \cdot \frac{\vec{I}_n^{\xi}}{\left| \vec{I}_n^{\xi} \right|} \qquad (5.17)$$

This ensures that the resulting single non-orthogonal interfacial directional vector is normal to the orthogonal directional vector and is eliminated for orthogonal grids. One does not require the magnitude of the directional vectors since one merely employs these vectors in a normalised form to facilitate the flux split method described above.

5.4.2 Control volume face areas

For the calculation of the six facial areas of a hexahedral control volume refer to figure 5.2. Each face, such as face 1 in figure 5.2, contains two triangles, each of which is enclosed by two vectors.

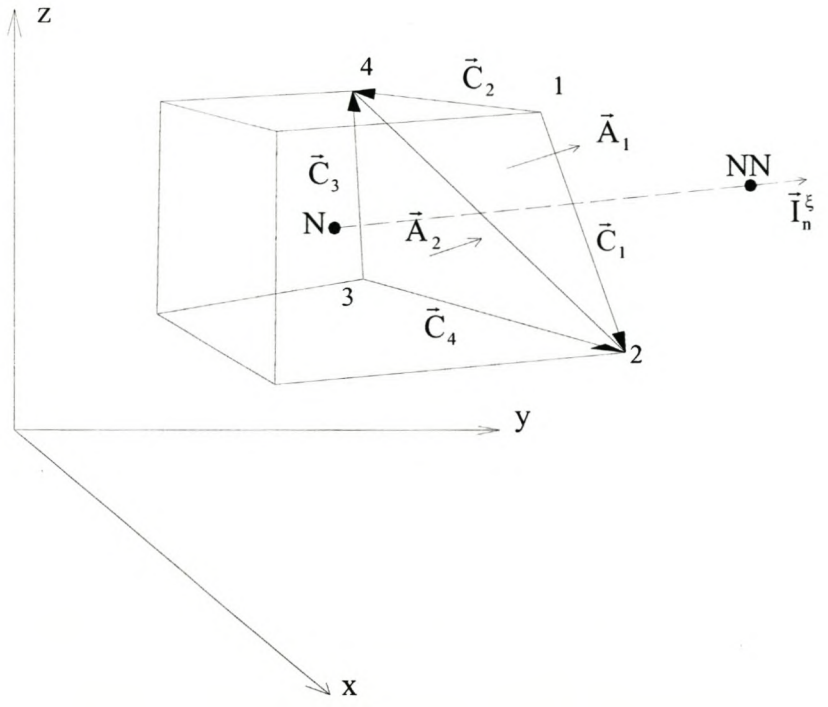

Figure 5.2. Control volume area cross vectors

The definition of the two cross vectors for each triangle is such that the cross product of them results in a third vector pointing out of the control volume and of which the magnitude is equal to the area of the parallelogram. It is important that the cross vectors are defined such that their cross product point out of the control volume.

Table 5.1. Control volume corner vector convention

Corner vector	Spanning nodes	Positive direction
$\vec{C}_1$	1,2	$1 \rightarrow 2$
$\vec{C}_2$	1,4	$1 \rightarrow 4$
$\vec{C}_3$	3,4	$3 \rightarrow 4$
$\vec{C}_4$	3,2	$3 \rightarrow 2$

Table 5.1 describes the convention for determining corner numbers, vectors and vector directions, to ensure positive area vectors pointing outwards. The corner vertices are always numbered from 1 to 4 in a rotational manner consistent with the right hand rule. For example, the vector spanning corners 1 and 2 is vector $\vec{C}_1$ which points from corner 1 to corner 2, and vector $\vec{C}_3$ spans corners 3 and 4 and pointing from 3 to 4.

The total area vector of the face is then defined as the vector sum of the area vectors of the two triangles. This implies an underlying assumption that the area vector for a face is the average of the two triangular area vectors defined by that face. Thus for a typical face (n), the two triangular area vectors are

$$\vec{A}_1 = \frac{1}{2}\left(\vec{C}_1 \times \vec{C}_2\right) \tag{5. 18}$$

$$\vec{A}_2 = \frac{1}{2}\left(\vec{C}_3 \times \vec{C}_4\right) \tag{5. 19}$$

both pointing outwards according to the right hand rule. The total face area vector is simply

$$\vec{A}_N = \vec{A}_1 + \vec{A}_2 \tag{5. 20}$$

and the face area is the magnitude of the area vector. For the local transformation approach one would typically require the projection of the area vector in the direction of the nodal vector i.e.

$$A_n^{\xi} = \frac{\vec{A}_n \bullet \vec{I}_n^{\xi}}{\left|\vec{I}_n^{\xi}\right|} \qquad (5.21)$$

5.4.3 Three dimensional non-orthogonal control volume

A typical three dimensional control volume, as shown in figure 5.3, consists of six faces each defined by four vertices that do not generally lie in the same plane but which are joined by straight lines. Such a volume can be decomposed into six tetrahedral volumes as shown in

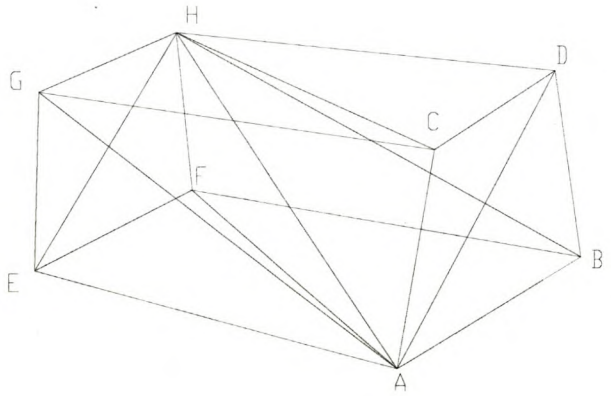

Figure 5.3. Three dimensional control volume

figure 5.4, by joining two opposite corners of the cell. Each tetrahedral volume represents half the volume of a parallelepiped defined by the scalar triple product of three vectors, each of which lie along different facial planes of the parallelepiped.

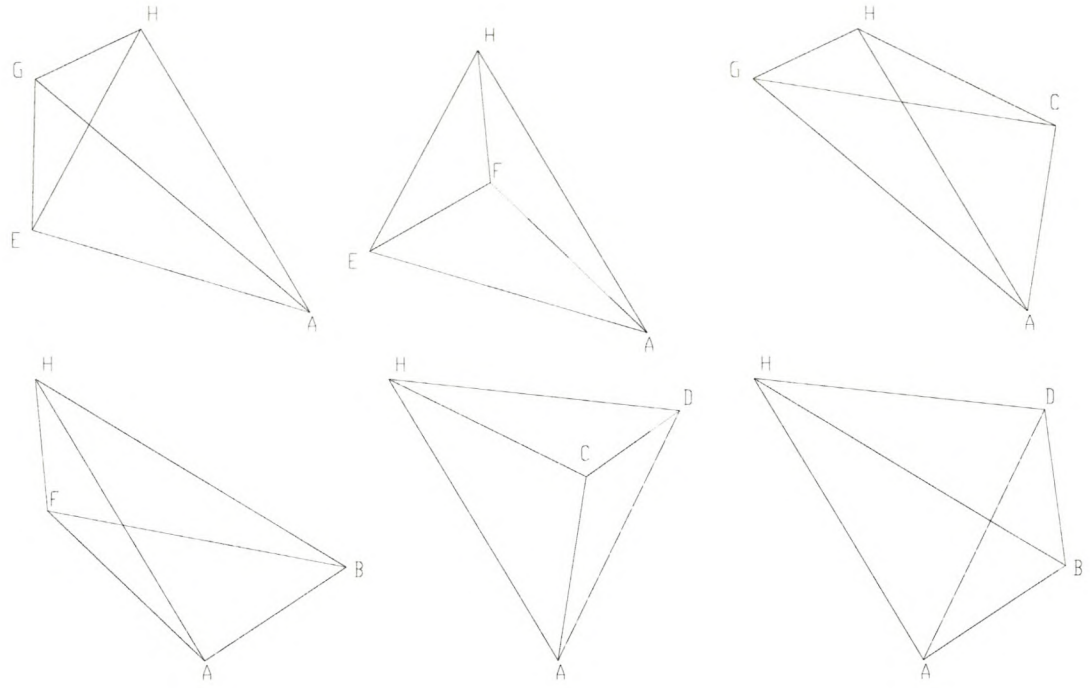

Figure 5.4 Control volume tetrahedra

Thus the volume of the parallelepiped defined by tetrahedral ABDH can be found from the scalar triple product

$$\mathrm{Vol}_{ABDH} = \left|\left(\vec{C}_{AD} \times \vec{C}_{AB}\right) \bullet \vec{C}_{AH}\right| \tag{5.22}$$

and the volume of the hexahedral computational cell can be shown to be

$$\mathrm{Vol}_N = \frac{1}{6}\Big[\left(\left|\vec{C}_{AD} \times \vec{C}_{AB}\right| + \left|\vec{C}_{AC} \times \vec{C}_{AD}\right| + \left|\vec{C}_{AG} \times \vec{C}_{AC}\right| \right.$$

$$\left. + \left|\vec{C}_{AB} \times \vec{C}_{AF}\right| + \left|\vec{C}_{AF} \times \vec{C}_{AE}\right| + \left|\vec{C}_{AE} \times \vec{C}_{AG}\right| \right) \bullet \vec{C}_{AH} \Big] \tag{5. 23}$$

All the vectors required for the calculation are found from the coordinates of their respective vertices.

6. VERIFICATION OF THE CODE

6.1 Introduction

This chapter deals with the verification of the results obtained from the application of the present numerical code. The code is applied to simple problems for which analytical, experimental or other numerical results are available. The verification problems were selected to ensure that that the code accurately models important mechanisms present in the physical flow such as the hydrodynamic and thermal boundary layer development of flows, heat transfer characteristics and turbulence modeling. The results from the test cases are also compared to radial flows within parallel plates under similar flow conditions. This is done to evaluate the performance of the code to predict flow within geometries similar to those found for application to the circular solar collectors discussed in chapter 7. Lastly, the performance of the code to process geometries containing non-orthogonal control volumes is evaluated.

The verification problems are:

- Steady, laminar hydrodynamic and thermal developing flow between parallel plates discussed in section 6.2.
- Steady, turbulent hydrodynamic and thermal developing flow between parallel plates discussed in section 6.3.
- Radial flow within parallel plates discussed in section 6.4.
- Steady, turbulent hydrodynamic developing flow between parallel plates with non-orthogonal control volumes.

All the evaluations reported were carried out using three grid configurations ranging from coarse, medium and fine grid resolution to ensure that grid independent results were achieved. The evaluation result was deemed grid independent and converged once it was found that the difference for the results for the average pressure and temperature field deviated less than 1% from the results from a previous and coarser grid evaluation. All the test cases reported followed this procedure.

6.2 Steady, Laminar Hydrodynamic and Thermal Developing Flow Between Infinite Parallel Plates

6.2.1 The numerical model

The behaviour of laminar fluid flows in ducts and laminar flows between parallel plates has been extensively investigated, both numerically and experimentally. The numerical model verified in this study represents the physical model, the fluid properties and the flow conditions as shown in figure 6.1 for air flow between parallel plates. The plates are W=0.1m wide and H=0.1m apart. The plate length is L=3.0m.

A constant mass flow of uniform inlet velocity (U=0.0183m.s^{-1}) was selected which permits the investigation of the hydrodynamic and thermal flow development within the entrance region. The Reynolds number based on an effective diameter of twice the plate height (2H) is Re=240. The developing flow frictional pressure drop and heat transfer correlation comparisons presented later in this chapter are also based on the effective diameter mentioned above. The outlet velocity is mass-flux corrected. Both top and bottom plates are at constant wall temperature (T_w=373K) and a uniform air inlet temperature profile (T_i=273K) is selected. Axi-symmetric side boundaries (y-direction) ensure that the essentially two-dimensional flow is maintained.

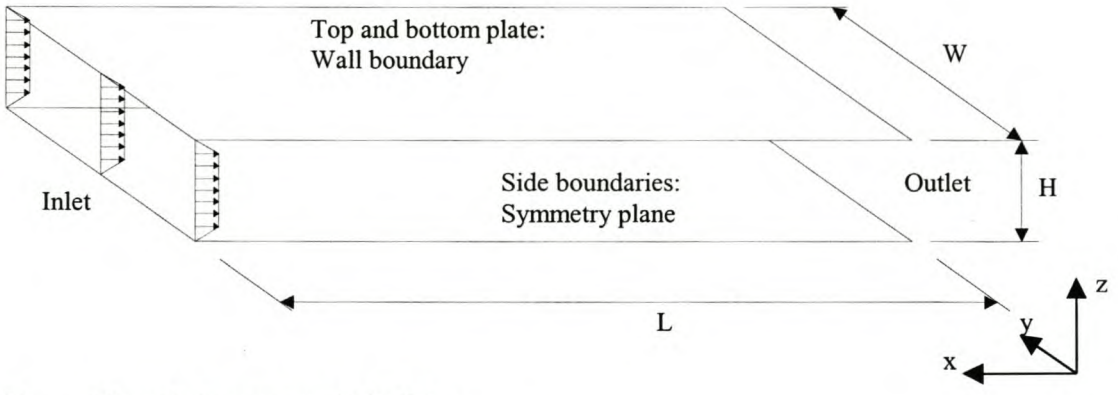

Figure 6.1. Flow between parallel plates

The calculations were performed on three grids (91x3x11, 45x3x17 and 33x3x13 grid points) to ensure grid independent results. The results for the 45x3x17 grid were found to be grid independent and is shown here.

The number of iterations required to reach convergence on this grid is approximately 150 with under-relaxation factors as per Table 6.1. The convergence history is shown in figure 6.2 where the normalised mass residual is defined as the absolute sum of mass residuals of all control volumes divided by the inlet mass flux. Computational speed was 0.0045 seconds/iteration/grid point.

Table 6.1 Solution parameters for laminar flow between parallel plates.

Under-relaxation factors			Flux blending factor
α_p	α_v	α_T	γ
0.1	0.8	0.9	0.9

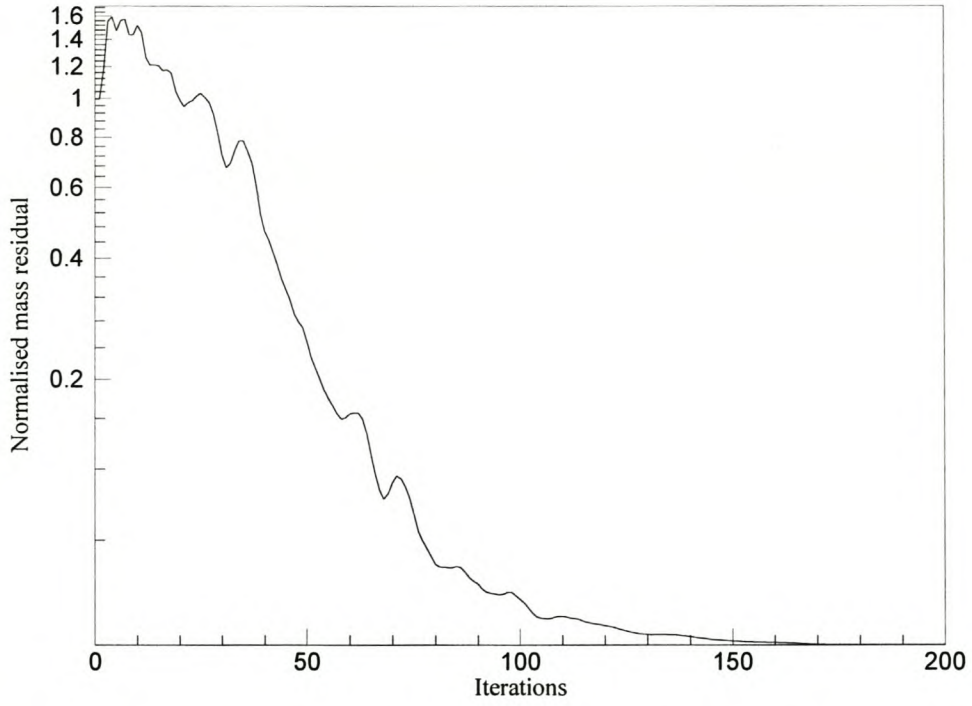

Figure 6.2. Convergence history for laminar flow between parallel plates.

6.2.2 Code results

Figure 6.3 shows the computational domain with the inlet at x=3.0m. The resultant vector field plot is shown in figure 6.4. The velocity contours for the axial and normal velocity components are shown in figure 6.5 and figure 6.6. The presence of w-velocity components at the inlet, shown in figure 6.6, indicates the flow development from a uniform inlet distribution to the parabolic laminar velocity distribution. The pressure contours shown in figure 6.7 illustrates the pressure gradient across the width of the channel in the entrance region. As the flow develops, this cross stream pressure gradient, $\left(\frac{dp}{dz}\right)$, disappears and only the approximately linear axial pressure gradient from frictional effects remains. The temperature contours are shown in figure 6.8. Figure 6.9 shows the dimensionless outlet axial velocity (u/u_i) profile across the width of the channel. The dimensionless outlet velocity is based on the uniform inlet velocity (u_i). Figure 6.10 shows the rise in the average temperature along the channel associated with the thermal development of the flow between two plates of constant temperature. The average cross stream temperature is calculated as shown in appendix C.

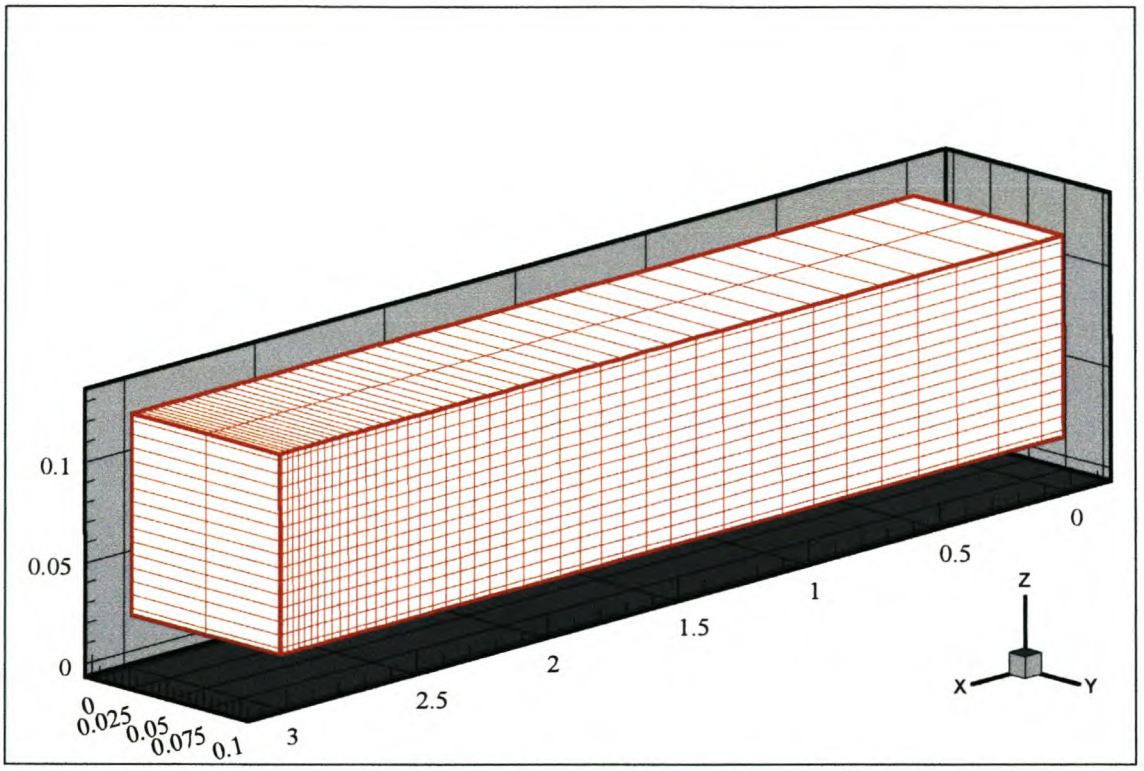

Figure 6.3. Computational domain for 45x3x17 grid points

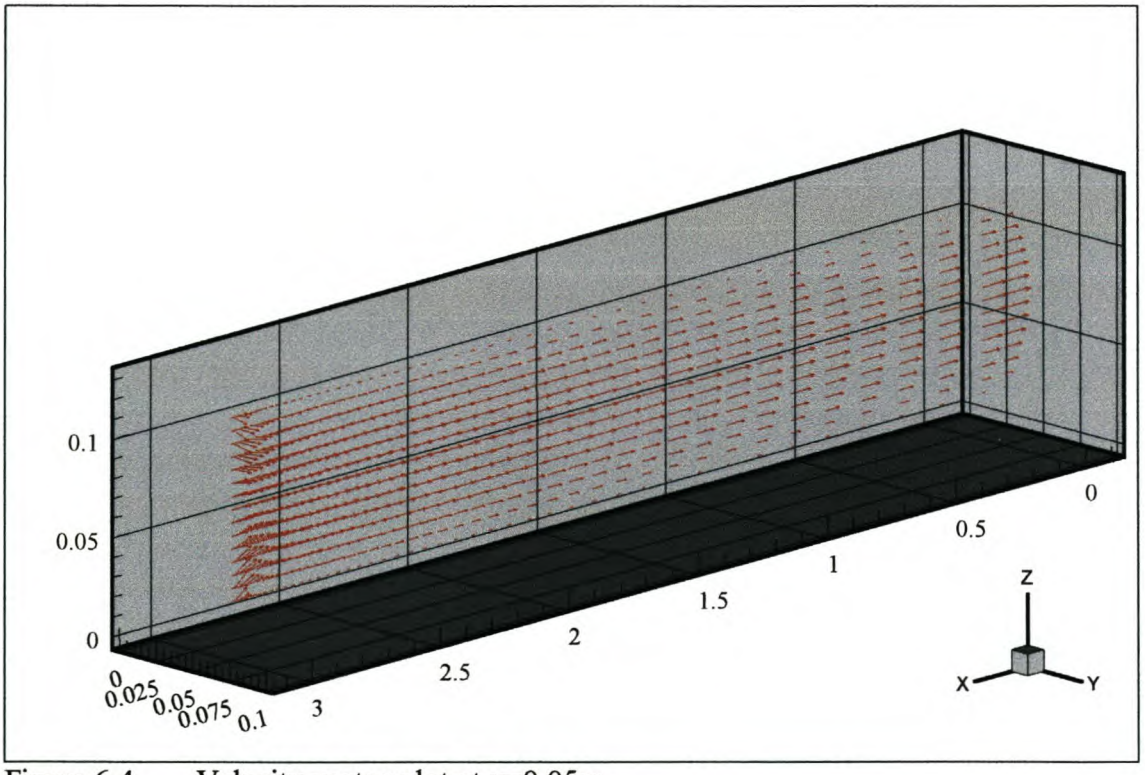

Figure 6.4. Velocity vector plot at y=0.05m

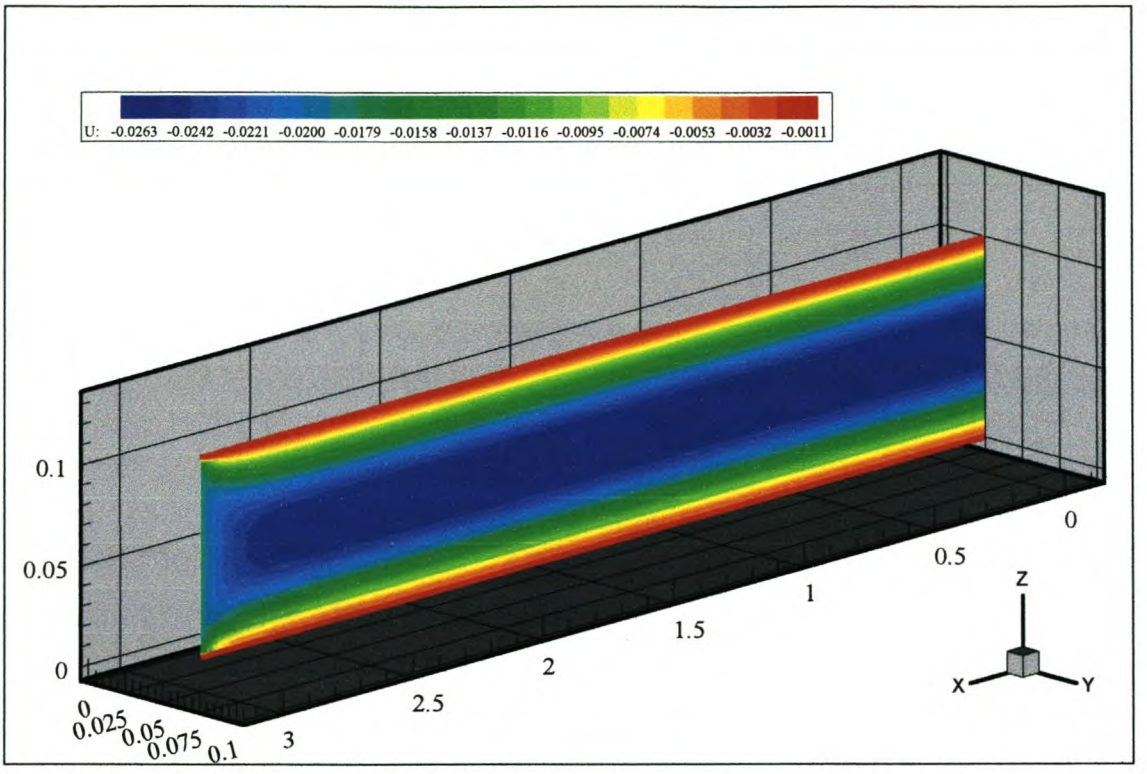

Figure 6.5. U-Velocity contour plot at y=0.05m

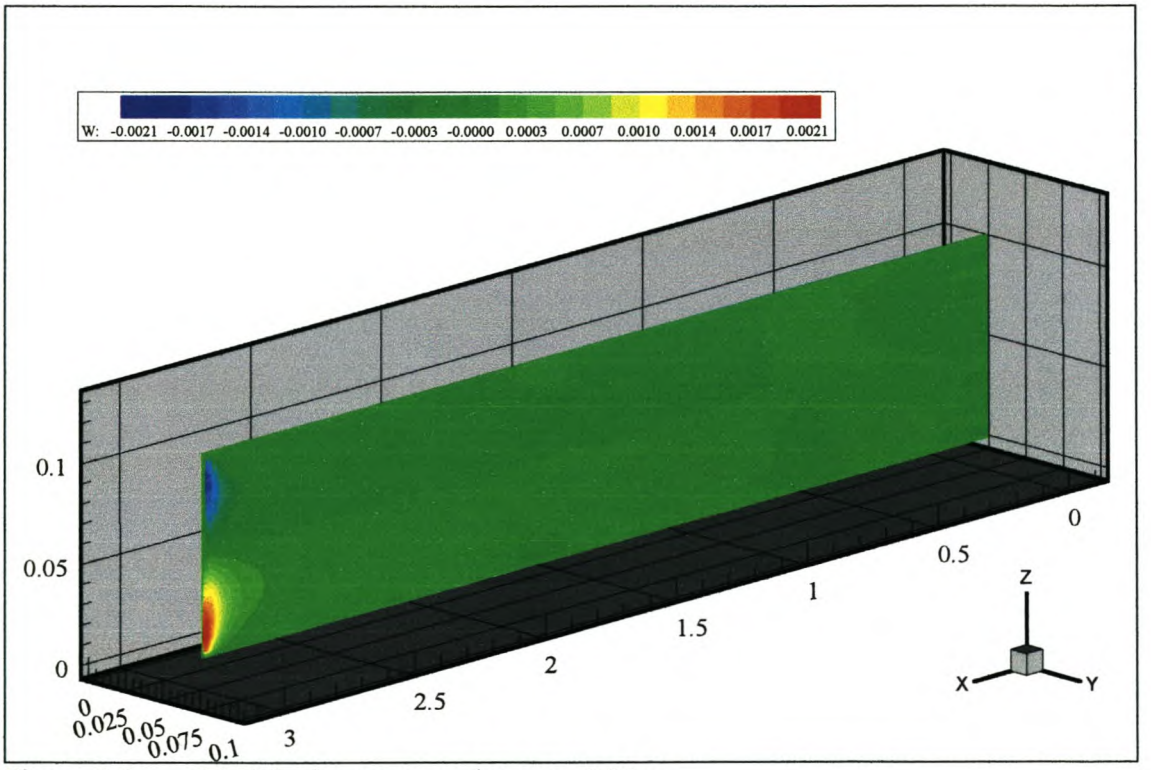

Figure 6.6. W-Velocity contour plot at y=0.05m

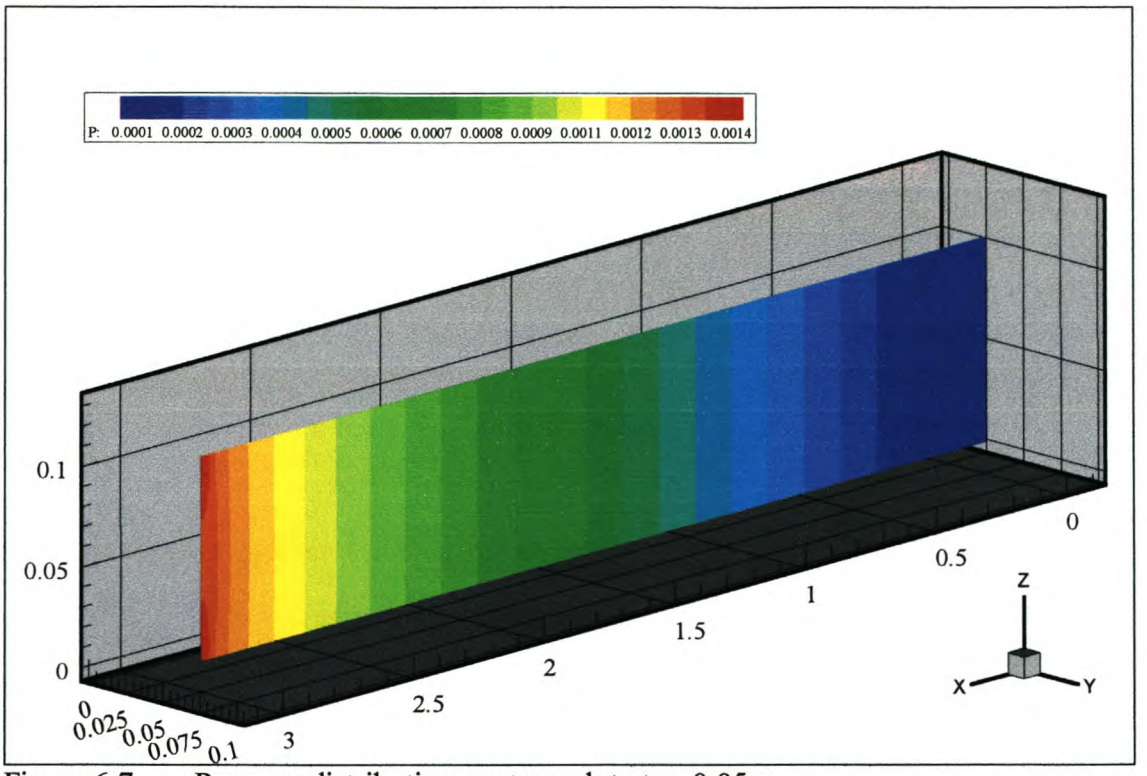

Figure 6.7. Pressure distribution contour plot at y=0.05m

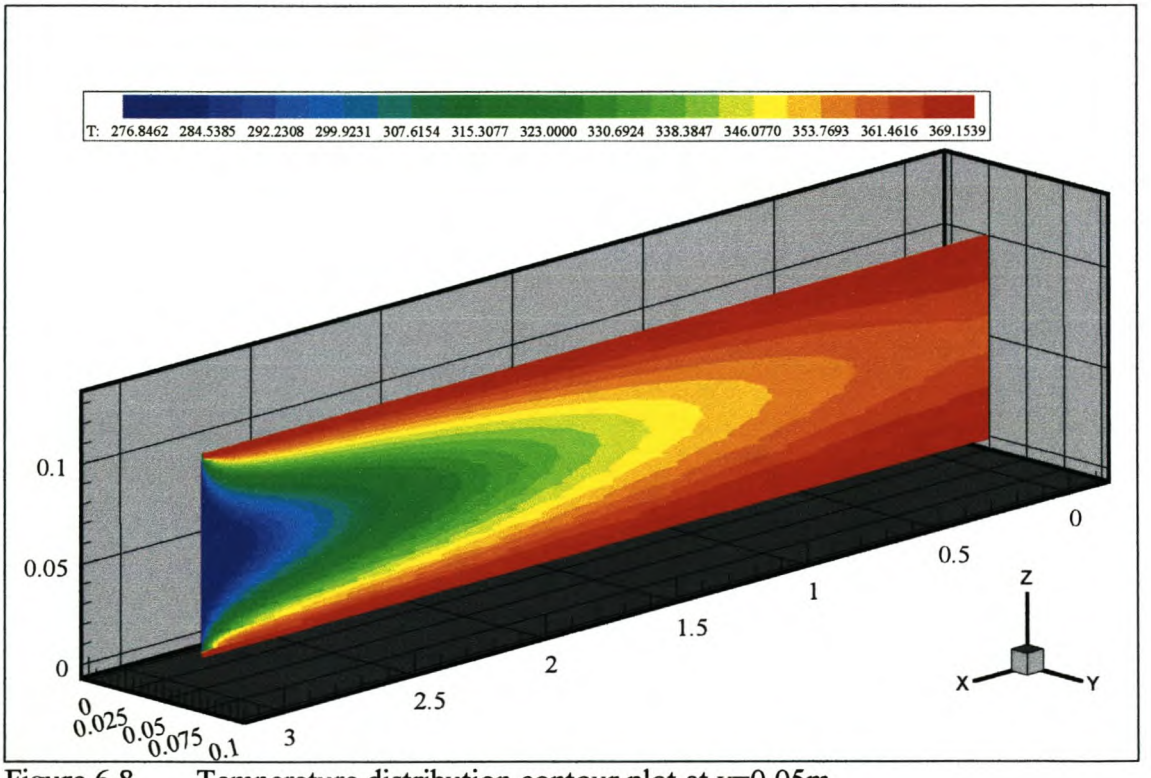

Figure 6.8. Temperature distribution contour plot at y=0.05m

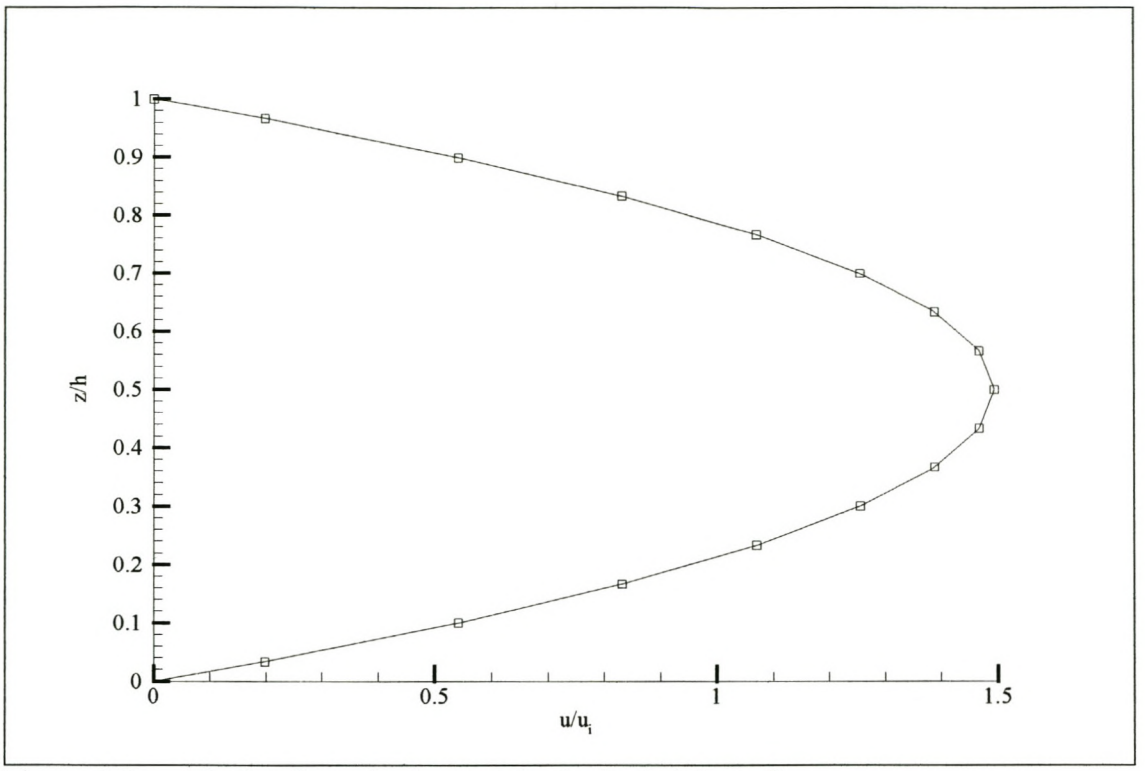

Figure 6.9. Outlet dimensionless axial velocity (u/u_i) profile

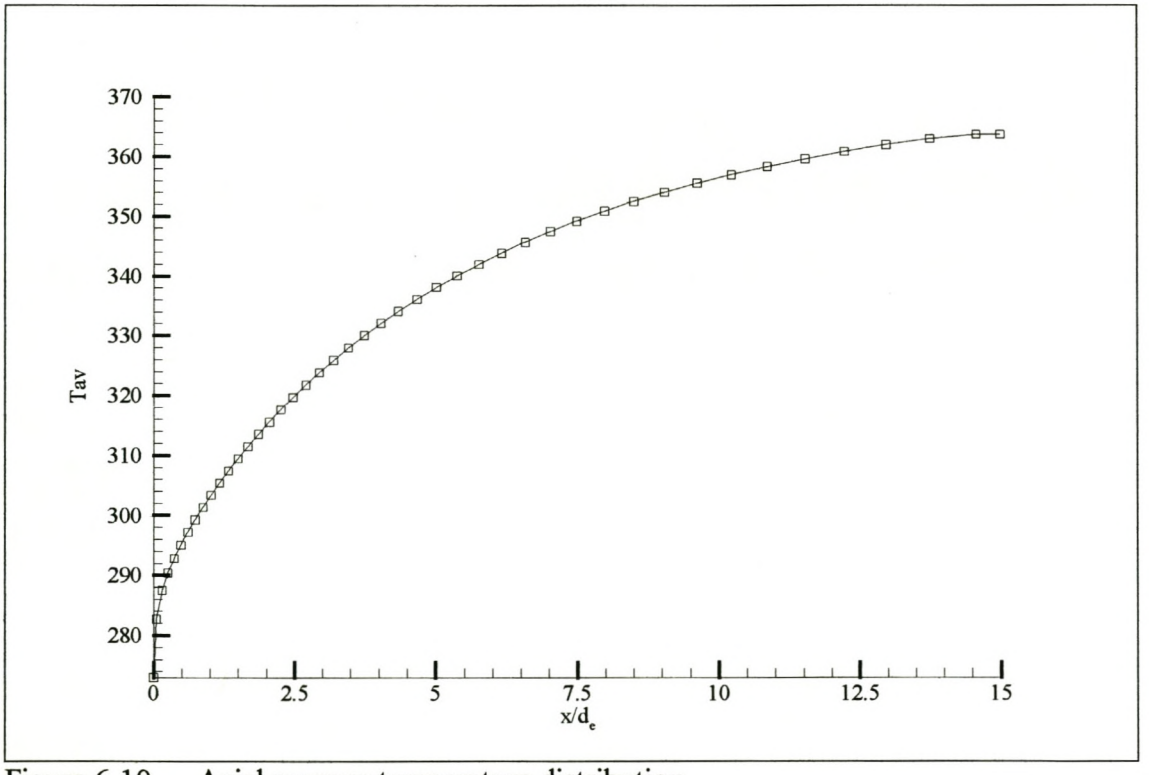

Figure 6.10. Axial average temperature distribution

6.2.3 Verification of results

The friction factors for the code solution can be calculated from the Darcy Weisbach relation as presented by Kröger (1998)

$$f_{app}\,Re = \frac{\Delta p}{4\left(\rho\frac{\bar{u}^2}{2}\right)\left(\frac{L}{d_e}\right)}Re \tag{6. 1}$$

where

$$d_e = 2H \tag{6. 2}$$

$$\Delta p = \bar{p}_{inlet} - \bar{p}_x \tag{6. 3}$$

$$f_{app} = \frac{f_D}{4} \tag{6. 4}$$

with f_D denoting the Darcy friction factor.

Equation (6.1) requires the average values of pressure and velocity in determining the friction factor and Reynolds number. This is found by integrating the pressure and velocity profile found from the field solution. These relations for determining the average values from flow field solutions can be found in appendix C.

The apparent friction factor in equation (6.1) includes the effects of an increased pressure drop in the entrance region due to the increased in shear stress in the boundary layer from the acceleration of the core fluid. The result as presented in figure 6.11, shows very good agreement with the general correlation for laminar flow in ducts of various cross sections of Du Plessis (1992) as presented by Kröger (1998) namely

$$f_{app}\,Re = \left[(f\,Re)^n + \left\{ \frac{3.44}{\left(L/(de\,Re)\right)^{0.5}} \right\}^n \right]^{\frac{1}{n}} \qquad (6.5)$$

where $n = 2.38$ and $f\,Re = 24.00$ for parallel plates. The $(f\,Re)$ term in equation (6.5) is the friction factor contribution for fully developed flow.

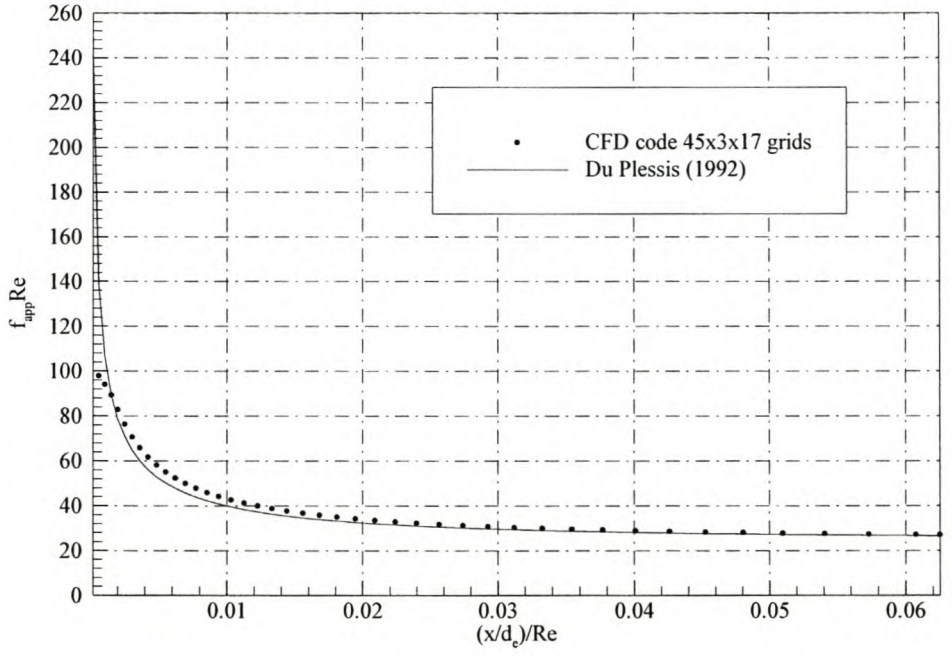

Figure 6.11. Friction factor for laminar flow between parallel plates, Re=240

An interesting observation can be made regarding the difference in friction factor values from the code solution and equation (6.5) in the entrance region. The correlation of equation (6.5) tends towards infinity near the entrance of the duct while the code results tend to some finite value. The three-dimensional solution of the continuity and momentum conservation equations in the entrance region captures a small increase in pressure near the wall at the entrance ($\frac{x}{d_e} \to 0$). At the entrance, the pressure in the center of the duct drops linearly from $x = 0$, whereas the pressure at the wall first shows a small increase in pressure before dropping. This initial increase in pressure at the wall entrance region, forces a flow of mass towards the center of the duct with a subsequent increase in duct centerline velocity consistent

with the conservation of mass. Thus instead of having an infinitely small pressure drop near the entrance, the small increase in pressure at the wall increases the average pressure slightly, resulting in the lower finite values of friction factors as shown in figure 6.11. This does not influence the fully developed friction factor values.

The theoretical hydrodynamic developing length may be calculated from the relation of Shah and London (1978) as presented by White (1991) and rewritten in terms of a dimensionless distance from the entrance i.e.

$$\frac{x}{d_e\,Re} \approx \left(\frac{0.6}{1+0.035\,Re}\right)\left(\frac{1}{Re}\right) + 0.056 \qquad (6.6)$$

The dimensionless distance from the entrance for fully developed flow for Re=240 according to equation (6.6) is $x/(d_eRe)=0.0563$. This theoretical value corresponds well to the code prediction, as seen from the asymptotic behaviour of the curves in figure 6.11 at approximately $x/(d_eRe)=0.06$.

The local dimensionless heat flux parameter or Nusselt number is found from the relation

$$Nu = \frac{mC_p(T_o - T_i)d_e}{k_f A(T_w - T_f)} \qquad (6.7)$$

which is derived by applying an energy balance across the channel. This local Nusselt number is based on an effective diameter of twice the plate spacing with T_i and T_o denoting the inlet and outlet fluid temperatures respectively, T_w being a constant wall temperature, T_f denoting the mean bulk fluid temperature, m denoting the mass flow rate of the fluid, k_f and C_p denoting the fluid thermal conductivity and specific heat at ambient temperature and A representing the total plate area for the duct. Thus from the temperature field values obtained from the code results one can compute the local Nusselt number from equation (6.7). Again the temperature values required in equation (6.7) are found from the integration of the

temperature profile as computed by the code. The mean Nusselt number is simply the average value of the local Nusselt number along the plates between x=0.0 and x=L i.e.

$$Nu_m = \frac{1}{L}\int_0^L Nu\ dx \tag{6. 8}$$

which may by found by simply substituting the temperature difference (T_w-T_i) in equation (6.7) with the logarithmic temperature difference White (1991) i.e.

$$\left(T_w - T_f\right) = \Delta T_{ln} = \frac{\left[T_w - T_f(0)\right] - \left[T_w - T_f(x)\right]}{\ln\left\{\left[T_w - T_f(0)\right] / \left[T_w - T_f(x)\right]\right\}} \tag{6. 9}$$

The values calculated from equations (6.7) and (6.9) are compared with the mean Nusselt number values calculated from a correlation by Stephan (1959) as given by Kröger (1998) i.e.

$$Nu_m = 7.55 + \frac{0.024\left(Re\,Pr\,d_e / L\right)^{1.14}}{1 + 0.0358\left(Re\,Pr\,d_e / L\right)^{0.64} Pr^{0.17}} \tag{6. 10}$$

for simultaneously developing flow between parallel plates with uniform inlet velocity and constant wall temperatures. Figure 6.12 shows the comparison between the mean Nusselt numbers found from the code solution and those calculated using equation (6.10).

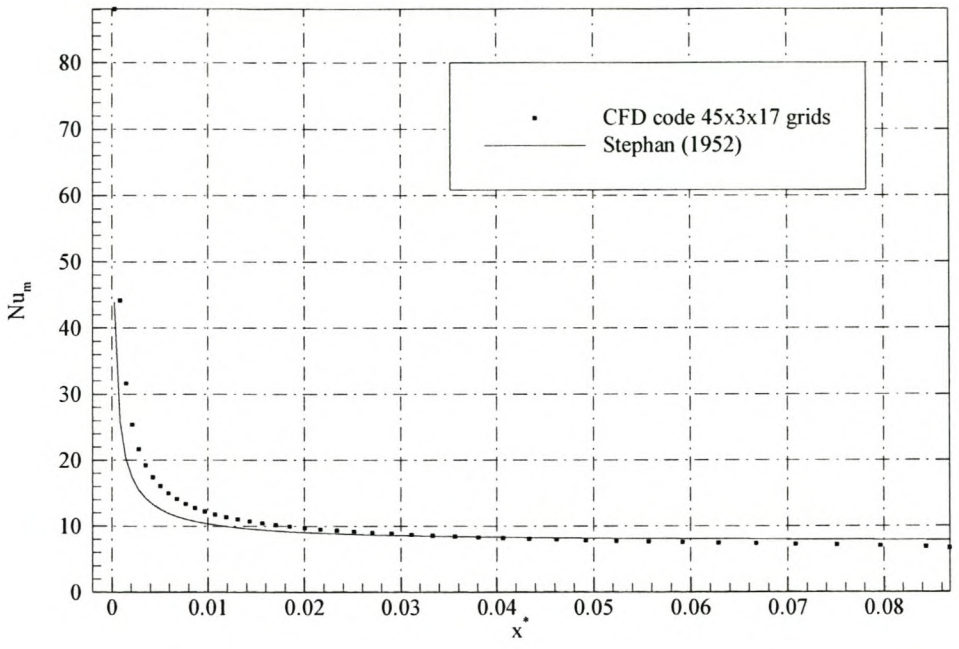

Figure 6.12. Mean Nusselt number for laminar flow between parallel plates, Re=240

The dimensionless distance from the entrance is defined as

$$x^* = \left(\frac{x}{d_e \, Re \, Pr} \right) \tag{6. 11}$$

The prediction from equation (6.10) indicates that the flow is thermally developed at $x^* \approx 0.03$. This is smaller than the value predicted, $x^* \approx 0.05$, by the code results. The latter prediction from the code results compares better with the thermal entry length for pipes from White (1991) i.e.

$$\left(\frac{L_{e,thermal}}{d_e \, Re \, Pr} \right) = 0.05 \tag{6. 12}$$

The results, as shown by figure 6.11 and 6.12, indicates that the code accurately predicts the friction factors and heat transfer coefficients for laminar simultaneously developing flow between the parallel plates.

6.3 Steady, Turbulent Hydrodynamic and Thermal Developing Flow between Parallel Plates

6.3.1 The Numerical model

The turbulence modeling capabilities of the code is verified by applying the present code to the modeling of hydrodynamic and thermally developing turbulent flow between parallel plates. The properties of the flow within such a configuration has been extensively evaluated experimentally and accurately predicted by analytical and numerical methods, Rhosenow et. al. (1985), Schlichting (1968), Stephenson (1975), Comini and Del Guidice (1985).

Turbulent flow between parallel plates shows relatively short developing lengths [$x/(d_eRe)$], both thermally and hydro-dynamically, in comparison with laminar flow. This is due to an increased turbulent momentum transfer from the wall boundaries. This increased mixing effect also leads to an increase in heat transfer from the boundaries as well as an increase in shear stress, subsequently leading to higher friction factors or a larger pressure gradient.

The numerical model employs the standard $k-\varepsilon$ model as described in chapter 2 in determining the turbulent kinetic energy and rate of diffusion. The model was solved with three-dimensional orthogonal control volumes. The test case configuration, boundary conditions and fluid properties are similar to the laminar flow case and as illustrated by figure 6.1. The total length of the parallel plates was changed to L=10.0m to accommodate fully developed flow conditions for large Reynolds numbers.

Initially an entrance region control volume refinement was applied in order to evaluate the developing region properly. The difference in results for the refined grid and uniform grid proved insignificant and a uniform grid was selected for the verification. Three uniform grid configurations were evaluated namely 35x3x7 grid points, 65x3x17 grid points and 99x3x15 grid points. This ensured that a grid independent solution was reached and the results shown are applicable to the intermediate grid, 65x3x17, since it was found to give grid independent results. It was found that 8000 iterations were required for the solution as indicated by the convergence history shown in figure 6.13. The normalised mass residual is defined as the

absolute sum of mass residuals of all control volumes divided by the inlet mass flux. The under-relaxation factors employed are shown in table 6.2. Computational speed was 0.0042 seconds/iteration/grid point.

Table 6.2 Solution parameters for turbulent flow between parallel plates

Under-relaxation factors					Flux-blending
α_p	α_V	α_k	α_ε	α_T	γ
0.2	0.8	0.2	0.2	0.9	0.9

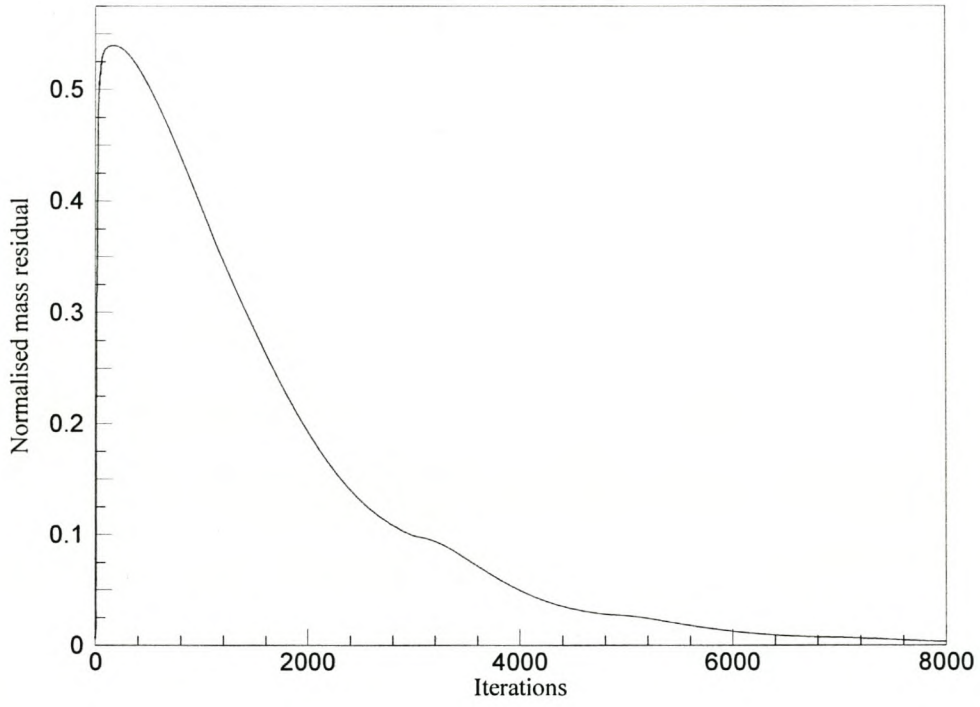

Figure 6.13. Convergence history

6.3.2 Code results

The code results shown are applicable to Re=196721. Figure 6.14 shows the computational domain and the resultant vector field plot is shown in figure 6.15. The pressure contours are shown in figure 6.16. The cross stream pressure gradient in the entrance region is not visible

due to the presence of a much larger axial pressure gradient due to frictional effects. The temperature contours are shown in figure 6.17. The velocity contours for the axial and normal velocity components are shown in figure 6.18 and 6.19. Again figure 6.19 shows the w-velocity contours in the entrance region where the flow develops from a uniform inlet distribution to the fully developed turbulent velocity distribution.

The turbulent kinetic energy and dissipation rate contours are shown in figures 6.20 and 6.21. The large velocity gradient near the wall at the entrance increases the turbulent kinetic energy and dissipation rates in that region as shown by figures 6.20 and 6.21. The effective viscosity contour plot is shown in figure 6.22 indicating the increase of the stream turbulence and effective viscosity towards the outlet.

The code prediction of the dimensionless outlet turbulent kinetic energy profile is compared to previous experimental and numerical results in figure 6.23. The dimensionless kinetic energy is defined as

$$k^+ = \frac{2k}{u_\tau^2} \qquad (6.13)$$

where the shear velocity, u_τ, at the wall is found from equations (2.42), (2.44) and (2.46) with the turbulent viscosity taken at the first node away from the wall. The z-dimension in figure 6.23 is measured from the centerline. The code prediction compares well with experimental results from Comte-Bellot (1965) although it shows an over-prediction in the center of the flow. The numerical prediction of Comini and Del Guidice (1985) shows an under-prediction of the dimensionless kinetic energy. This may be attributed to insufficient allowance for the developing length for the turbulent kinetic energy. The Comini and Del Guidice (1985) numerical model dimensionless duct length was, l/d_e=5.0 whereas the present model yields a more acceptable value of l/d_e=50.0, typically associated with development of turbulent flows. Although the numerical work of Comini and Del Guidice (1985) applied a developed velocity profile for the inlet boundary condition, it employed a uniform inlet kinetic energy and dissipation rate profile. A similar under-prediction of center line values was also reported by Harms (1995) for fully developed turbulent flow. The numerical

prediction by Stephenson (1976) shows an under-prediction largely due to a lower Reynolds number employed. The turbulent kinetic energy prediction from the present code was found acceptable due to its accurate prediction of the developing flow friction factors and heat transfer coefficients, discussed below.

The dimensionless dissipation rate outlet profile is shown in figure 6.24. The dimensionless dissipation rate is defined as

$$\varepsilon^{+} = \frac{\varepsilon d_e}{u_\tau^3} \tag{6. 14}$$

The prediction from the code again shows larger values compared to the values from the numerical predictions of Comini and Del Guidice (1985).

The normalised outlet axial velocity profile is shown in figure 6.25 indicating the flattened velocity profile associated with turbulent flows. This profile is compared to the universal velocity profile of Prandtl as presented by Schlichting (1968) i.e.

$$\frac{u_o}{u_c} = \left(\frac{y}{R}\right)^{\frac{1}{n}} \tag{6. 15}$$

where u_c is the outlet centreline velocity and R equals half the plate spacing. The distance y=R-z, where z is measured from the centreline towards the plate wall. An exponent of n=7 is employed which corresponds to a Reynolds number of 1.1E-5, Schlichting (1968). The velocity profile is also compared to the velocity profile calculated from the logarithmic law for turbulent flows as given by White (1994) i.e.

$$\frac{u_o(y)}{u^*} = \frac{1}{\kappa}\ln\left(\frac{yu^*}{\nu}\right) + B \tag{6. 16}$$

where, similar to equation (2.42), u^* is the wall shear velocity, κ=0.41 is the Von Karman constant, B=5.0 is an empirical constant and y=H/2-z where z is measured from the centreline towards the plate wall. Both the Nikuradse velocity profile and the logarithmic law velocity profile corresponds well to the outlet velocity profile predicted by the code although the logarithmic velocity profile gives slightly better results.

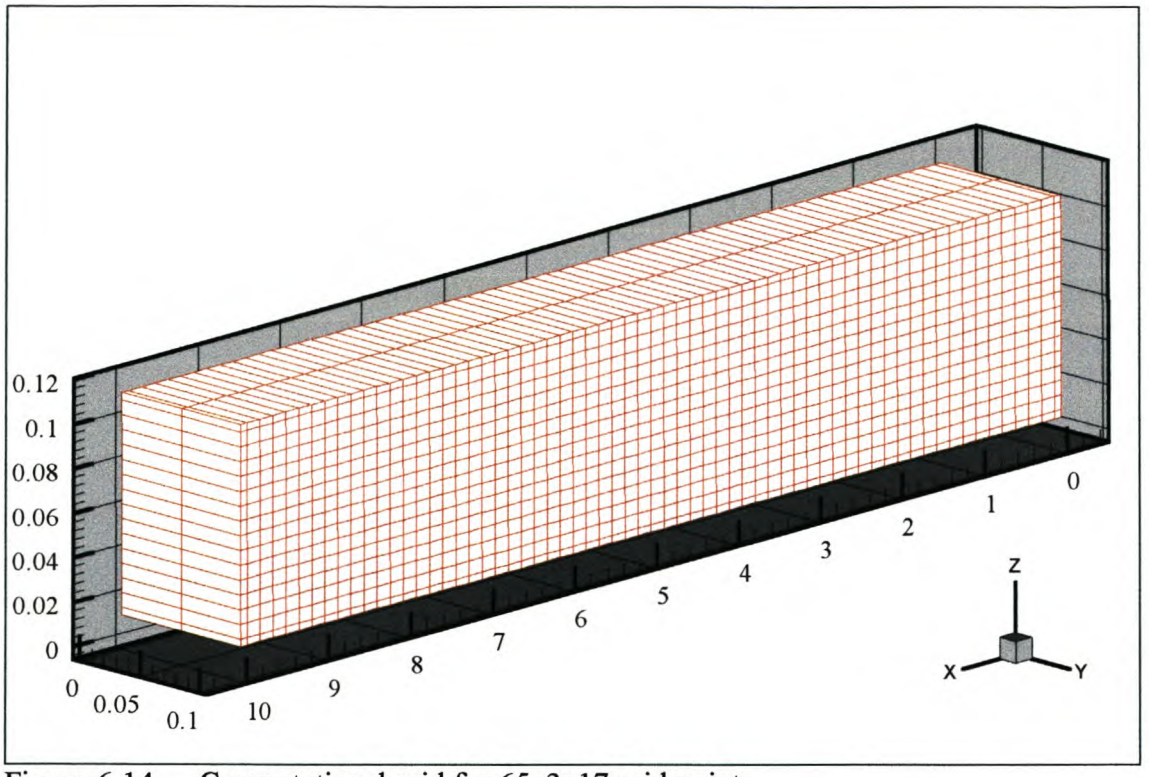

Figure 6.14. Computational grid for 65x3x17 grid points

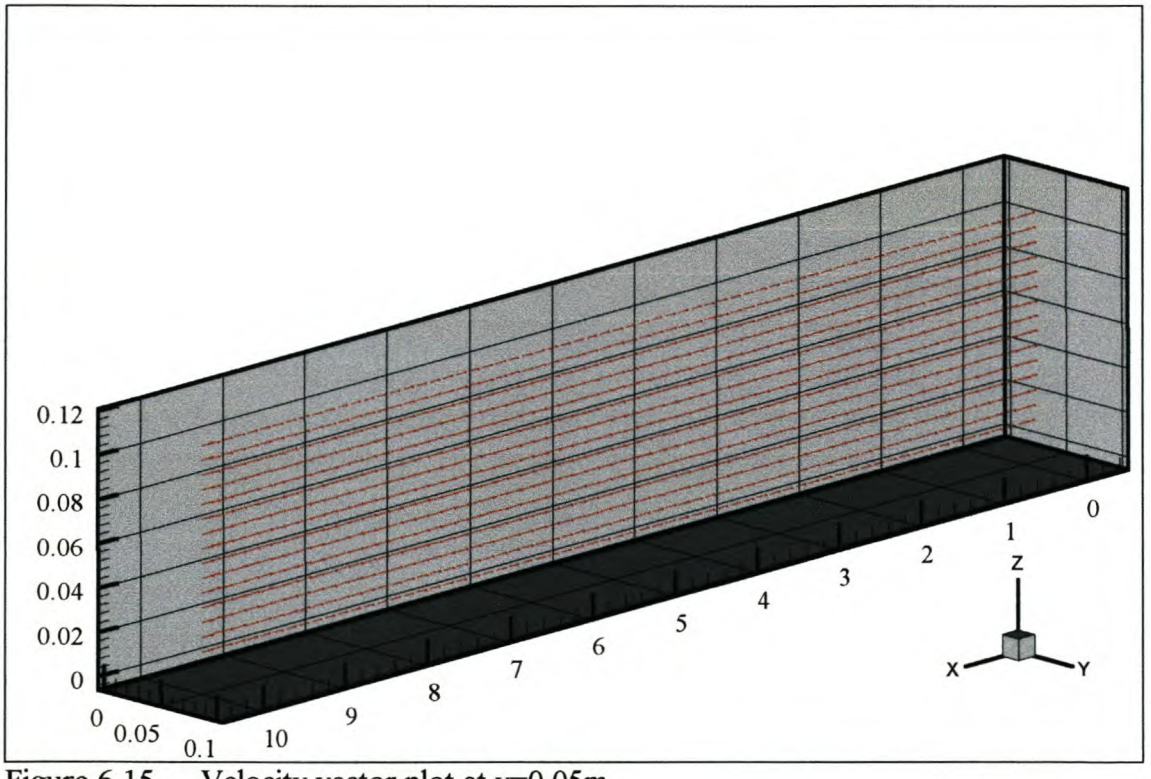

Figure 6.15. Velocity vector plot at y=0.05m

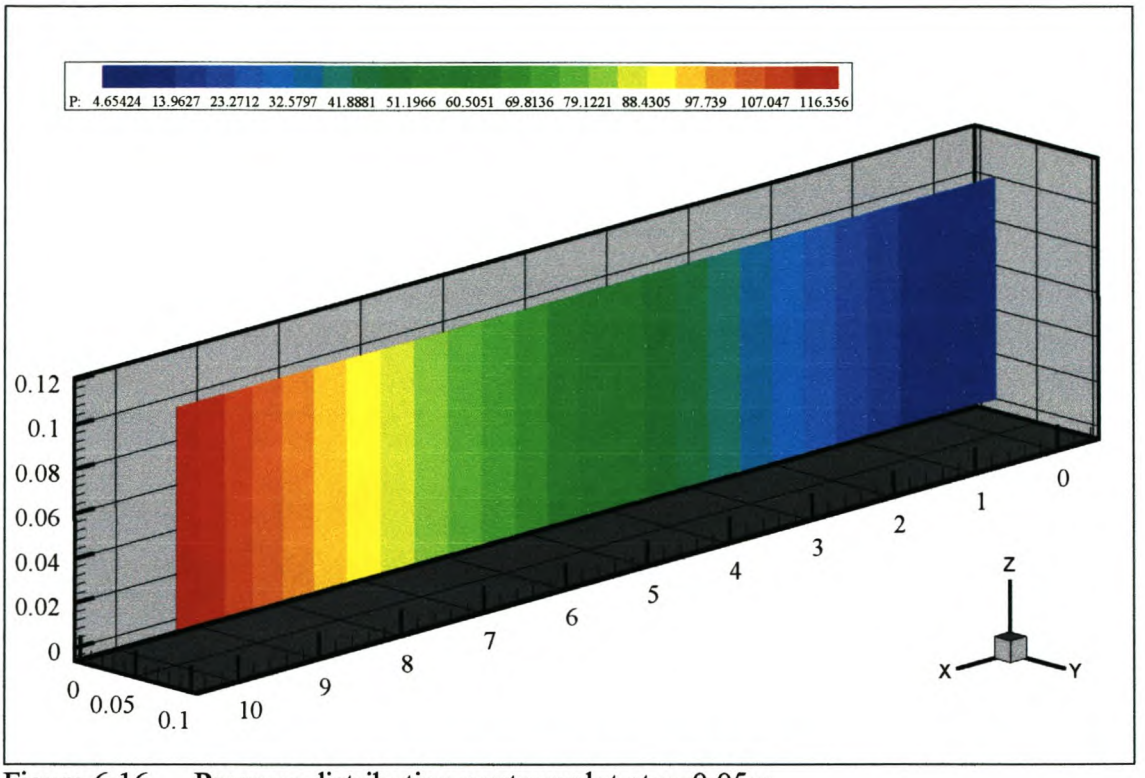

Figure 6.16. Pressure distribution contour plot at y=0.05m

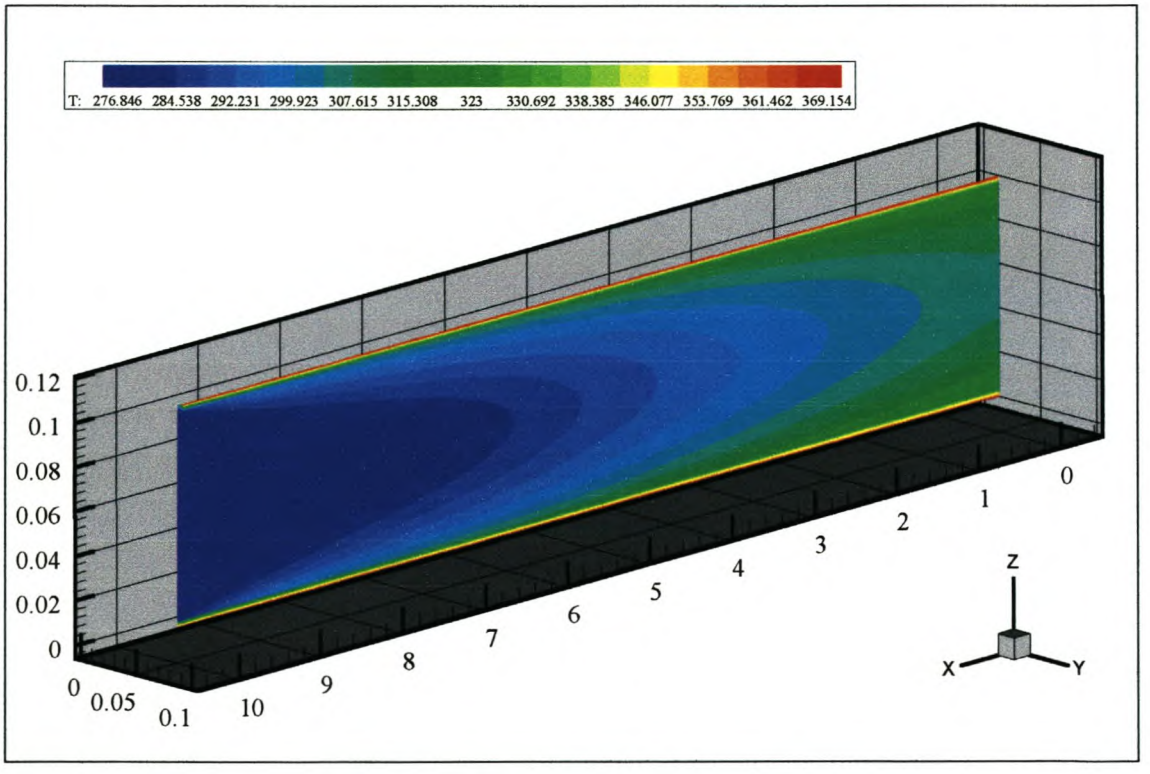

Figure 6.17. Temperature distribution contour plot

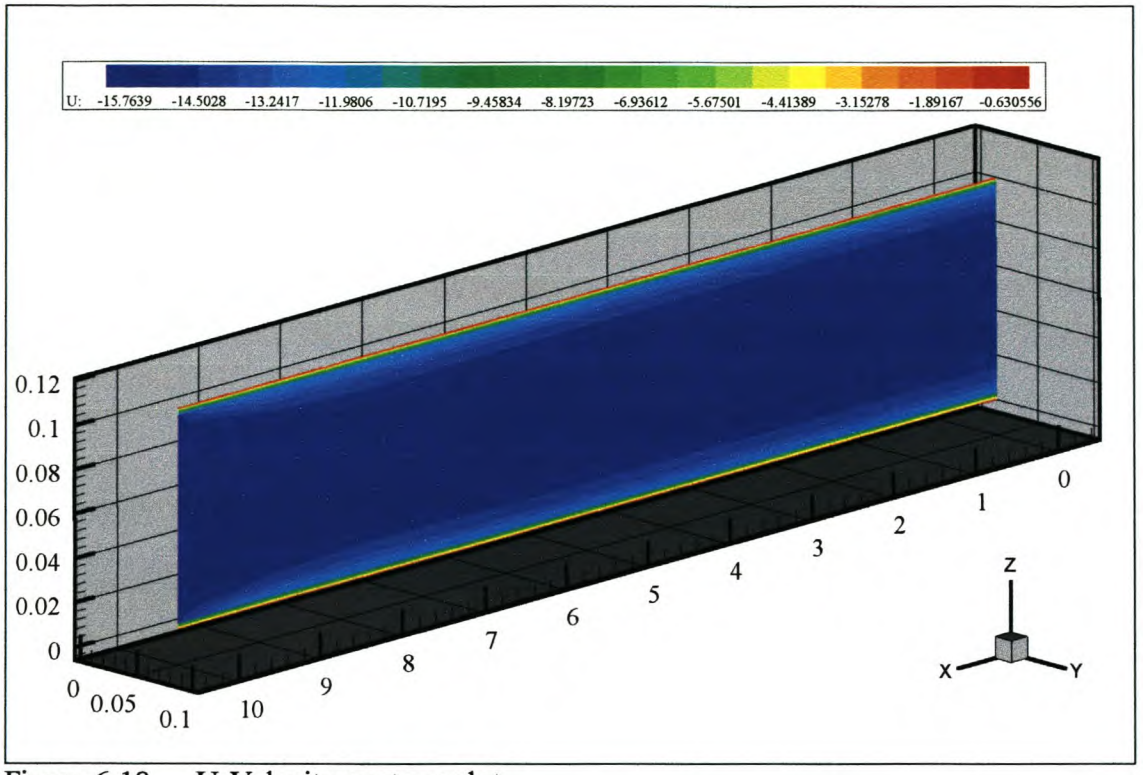

Figure 6.18. U-Velocity contour plot

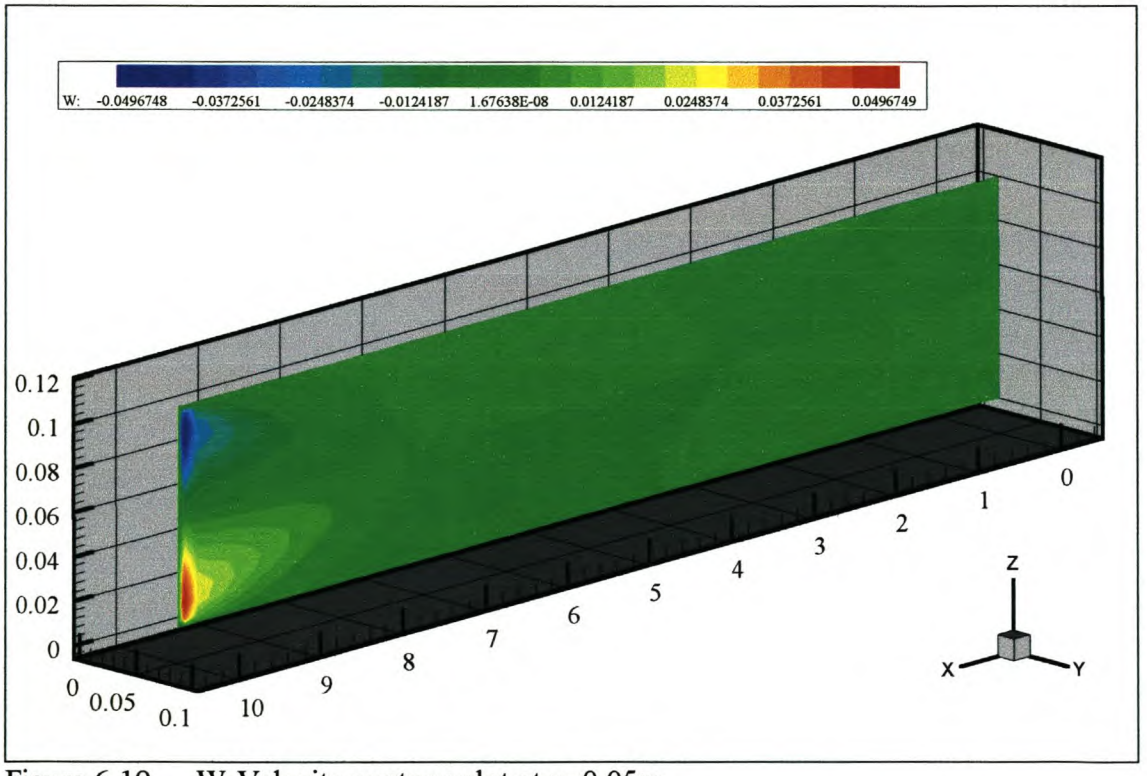

Figure 6.19. W-Velocity contour plot at y=0.05m

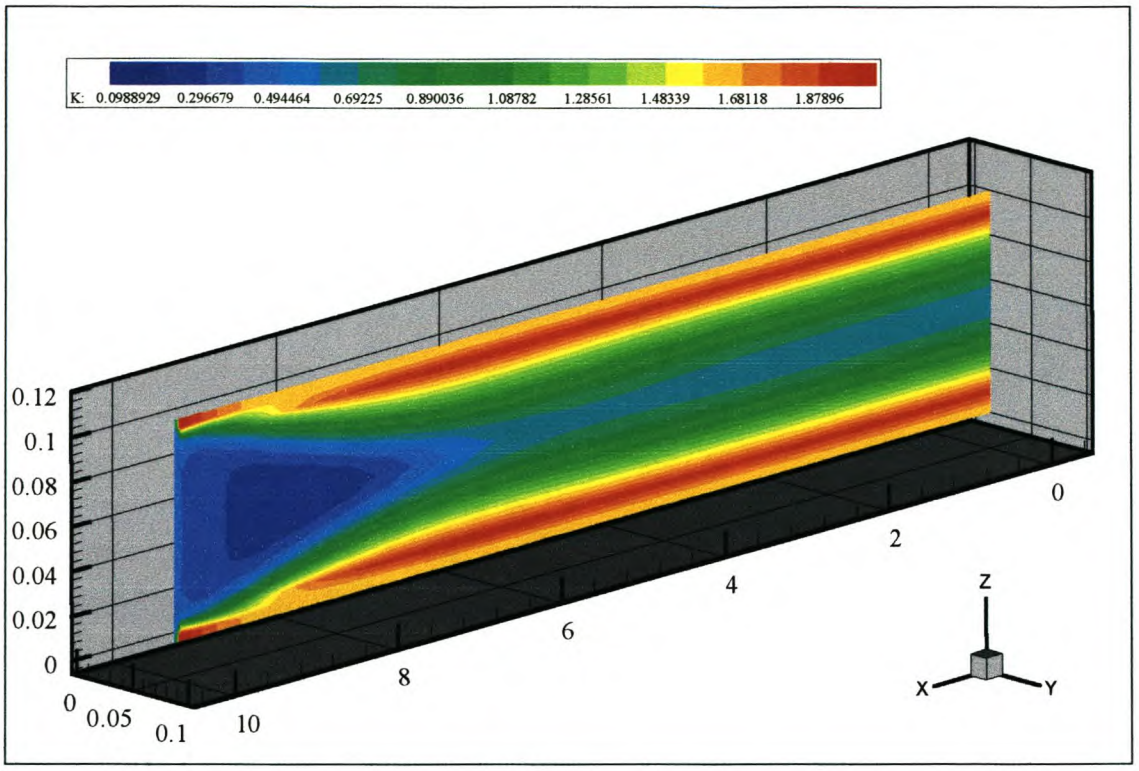

Figure 6.20. Turbulent kinetic energy contours plot at y=0.05m

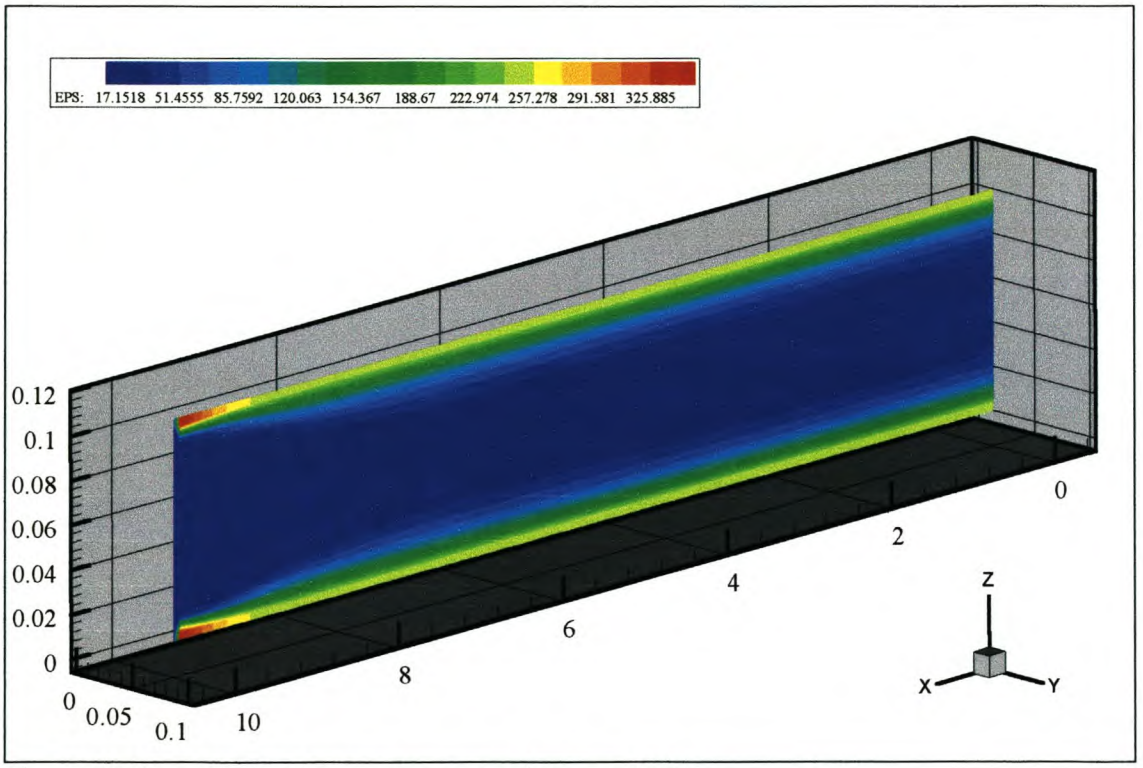

Figure 6.21. Dissipation rate contour plot at y=0.05m

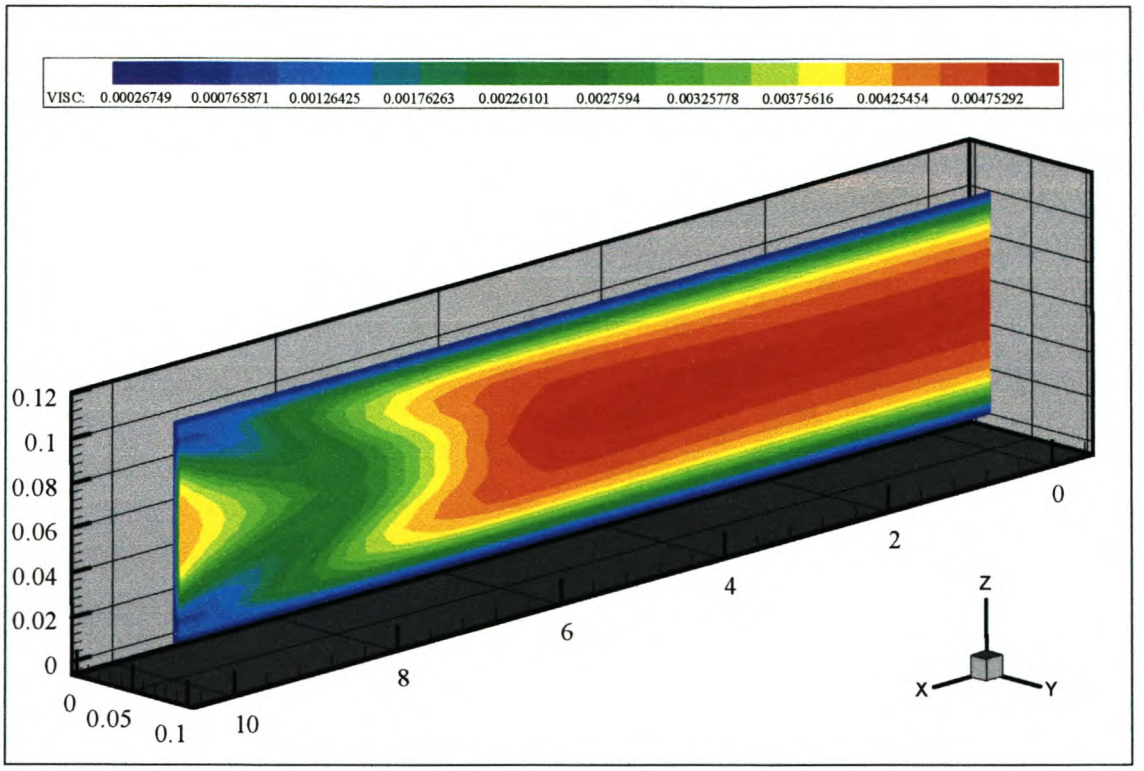

Figure 6.22. Effective viscosity contour plot at y=0.05m

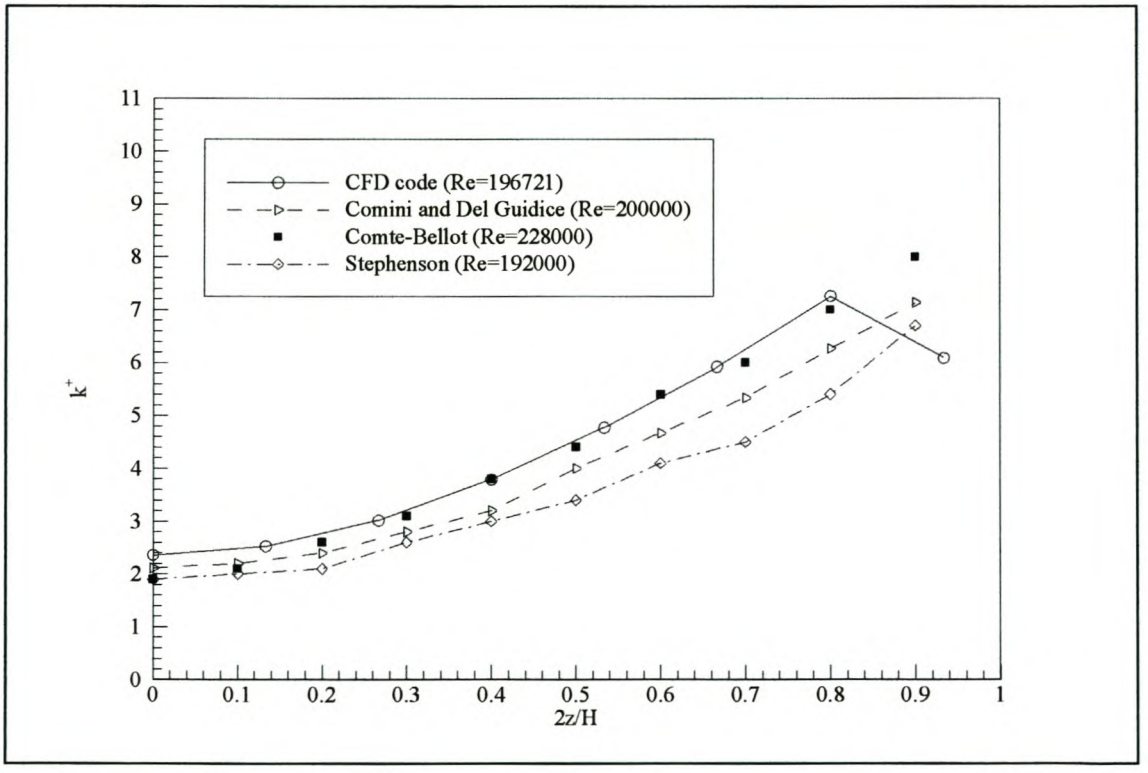

Figure 6.23. Dimensionless outlet turbulent kinetic energy distribution

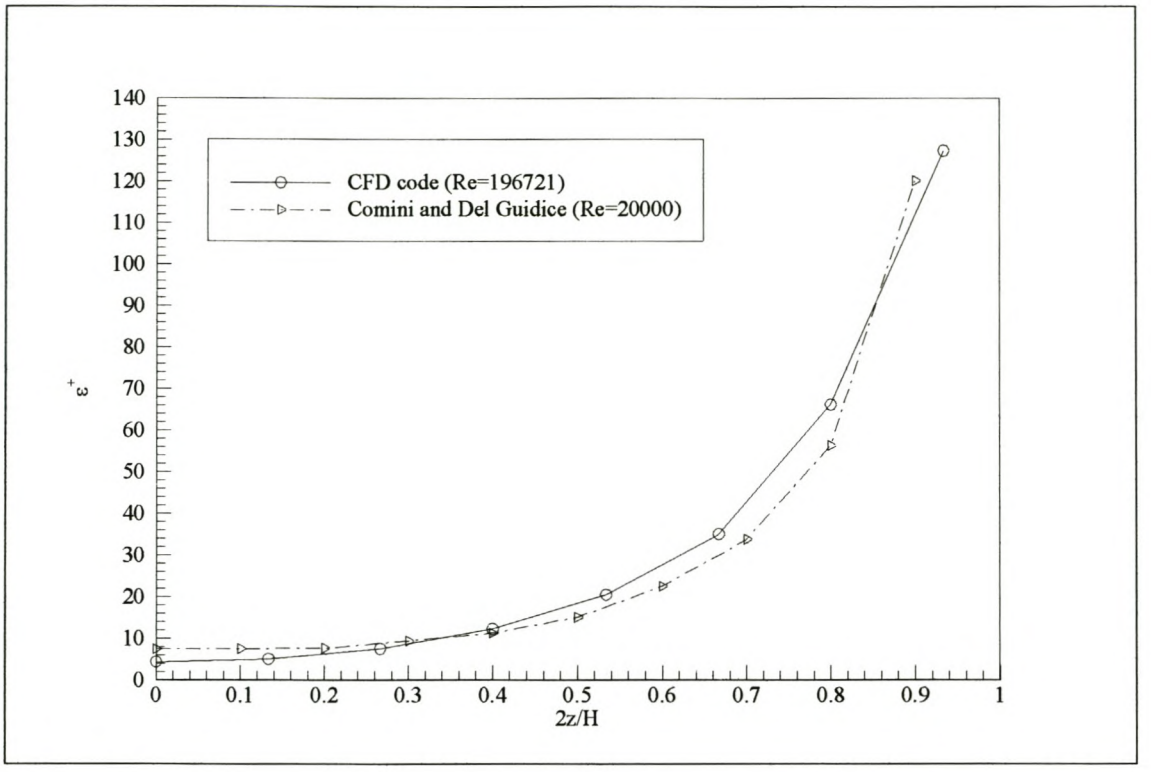

Figure 6.24. Dimensionless outlet dissipation rate distribution

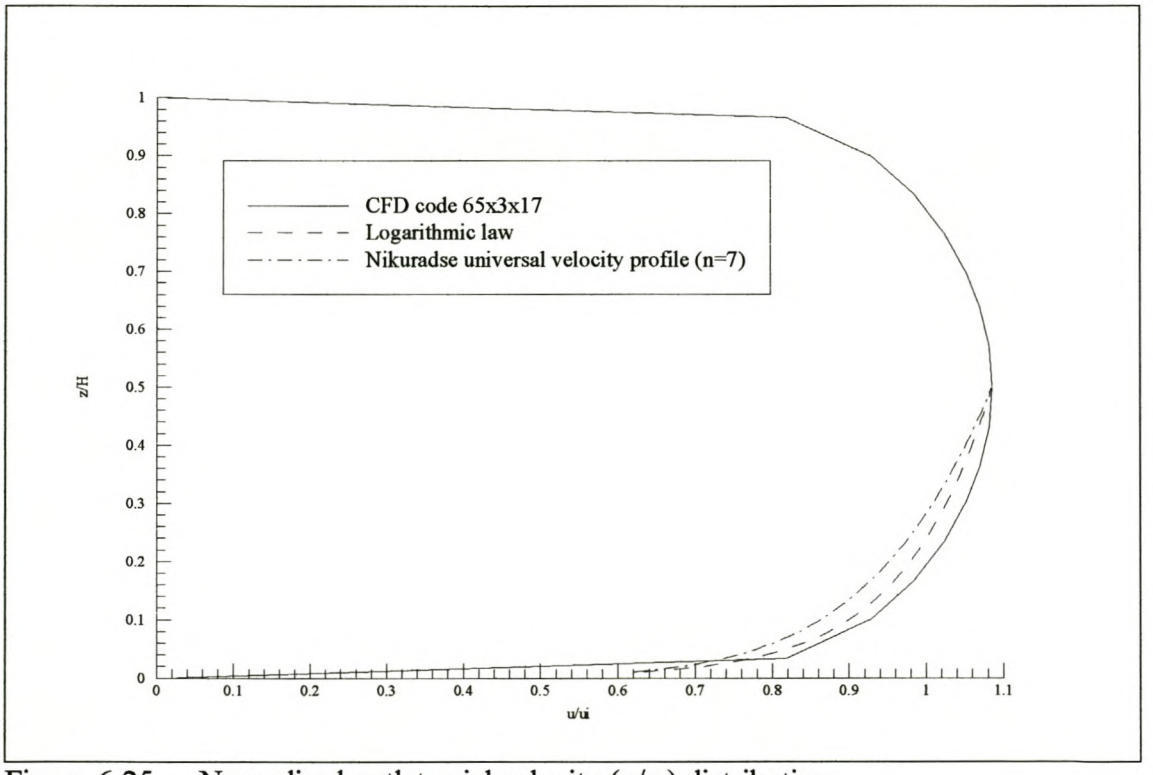

Figure 6.25. Normalised outlet axial velocity (u/u_i) distribution

6.3.3 Verification of results

The flow was evaluated at four Reynolds numbers namely, Re=131147, Re=196721, Re= 262295 and Re=655737. The friction factors from the code solution is again calculated as per equation (6.1). Figure 6.26 shows the friction factor distribution along the length of the plates for the above mentioned Reynolds numbers. Figure 6.26 also shows the fully developed friction factors for parallel plate flows found from equation (6.17) from White (1991) i.e.

$$\frac{1}{f_D^{0.5}} = 2.0\log_{10}\left(Re\, f_D^{0.5}\right) - 1.19 \qquad (6.17)$$

which are plotted at their respective fully developed hydrodynamic entrance lengths calculated from the relation given by White (1994) i.e.

$$\left(\frac{x}{d_e\, Re}\right) \approx 4.4\, Re^{-5/6} \qquad (6.18)$$

The apparent friction factors shown in figure 6.26 are found from equation (6.4). Figure 6.26 indicates that the present code predicts the hydrodynamic developing length in the parallel plates satisfactorily. The results from the present code and using equation (6.4) predicts slightly higher friction factor values than those obtained from the equation for turbulent pipe flow from Haaland (1983) as presented by Kröger (1998) i.e.

$$f_D = 2.7778\left[\log_{10}\left\{\left(\frac{7.7}{Re}\right)^3 + \left(\frac{\varepsilon/d}{3.75}\right)^{3.33}\right\}\right]^{-2} \qquad (6.19)$$

where the roughness factor, ε, is assumed zero. The larger values predicted by the present code and found from using equation (6.17) compared to the values found from equation (6.19) are consistent with comments made by White (1991) that parallel plates show slightly higher friction factors than those found by using equation (6.19). The fully developed friction factor comparison for the various Reynolds numbers evaluated are shown in figure 6.27.

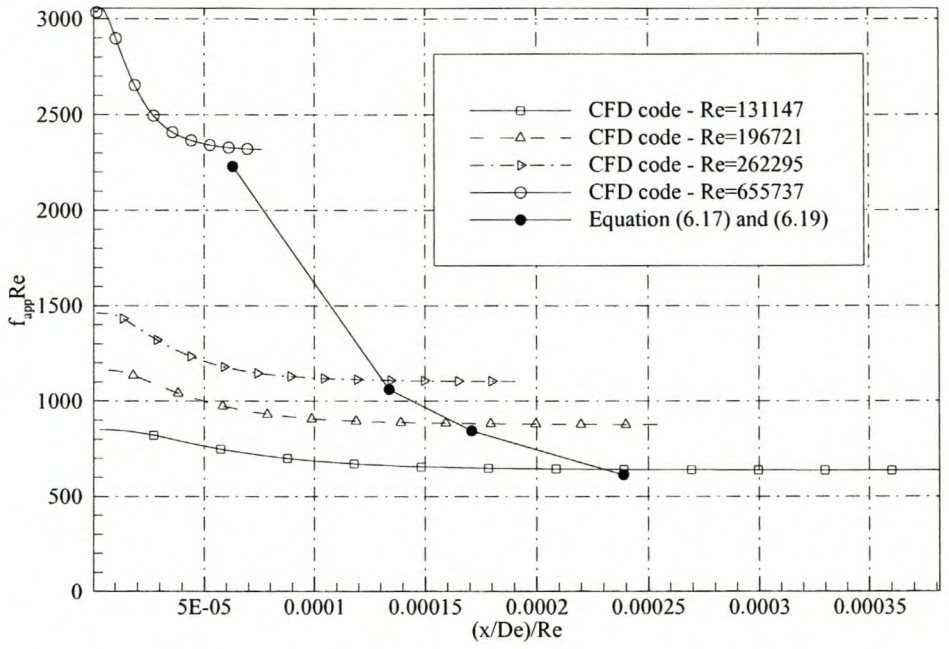

Figure 6.26. Friction factor distribution along the plates for Re=131147, Re=196721, Re=262295 and Re=655737.

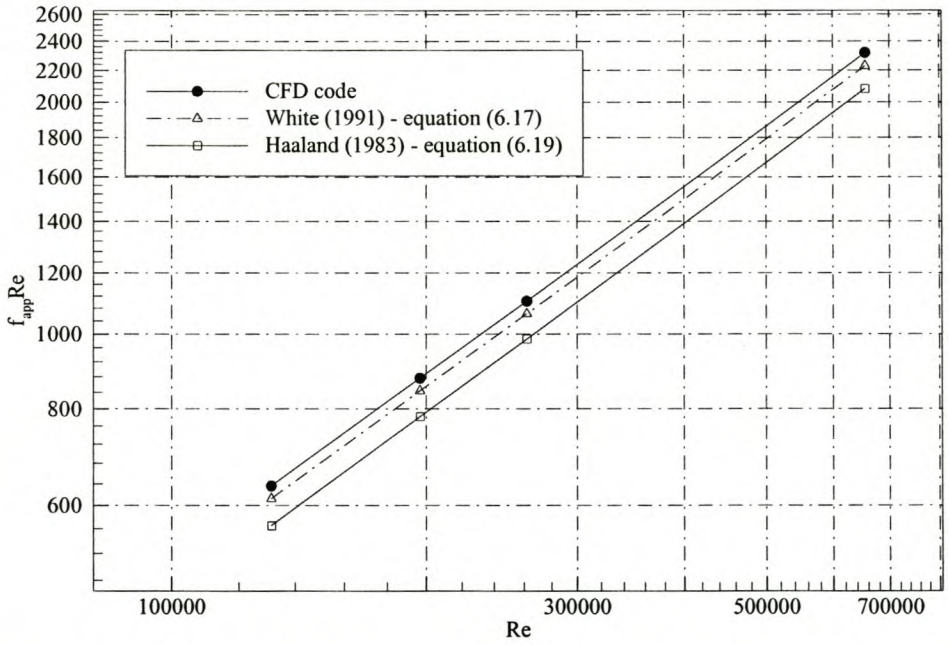

Figure 6.27. Fully developed friction factors for Re=131147, Re=196721, Re= 262295 and Re=655737.

The inlet and outlet dimensionless distance from the wall at the first node away from the wall, (y^+), for the different Reynolds number solutions are shown in figure 6.28. The maximum y^+ value is at the inlet due to the uniform inlet velocity and therefore the highest velocity gradient and shear velocity at the wall.

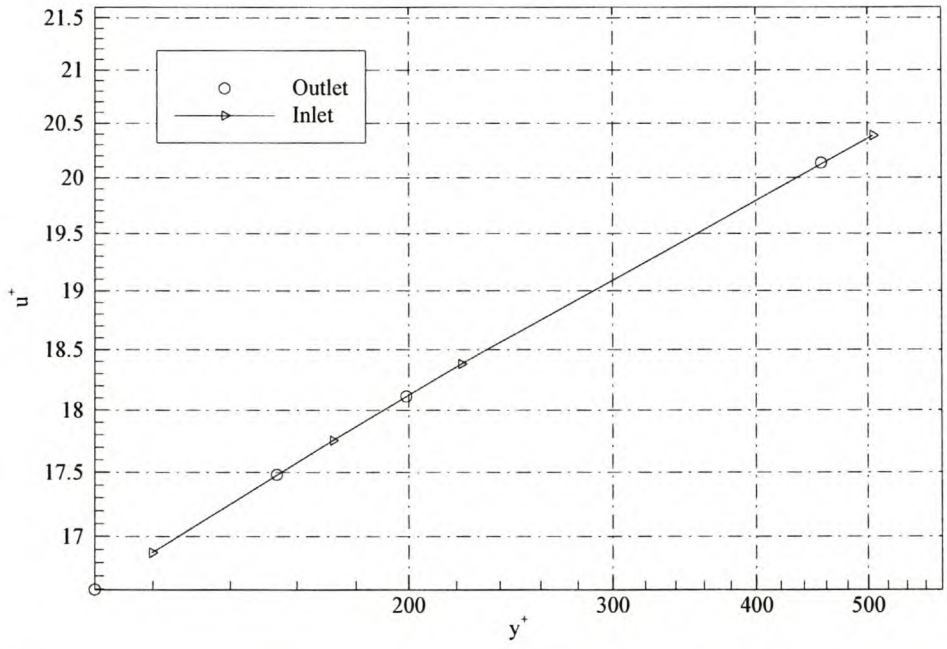

Figure 6.28. Dimensionless distance from the wall for Re=131147, Re=196721, Re= 262295 and Re=655737.

Figure 6.28 indicates that the minimum limiting criteria $y^+ > 30$ for the application of the $k-\varepsilon$ model is met for all Reynolds numbers. The maximum limit is exceeded but does not seem to influence the final solution. This is consistent with comments made by Thiart (1990) that the $y^+ < 100$ limitation need not be rigorously adhered to especially for higher Reynolds numbers. White (1991) also shows that for small pressure gradients, as found for these test cases, the logarithmic velocity relation employed for the $k-\varepsilon$ turbulence modeling is applicable within $35 \leq y^+ \leq 1000$.

It is important to note that the inlet boundary $k-\varepsilon$ values contribute largely to the final converged field solution. The inlet turbulent kinetic energy value is significant since it influences the entry lengths, frictions factors and heat transfer properties by controlling the

effective viscosity of the field. The results shown here were calculated with a turbulent intensity value of 3.7%. However, it was found that lower inlet turbulence levels (1%), do not significantly influence the friction factor and heat transfer characteristics since the turbulence levels of the flow are predominantly controlled by the wall boundary conditions i.e. the wall velocity gradient, wall shear velocity and law of the wall boundary condition. Similar remarks was made by Stephenson (1975). Therefore, for other applications such as for the solar collector numerical model, a turbulent intensity value of 1% will be employed.

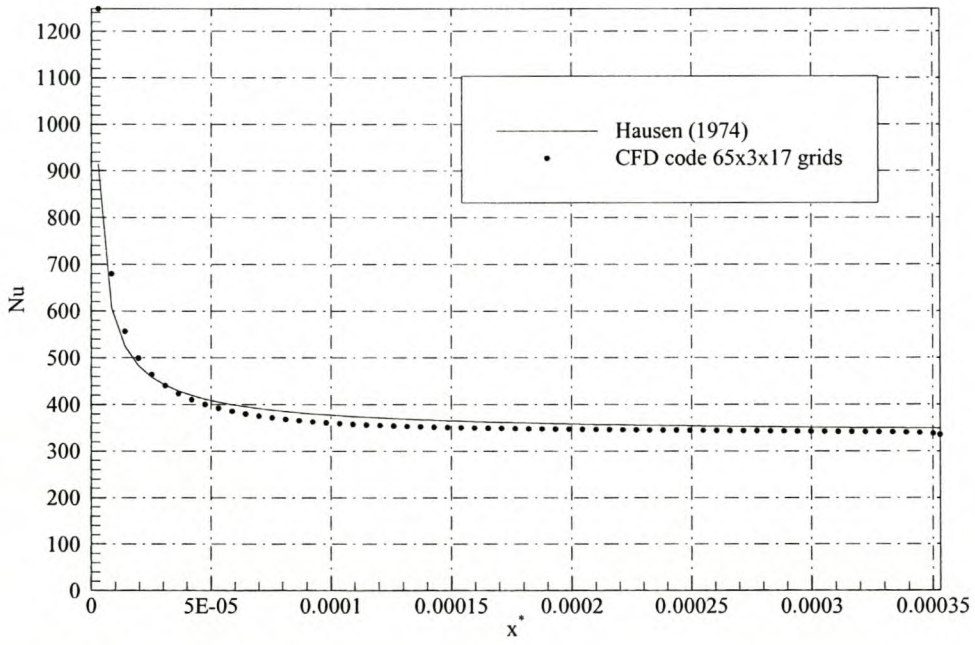

Figure 6.29. Nusselt number comparison for Re=196721

Figure 6.29 shows the code results of the heat transfer characteristics for Re=196721 compared to the results from an equation proposed by Hausen (1974) and as given by Kröger (1998) for the Nusselt number for developing flow in ducts

$$Nu = 0.0235\left(Re^{0.8} - 230\right)\left(1.8\,Pr^{0.3} - 0.8\right)\left[1 + \left(\frac{d}{L}\right)^{0.667}\right]\left(\frac{\mu}{\mu_w}\right)^{0.14} \qquad (6.\ 20)$$

where d_e, the effective diameter of the channel, equals twice the plate spacing. The viscosity ratio in equation (6.20) accounts for temperature gradients across the duct where μ_w is the fluid viscosity at the wall temperature and μ evaluated at the bulk mean fluid temperature T_f. The temperature dependence of the air viscosity can be expressed by the relation from Kröger (1998) i.e.

$$\mu_f = 2.287973 \cdot 10^{-6} + 6.259793 \cdot 10^{-8} \cdot T_f - 3.131956 \cdot 10^{-11} \cdot T_f^2 + 8.15038 \cdot 10^{-15} \cdot T_f^3 \quad (6.21)$$

The high heat transfer coefficients in the entrance region are due to a thin thermal boundary layer and subsequently high temperature gradients at the wall and near the entrance consistent with reports by Deisler (1954).

Table 6.3 and table 6.4 summarises the friction factor and heat transfer coefficient predictions for turbulent flow calculated from the results of the present code.

Table 6.3. Friction factor prediction and comparison for fully developed turbulent flow in a parallel duct.

Prediction from:	Re	$f_{app}Re$		% difference
		Numerical code (a)	Equation (6.17) (b)	$\frac{(a)-(b)}{(b)}$ %
Present code	196721	876.55	844.14	+3.84
Stephenson	192000	777.60	828.07	-6.09
Comini and Del Guidice	200000	796.00	855.41	-6.95

Table 6.4. Nusselt number prediction and comparison for fully developed turbulent flow in a parallel duct.

Prediction from:	Re	Nu		% difference
		Numerical code (a)	Equation (6.20) (b)	$\frac{(a)-(b)}{(b)}$ %
Present code, Pr_t=0.9	196721	334.89	348.88	-4.01
Stephenson, Pr_t=0.9	192000	321.21	348.51	-7.83

Table 6.3 indicates that although, as discussed earlier, the present code predicts larger outlet turbulent kinetic energy values compared to other numerical work done by Comini and Del Guidice (1985) and Stephenson (1976), it shows considerably better accuracy in predicting the fully developed friction factor for parallel ducts. The same applies to the prediction of the Nusselt number for turbulent flows in parallel ducts. The present code prediction shows very good agreement with results calculated using equation (6.20) and marginally better than the results from Stephenson (1976). The viscosity ratio in equation (6.20) was assumed one during the calculation of the Nusselt number for Re=192000 presented in table 6.4.

6.4 Steady, Turbulent Hydrodynamic and Thermal Developing Radial Flow between Parallel Plates

6.4.1 The numerical model

The flow conditions and fluid properties are the same as for the test case for turbulent flow between infinite parallel plates. The geometry is also of similar size except that the flow is between two circular plates instead of infinite plates. Two configurations were evaluated, both with a 65x7x17 grid. Both configurations have a plate length of L=10.0m and plate spacing of H=0.1m. The first test case models an axisymmetric circular wedge with an inlet to outlet area aspect ratio, a_r=1.01. An outer radius of r_o=1010.0m, inner radius of r_i=1000.0m and an included angle of θ=0.0001 radians are specified. Test case 2 models an outer to inner area

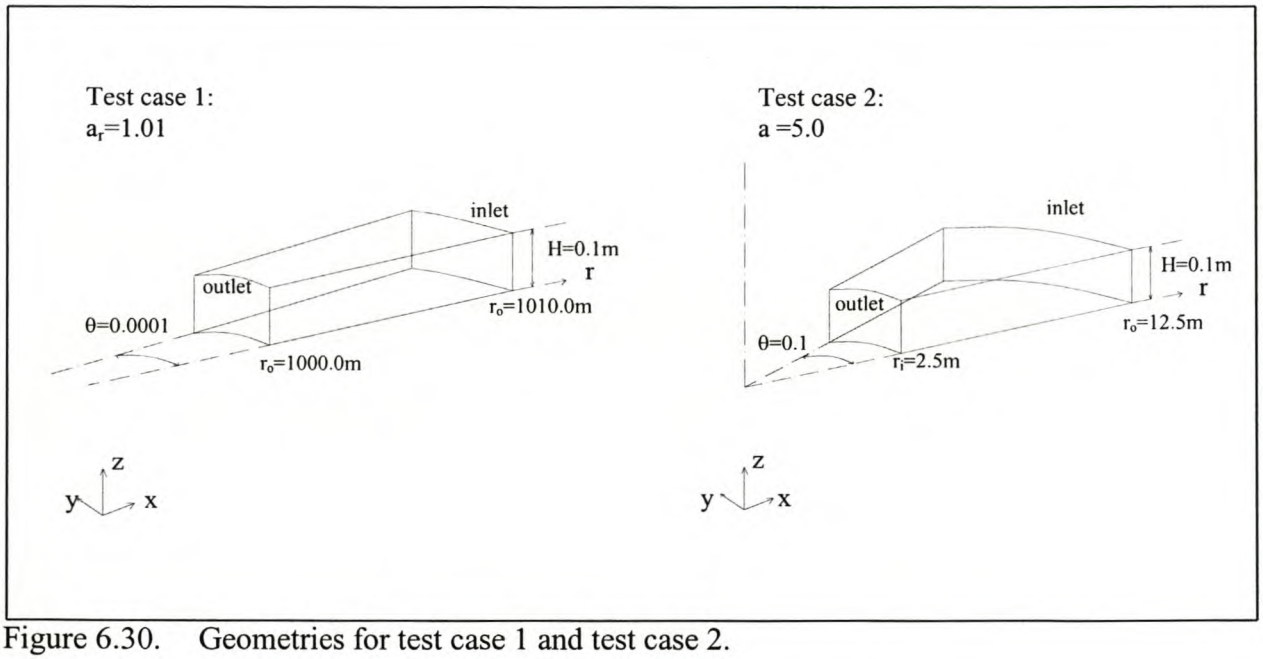

Figure 6.30. Geometries for test case 1 and test case 2.

aspect ratio of a_r=5.0. This test case has outer radius of r_o=12.5m., inner radius r_i=2.5m. and included angle of θ=0.1 radians. The test case geometries are shown in figure 6.30. The parallel plates are also evaluated with both smooth and rough surfaces according to the roughness model presented in chapter 2. The code results are compared to results from equations presented by Kröger (1999) for radial developing and fully developed flow.

Table 6.4 shows the solution parameters employed and figure 6.31 indicates the convergence history for both test cases. Computational speed was 0.0043 seconds/iteration/grid point.

Table 6.5 Solution parameters for turbulent flow between radial parallel plates

	Under-relaxation factors					Flux-blending
	α_p	α_v	α_k	α_ε	α_T	γ
Test case 1 a_r=1.01	0.2	0.8	0.2	0.2	0.8	0.9
Test case 2 a_r=5.0	0.2	0.8	0.2	0.2	0.8	0.9

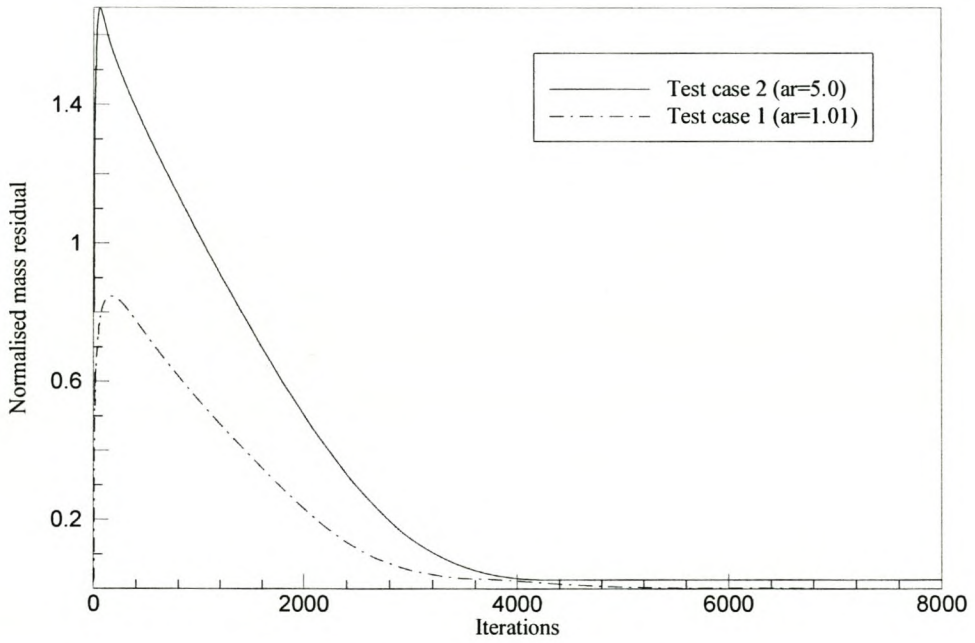

Figure 6.31. Convergence history for test case 1 and test case 2.

6.4.2 Code results

Only the numerical code results for a smooth surface test case 2 is presented. Figure 6.32 shows the computational domain and the resultant vector field plot is shown in figure 6.33 to figure 6.35. The pressure distribution contours are shown in figure 6.36. The temperature distribution contours are shown in figure 6.37. The velocity contours for the axial velocity components are shown in figures 6.38. Figure 6.39 shows the cross stream velocity contours. The turbulent kinetic energy and dissipation rate contours are shown in figures 6.40 and 6.41 respectively. The effective viscosity contour plot is shown in figure 6.42 while the dimensionless distance contours (y^+) for the first node away from the wall are shown in figure 6.43.

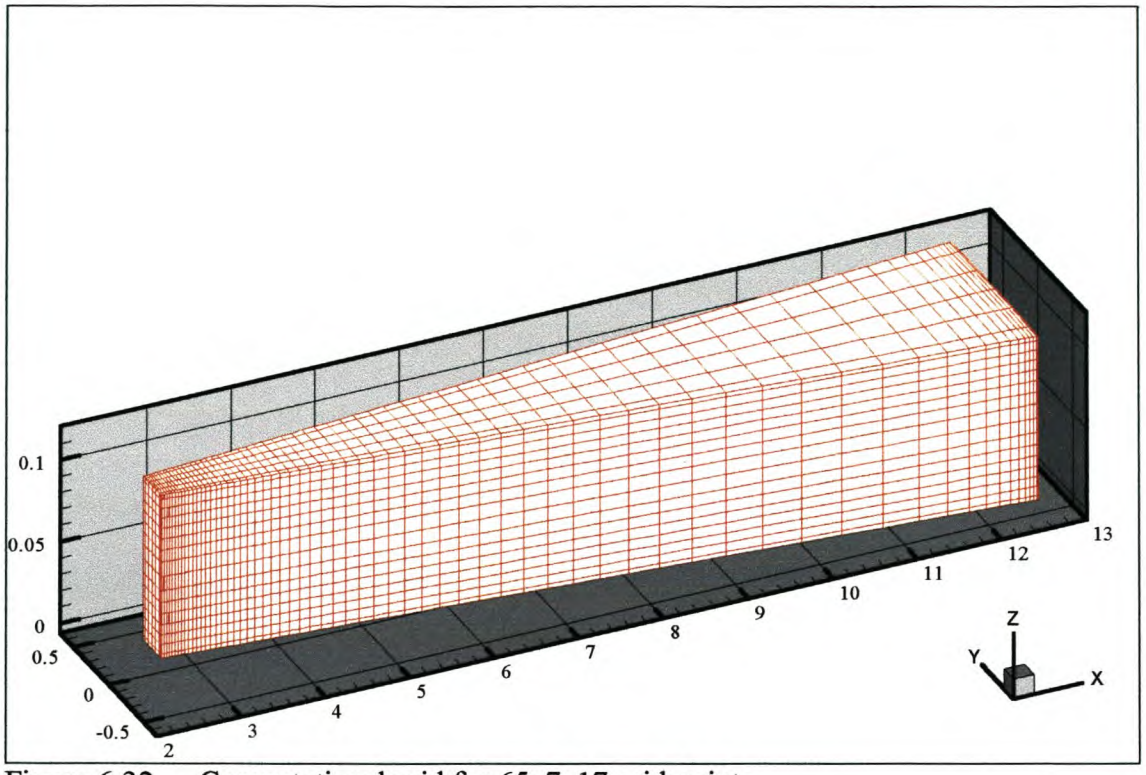

Figure 6.32. Computational grid for 65x7x17 grid points

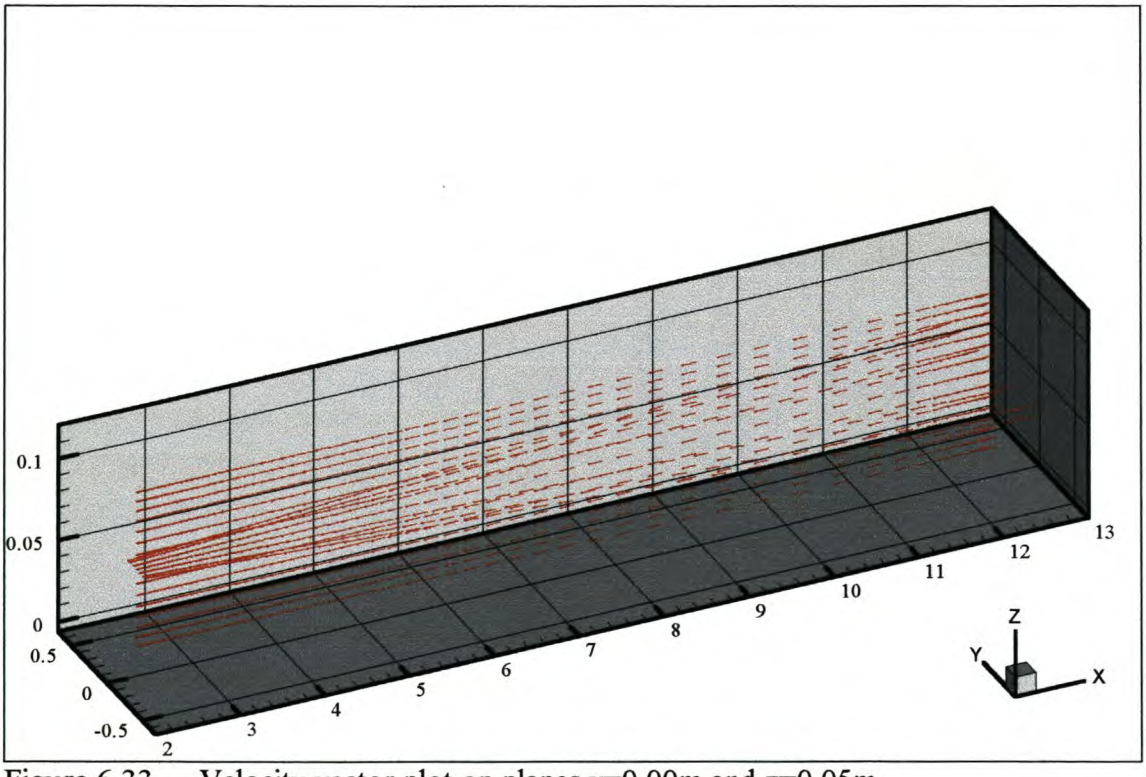

Figure 6.33. Velocity vector plot on planes y=0.00m and z=0.05m

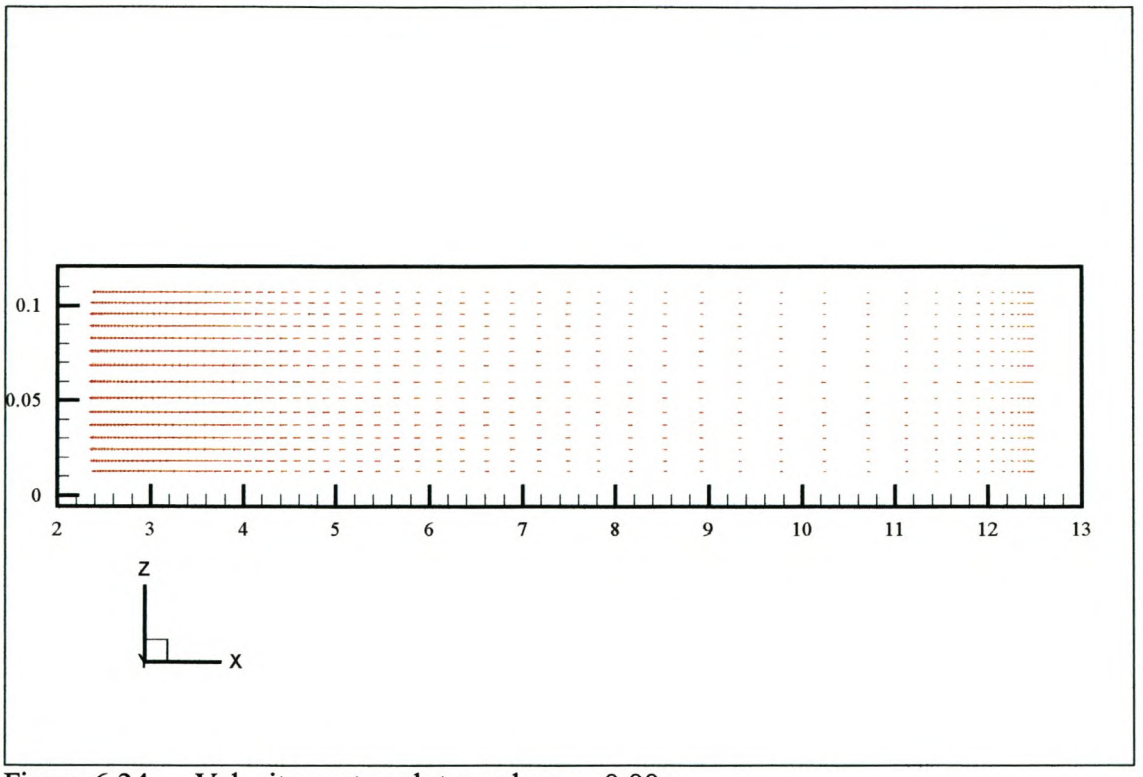

Figure 6.34. Velocity vector plot on plane y=0.00m

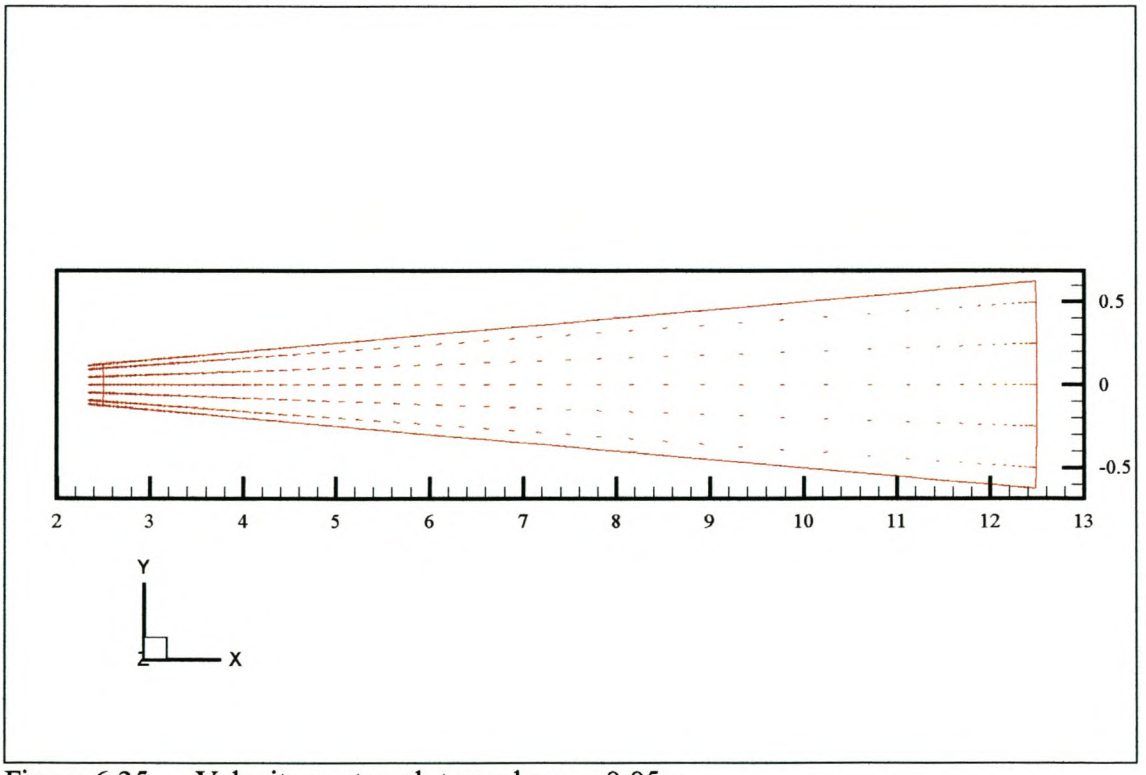

Figure 6.35. Velocity vector plot on plane z=0.05m

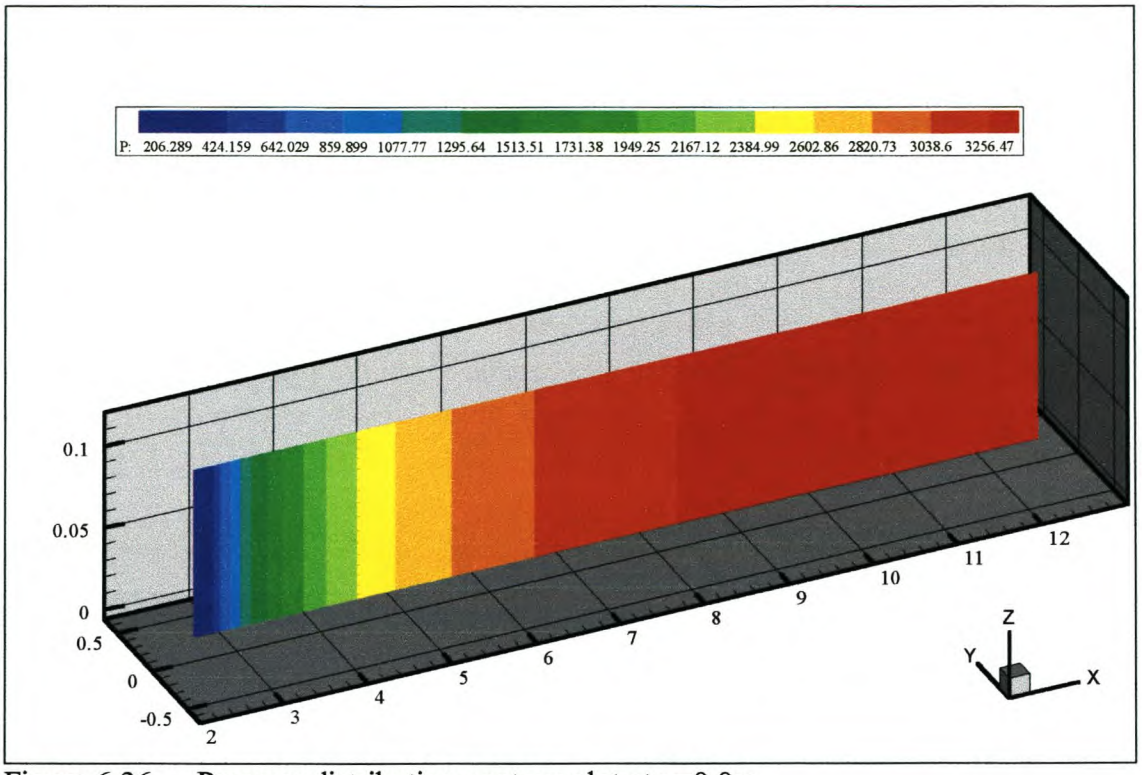

Figure 6.36. Pressure distribution contour plot at y=0.0m

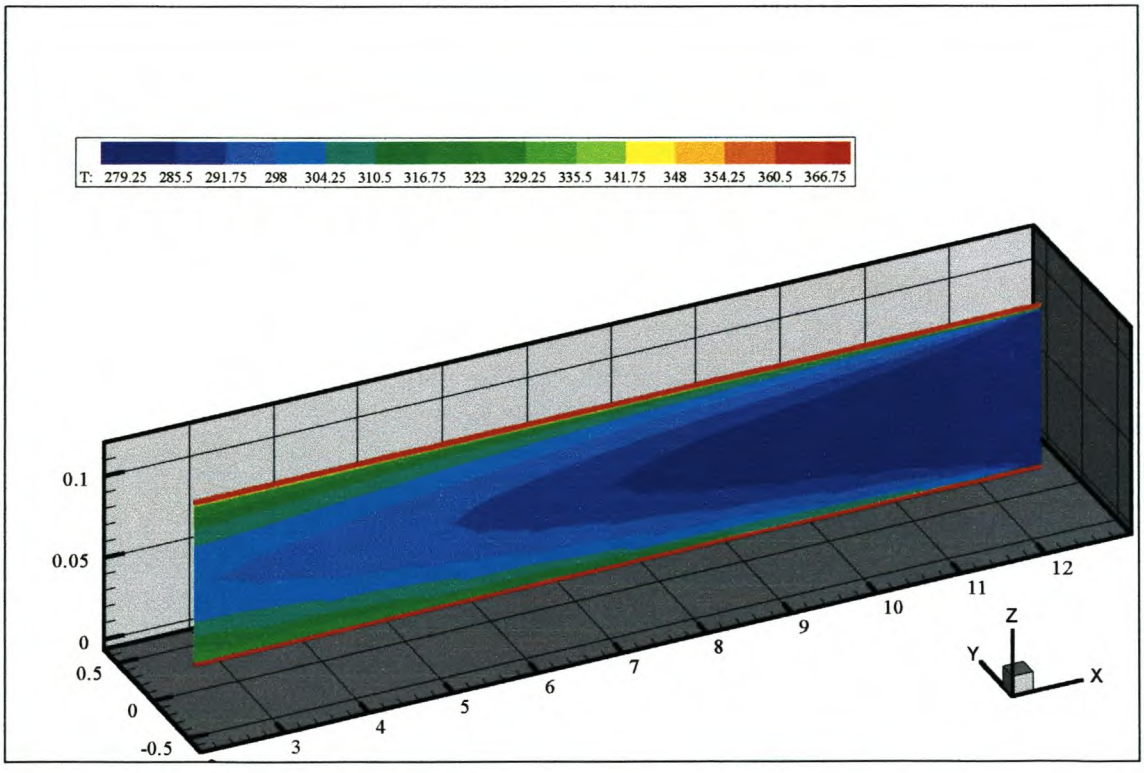

Figure 6.37. Temperature distribution contour plot at y=0.0m

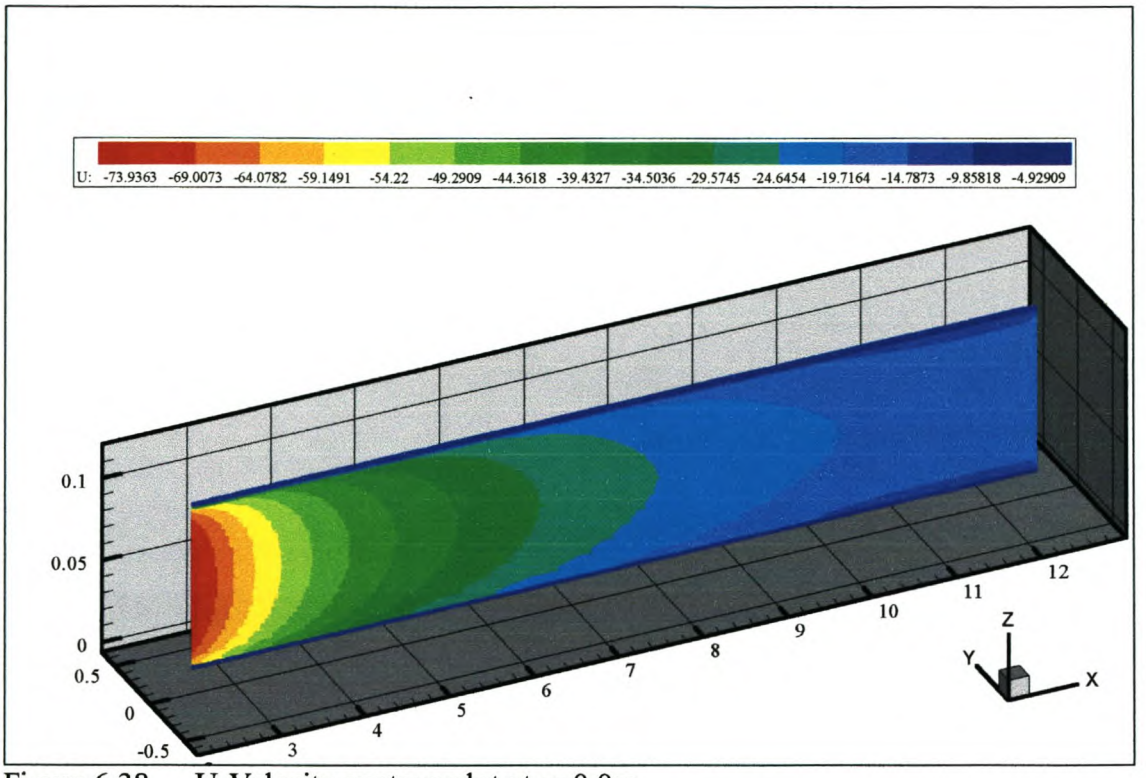

Figure 6.38. U-Velocity contour plot at y=0.0m

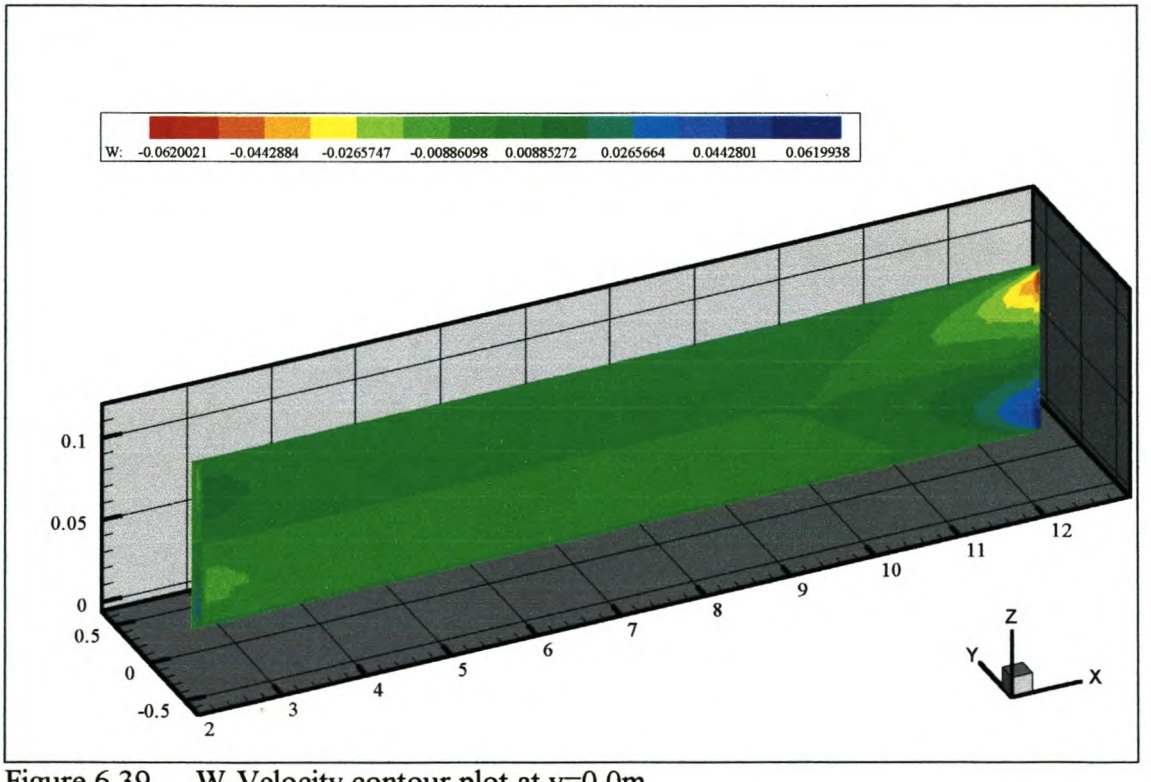

Figure 6.39. W-Velocity contour plot at y=0.0m

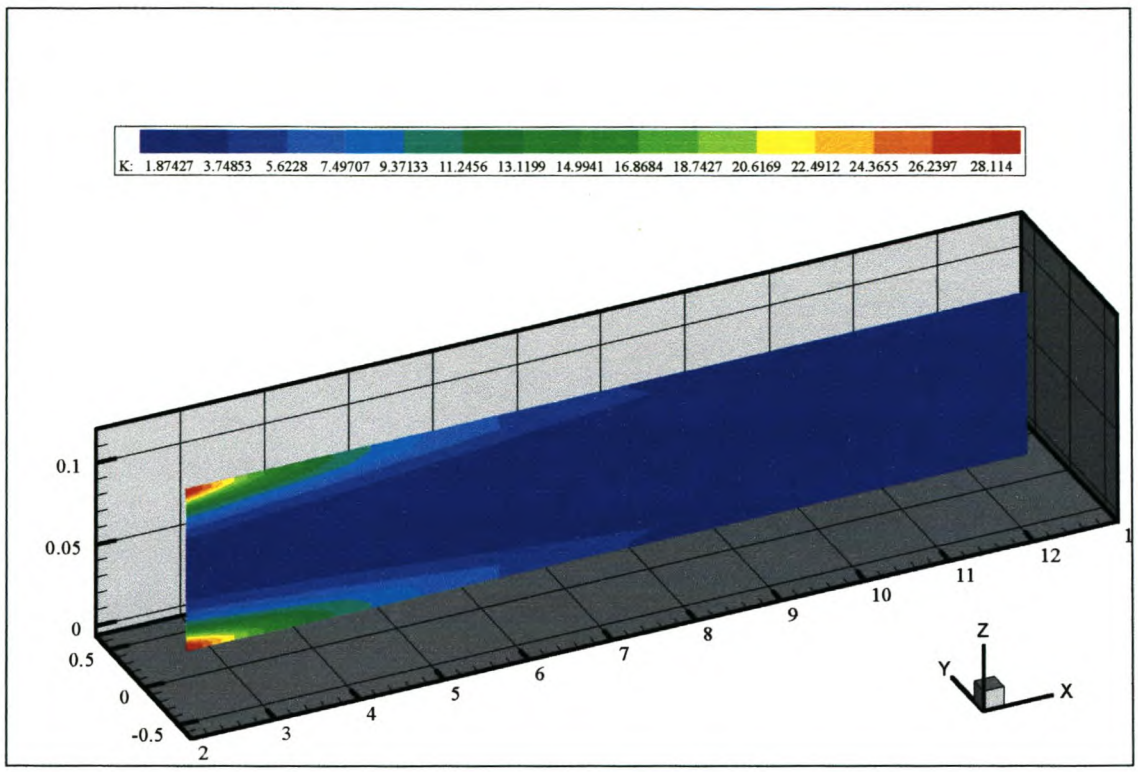

Figure 6.40. Turbulent kinetic energy contours plot at y=0.0m

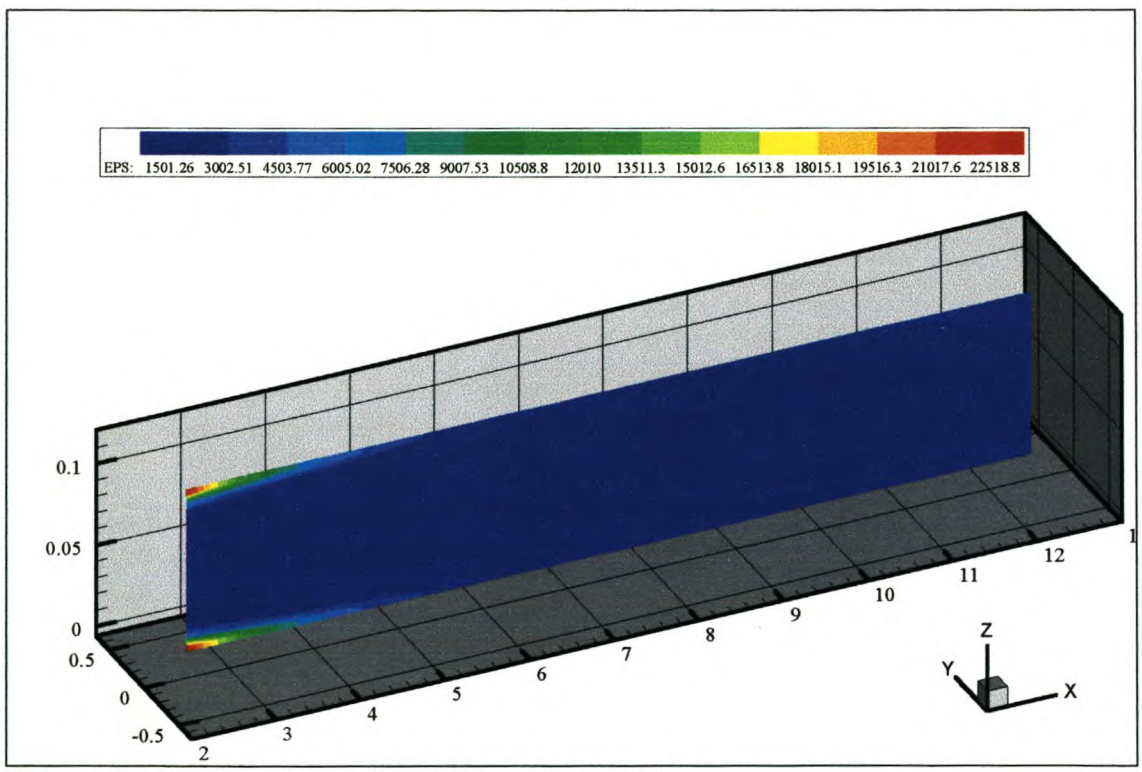

Figure 6.41. Dissipation rate contour plot at y=0.0m

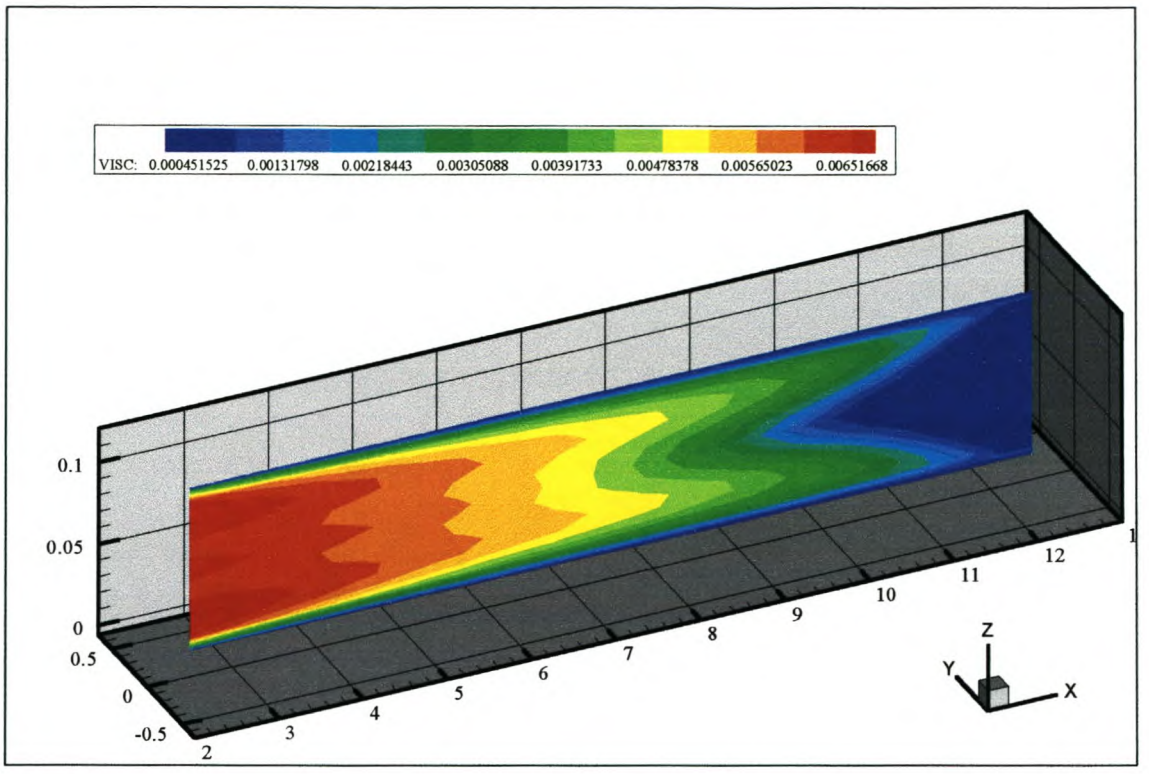

Figure 6.42. Effective viscosity contour plot at y=0.0m

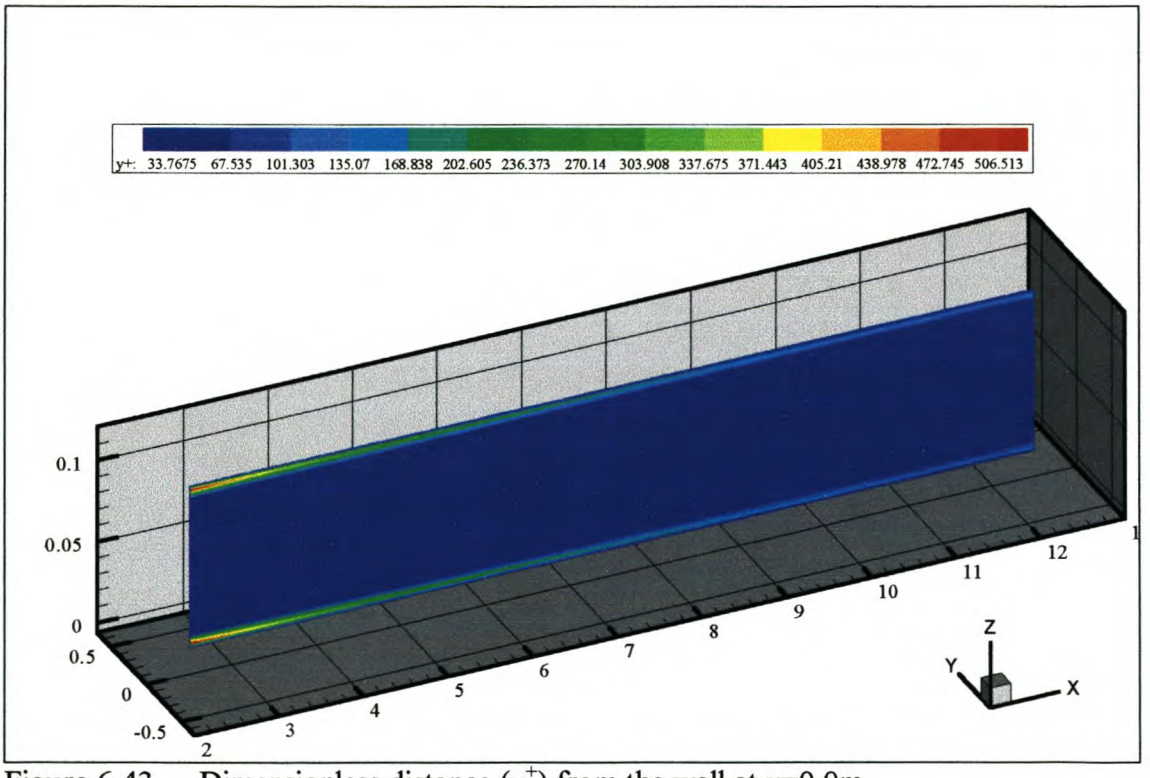

Figure 6.43. Dimensionless distance (y^+) from the wall at y=0.0m

6.4.3 Verification of results

Smooth radial parallel plates.

For test case 1, the flow is expected to behave very similar to the flow within the infinite parallel plates since the flow acceleration due to the area contraction is very small. Test case 2 however has an area change ratio of a_r=5.0 and consequently an average fluid flow acceleration of approximately the same ratio. This increasing core velocity should result in continuously increasing turbulence levels towards the wedge outlet.

Figure 6.44 shows the pressure loss coefficient due to friction for both test cases. The loss coefficients for both these test cases are also compared to the frictional pressure drop results from the turbulent infinite parallel plate predictions presented earlier in this chapter. The pressure drop due to frictional effects is expected to increase for higher turbulent levels, a phenomenon clearly shown in figure 6.44. Test case 1, compared to the results from the infinite parallel plates, shows an insignificant increase in the frictional pressure loss due to the slight increase in the velocity towards the outlet. Test case 2 shows a large increase in the frictional pressure loss due to the large velocity acceleration through the duct.

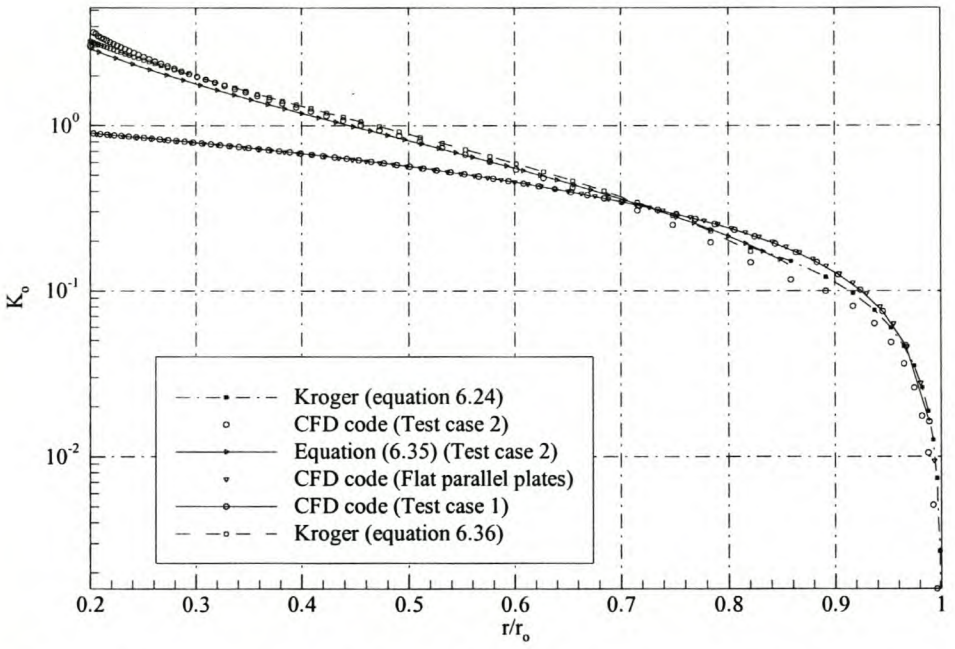

Figure 6.44. Pressure loss coefficient for smooth radial parallel plates

The pressure loss coefficient, Ko, due to friction on the two surfaces of the radial plates was calculated from the average static pressure drop results of the CFD code. The static pressure drop along the plates was calculated by subtracting the dynamic pressure from the total average pressure as calculated by the code i.e.

$$\Delta p_s = \left(\bar{p}_o - \bar{p}_r\right) - \frac{1}{2}\rho\left(\bar{u}_o^2 - \bar{u}(r)^2\right) \tag{6. 22}$$

The static pressure loss coefficient based on the inlet velocity then becomes

$$K_0 = \frac{\Delta p_s}{\frac{1}{2}\rho\bar{u}_0^2} \tag{6. 23}$$

The loss coefficient due to wall friction in the entrance region between two surfaces of radial plates and based on the inlet velocity was derived by Kröger (1999) i.e.

$$K_0 = 0.08038\left(\frac{\mu H}{\dot{m}}\right)^{0.1667}\left(\frac{r_o}{H_0}\right)F_s\left(\frac{r}{r_0}\right) \tag{6. 24}$$

where,

$$F_s = \left(1 - \frac{r}{r_0}\right)^{5/6}\left[1.51 + (1.71 - 2.5b)\left(1 - \frac{r}{r_0}\right)^{5/6}\right] \tag{6. 25}$$

The mass flow, $\dot{m}$, in equation (6.24) is the total mass flow through the plates, $\dot{m} = 2\pi r_o H\rho\bar{u}_o$. The above formulation of Kröger (1999) allows for the variation of the top plate height according to the relation

$$H = H_0\left(\frac{r}{r_0}\right)^{-b} \tag{6. 26}$$

where b is a parameter, $0 \le b \le 1$. For the present calculations b=0 representing a parallel radial plates.

Since the boundary layer for high Reynolds number flows is expected to be thin, the approximate free stream velocity is inversely proportional to the radius, Kröger (1999), i.e.

$$u_c \propto \frac{1}{r} \tag{6. 27}$$

The shear stress at the wall is directly proportional to the velocity gradient $(\frac{\partial u}{\partial n})$ at and normal to the wall and therefore from equation (6.27) one expects the shear stress also to be inversely proportional to the radius (r). Based on the above assumption and by employing the logarithmic law, equation (6.16), for the velocity distribution for fully developed turbulent flow between the plates, one may find the wall shear velocity for fully developed accelerating flows between radial parallel plates, (appendix D), i.e.

$$u_\tau(r) = \left[\frac{-\left(x_1 e^{Px_1} - Z\right)\left(x_1 - x_2\right)}{\left(x_1 e^{Px_1} - x_2 e^{Px_2}\right)} + x_1 \right]^{-1.0} \tag{6. 28}$$

$$x_1 = \frac{1}{P(r)} \ln\left(\frac{ZP(r)}{\ln(Z)}\right) \tag{6. 29}$$

$$x_2 = \frac{1}{P(r)} \left[\ln(Z) - \ln\left(\frac{1}{P(r)} \ln\left(\frac{ZP(r)}{\ln(Z)}\right)\right)\right] \tag{6. 30}$$

$$P(r) = u_c(r) \cdot \kappa \tag{6. 31}$$

$$Z = \frac{EH}{2\nu} \tag{6. 32}$$

where E=0.91 and $\kappa = 0.41$. By assuming a thin turbulent boundary layer, the centerline flow velocity in equation (6.31) may be approximated by

$$u_c(r) = \frac{\dot{m}}{2\pi r \rho H} \tag{6. 33}$$

Kröger (1999) shows that the momentum balance on a control volume located between two parallel discs as shown by figure 6.30 yields the radial frictional pressure drop i.e.

$$\frac{\partial p}{\partial r} = \frac{2\tau_w(r)}{H} \tag{6. 34}$$

Integrating equation (6.34) one may find the pressure loss coefficient due to wall shear and based on the uniform inlet velocity as

$$K_0 = \frac{p_{r_0} - p_r}{0.5\rho u_0^2} = \frac{1}{0.5\rho u_0^2}\int_{r_o}^{r}\frac{2}{H}\tau_w(r)dr \tag{6. 35}$$

where the shear stress $\tau_w(r)$ is given by equation (6.28) and $u_\tau = \sqrt{\tau_w / \rho}$.

Kröger (1999) presents another equation for the pressure loss coefficient for the fully developed region for turbulent radial flows between smooth surfaces and based on the average inlet velocity i.e.

$$K_0 = \frac{1.4633\cdot 10^{-3}\dot{m}^{1.8}\mu^{0.2}\left[r_{fd}^{(3b-08)} - r^{(3b-0.8)}\right]}{\rho\left(H_0 r_0^b\right)^3(3b-0.8)}\frac{1}{0.5\rho u_0^2} \tag{6. 36}$$

Figure 6.44 indicates that the present code prediction of the pressure loss coefficient calculated using equation (6.23) compares well with the results from equation (6.24) for the pressure loss coefficient for the entrance region, as well as with results calculated by employing equation (6.36) for the fully developed region.

Figure 6.45 shows the local heat transfer coefficient prediction calculated from results of the present code. The results for test case 1 and 2 are also compared to the results for the infinite parallel plates presented earlier in this chapter. The local heat transfer results for test case 1 again show an insignificant increase compared to the infinite parallel plates results while test case 2 shows a considerable increase in heat transfer coefficient.

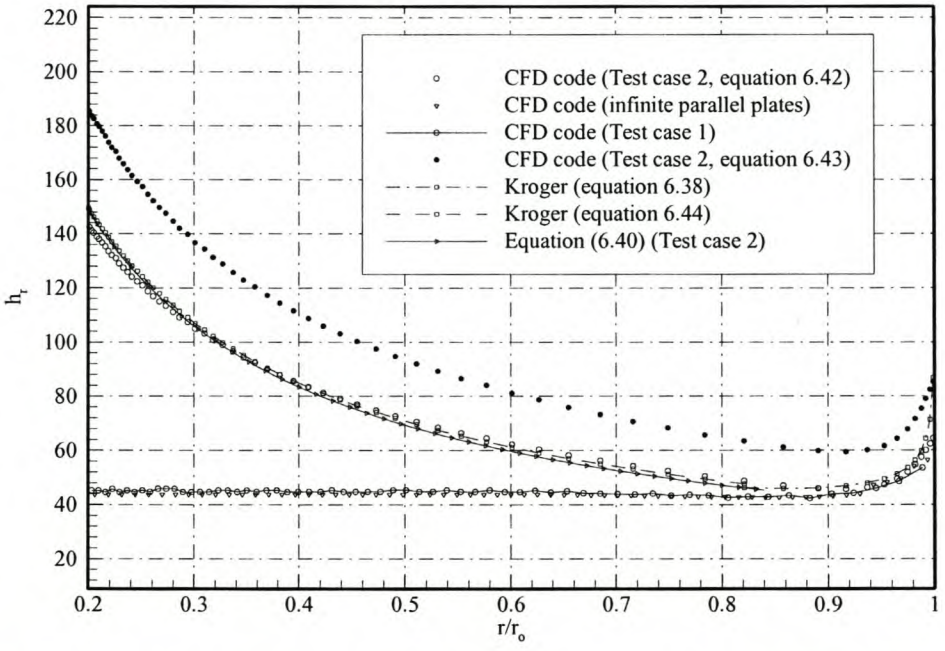

Figure 6.45. Local heat transfer coefficient for smooth radial parallel plates

The accelerating radial flows between the parallel plates gives rise to higher turbulent levels along the length of the plates which in turn increases the heat transfer from the walls due to increased eddy conductivity. Kröger (1999) employs the Colburn analogy, Rohsenow and Choi (1961), i.e.

$$\frac{h_r P_r^{2/3}}{C_p \rho u_c(r)} = \frac{\tau_w(r)}{\rho\left(u_c(r)\right)^2} \qquad (6.37)$$

to predict the local Nusselt number for flows within the entrance region of a smooth radial collector based on the integral analysis of the boundary layer. The formulation is

$$Nu_r = 0.0032\,Pr^{0.333}\left(1-\frac{r}{r_o}\right)\left(\frac{\dot{m}}{\mu H}\right)^{0.833}\left(\frac{r}{r_o}\right)^{0.8(1-b)}\left[\frac{6.218-15.08b}{\left(\frac{r}{r_o}\right)^{1.2-0.2b}-\left(\frac{r}{r_o}\right)^{2.743-3.943b}}\right]^{1/6} \qquad (6.38)$$

with the local heat transfer coefficient found from

$$h_r = \frac{Nu_r \cdot k}{(r_o - r)} \qquad (6.39)$$

Furthermore, the fully developed local heat transfer coefficient may also be found by using equation (6.37) i.e.

$$h_r(r) = \frac{\tau_w(r)\cdot C_p}{u_c(r)\cdot P_r^{0.667}} \qquad (6.40)$$

where the shear stress term $\tau_w(r)$ is again found by employing equation (6.28).

An energy balance at the wall yields the formulation for the calculation of the heat transfer coefficient from the present code results i.e.

$$h_r = \frac{k_e\left(\frac{\partial T}{\partial n}\right)_w}{(T_w - T_f)} \qquad (6.41)$$

where k_e is the effective conductivity at the wall as per equation (2.60) and $\left(\frac{\partial T}{\partial n}\right)_w$ is the local temperature gradient at and normal to the wall. The wall temperature gradient may be found from the following approximation for orthogonal control volumes at the boundary

$$\left(\frac{\partial T}{\partial n}\right)_w = \frac{T_w - T_1}{z_w - z_1} \tag{6. 42}$$

where T_1 and z_1 are the temperature and z-coordinate at the first node away from the wall.

A second order approximation for the first derivative of temperature at the wall may also be found from a parabola fit through a point on the wall and two inner points, given by Perić (1996), i.e.

$$\left(\frac{\partial T}{\partial n}\right)_w = \frac{-T_3(z_2 - z_w)^2 + T_2(z_3 - z_w)^2 - T_w\left[(z_3 - z_w)^2 - (z_2 - z_w)^2\right]}{(z_2 - z_w)(z_3 - z_w)(z_3 - z_2)} \tag{6. 43}$$

where the subscripts 2 and 3 refers to first and second grid points away from the wall respectively. From figure 6.45 it is evident that equation (6.42) provides a more accurate approximation of the local temperature gradient than equation (6.43). For turbulent flows the local temperature gradient at the wall will generally be larger than the value given by equation (6.42) but also smaller than the value from equation (6.43).

Kröger (1999) presents an equation for the fully developed local Nusselt number for radial flows between smooth parallel plates i.e.

$$Nu_r = \frac{(f_D / 8)(Re - 1000)\,Pr}{\left[1 + 12.7(f_D / 8)^{0.5}(Pr^{0.67} - 1)\right]} \tag{6. 44}$$

where the local heat transfer may be found from

$$h_r = \frac{Nu_r k}{d_e} \tag{6. 45}$$

The Darcy friction factor for a smooth surface in equation (6.44) may be given by

$$f_D = \left(1.82 \log_{10} Re - 1.64\right)^{-2} \qquad (6.46)$$

The local Reynolds number in equations (6.44) and (6.46) is based on the local centreline velocity, equation (6.33) and a hydraulic diameter of twice the plate spacing. It is evident that there exists good agreement between the code predictions of the local heat transfer coefficient and those found by using equation (6.38) for the entrance region and equations (6.40) and (6.44) for the fully developed region.

The above pressure drop and heat transfer correlations indicate that both the present code and the analytical relations predicts a similar behaviour of radial air flow between smooth parallel plates assuming that no flow separation occurs. It also suggests that the k-ϵ turbulence model is suitable for application to these types of flows.

Rough surface radial parallel plates.

The modified turbulence model for rough surface boundaries as described in chapter 2 is employed to evaluate the effects of roughness on the frictional pressure drop and local heat transfer coefficient. One expects the roughness to increase the turbulence level with subsequent rise in the frictional pressure drop as well as local heat transfer from the walls. All flow properties and test case geometries remain the same as for the smooth plate evaluation. An equivalent sand roughness length of $\varepsilon = 1\% \cdot H = 0.001\text{m}$ was employed.

Figure 6.46 shows the code prediction of the frictional pressure drop along the plates for test case 2. Kröger (1999) derived an equation for the frictional pressure loss coefficient for developing radial flows between rough surfaces. This loss coefficient, based on the average inlet velocity, is

$$K_0 = 0.0333\left(\frac{r_0}{H_0}\right)\left(\frac{\varepsilon}{r_0}\right)^{0.2026} F_r\left(\frac{r}{r_0}\right) \qquad (6.47)$$

with

$$F_r = \left(1 - \frac{r}{r_0}\right)^{0.797}\left[1.97 + \left(2.1 - 3.21b + 4.79q - 9.18bq\right)\left(1 - \frac{r}{r_0}\right)^{0.797}\right] \tag{6. 48}$$

$$q = \frac{\mu H_0 r_0}{\varepsilon \dot{m}} \tag{6. 49}$$

and for constant plate spacing b=0, as per equation (6.26). This loss coefficient is applicable to radial developing flows. Kröger (1999) presents another equation for fully developed radial flows between rough parallel plates i.e.

$$K_0 = \frac{0.632 \cdot 10^{-3} \varepsilon^{0.254} \dot{m}^2}{\rho\left(H_0 r_0\right)^{3.254}}\left[4.468\left(\frac{\mu H_0 r_0}{\dot{m}\varepsilon}\right)^{0.51} \frac{\left\{r_{fd}^{(2.7446b-0.49)} - r^{(2.7446b-0.49)}\right\}}{(2.7446b - 0.49)}\right.$$

$$\left. + \frac{\left\{r_{fd}^{3.254b-1} - r^{3.254b-1}\right\}}{(3.254b - 1)}\right]\frac{1}{0.5\rho u_0^2} \tag{6. 50}$$

This equation describes the radial frictional pressure drop from the fully developed radius, r_{fd}, to any other smaller radius. From figure 6.46 it is evident that good agreement exists between the present code prediction of the frictional pressure loss and the results calculated by using equations (6.47) and (6.50).

Figure 6.47 illustrates the present code prediction of the local heat transfer coefficient compared to results found by employing equations derived by Kröger (1999) for the local heat transfer coefficient for developing and fully developed turbulent flows between rough radial plates.

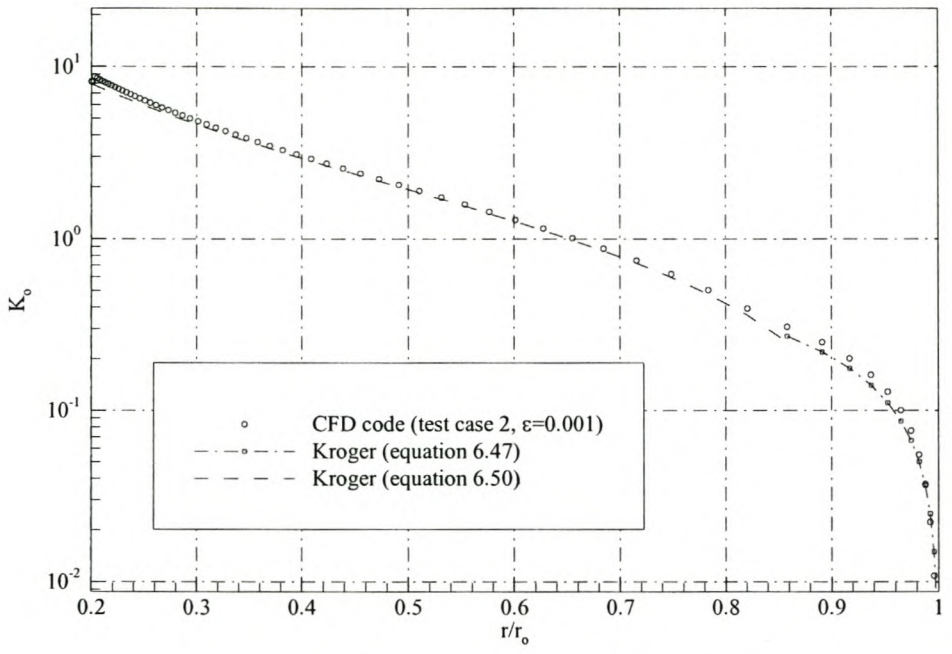

Figure 6.46. Pressure loss coefficient for rough radial parallel plates, $\varepsilon = 0.001$m

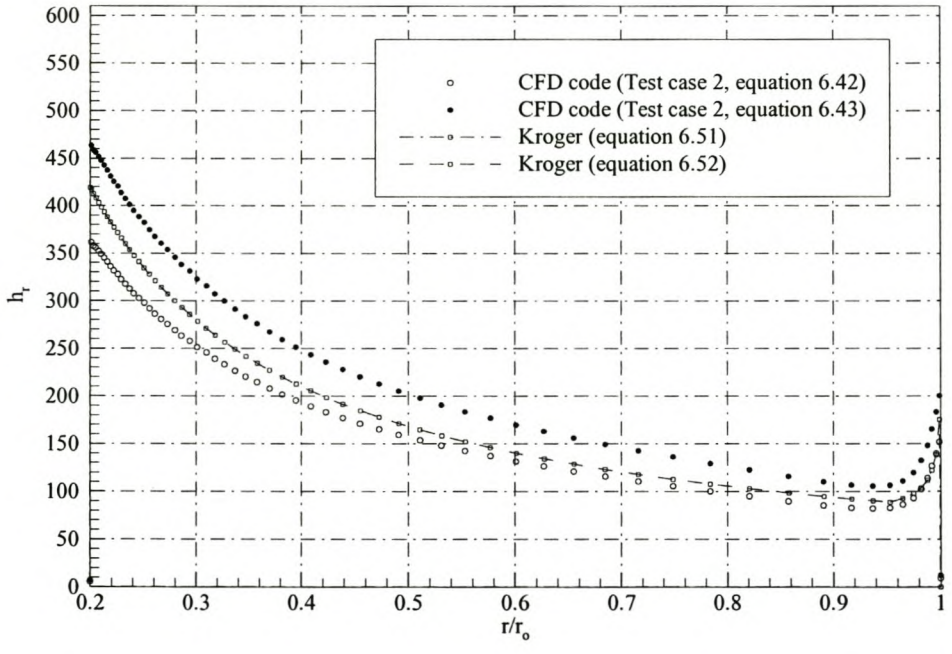

Figure 6.47. Local heat transfer coefficient for rough radial parallel plates, $\varepsilon = 0.001$m .

Kröger (1999) derived an equation for the local Nusselt number for developing radial flows between rough surfaces i.e.

$$Nu_r = 0.001325\,Pr^{0.333}\left(1-\frac{r}{r_0}\right)\left(\frac{\dot{m}}{\mu H_0}\right)\left(\frac{\varepsilon}{r_0}\right)^{0.2026}\left(\frac{r_0}{r}\right)^{1-b}$$

$$\times\frac{4.953q\left(\frac{r}{r_0}\right)^{0.51(1-b)}+1}{\left\{q\,\frac{\left(\frac{r}{r_0}\right)^{1.51-0.51b}-\left(\frac{r}{r_0}\right)^{2.866-4.120b}}{2.550-6.787b}+\frac{\left(\frac{r}{r_0}\right)-\left(\frac{r}{r_0}\right)^{2.866-4.120b}}{17.38-38.37b}\right\}^{0.2026}} \qquad (6.\ 51)$$

where the local heat transfer coefficient is found from equation (6.39). The local Nusselt number for the fully developed region is given by Kröger (1999) as

$$Nu_r = \frac{\left(f_D/8\right)\left(Re(r)-1000\right)Pr}{\left[1+12.7\left(f_D/8\right)^{0.5}\left(Pr^{0.67}-1\right)\right]} \qquad (6.\ 52)$$

with the local heat transfer coefficient found from equation (6.45). The Darcy friction factor in equation (6.52) may be found from an equation from Haaland as presented by Kröger (1999) i.e.

$$f_D = 0.3086\left[\log_{10}\left\{\frac{6.9}{Re}+\left(\frac{\varepsilon/H}{7.4}\right)^{1.11}\right\}\right]^{-2} \qquad (6.\ 53)$$

The local Reynolds number in equations (6.52) and (6.53) is based on the local centreline velocity, equation (6.33) and a hydraulic diameter of twice the plate spacing. Good agreement is found for the entrance region between the present code predictions of the local heat transfer coefficient and the results found by using equations (6.52) and (6.53). However, towards the

outlet, in the fully developed region, equation (6.52) predicts higher local heat transfer coefficients than predicted by the present code. This may be attributed to the code prediction of smaller local velocity and temperature gradients near the wall. The local heat transfer coefficient prediction is again higher when approximating the local wall temperature gradient by using equation (6.43) instead of equation (6.42). For turbulent flows, the actual local temperature gradient will generally be higher than the value calculated by using equation (6.42) and smaller than calculated from equation (6.43). Therefore the code predicted heat transfer coefficient would fall between the values shown in figure 6.47.

For the purpose of this study the present code satisfactorily predicts flow properties, frictional pressure losses and heat transfer characteristics for developing and fully developed turbulent radial flows over rough surfaces. Chapter 7 will apply the present code to model the air flow behaviour within an actual solar collector of similar geometry as modeled above.

6.5 Steady, Turbulent Hydrodynamic Developing Flow Between Infinite Parallel Plates with Non-orthogonal Control Volumes

6.5.1 The numerical model

A similar model geometry flow conditions and fluid properties are modeled and employed as discussed in section 6.3. The exception being that non-orthogonal control volumes are generated by moving the previously generated orthogonal control volume corners in alternate directions. The results may be compared to those found for orthogonal control volumes since the same flow conditions and fluid properties are employed.

Three grid configurations were evaluated namely 65x3x7, 99x3x17 and 121x3x17 to ensure that a grid independent solution was achieved. Only the results for the 121x3x17 grid, shown in figure 6.49, are presented and discussed here. Figure 6.48 shows the convergence history for this evaluation. The under-relaxation factors employed are shown in table 6.6

Table 6.6 Solution parameters for turbulent flow between parallel plates for non-orthogonal control volumes

Under-relaxation factors					Flux-blending
α_p	α_V	α_k	α_ε	α_T	γ
0.2	0.8	0.2	0.2	0.9	0.9

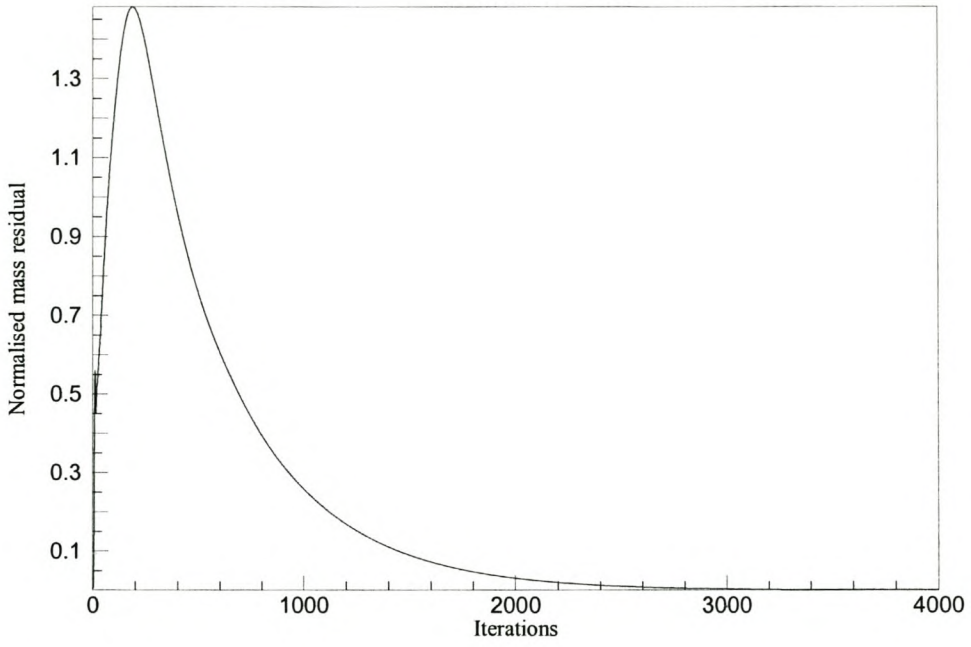

Figure 6.48 Convergence history

The minimum angle between the interface vector and the nodal vector ranged from 90° to 74° while corner angles ranged from 75° to 90° and 90 to 104°. The control volumes near the boundaries remained orthogonal since the non-orthogonal formulation for the present study, as presented in chapter 5, were not extended to include non-orthogonality at boundary control volumes.

6.5.2 Code results

The results shown in figure 6.50 to figure 6.59 indicate very good agreement and comparison to the results found and discussed in chapter 6.3.2 for the same geometry but with orthogonal control volumes.

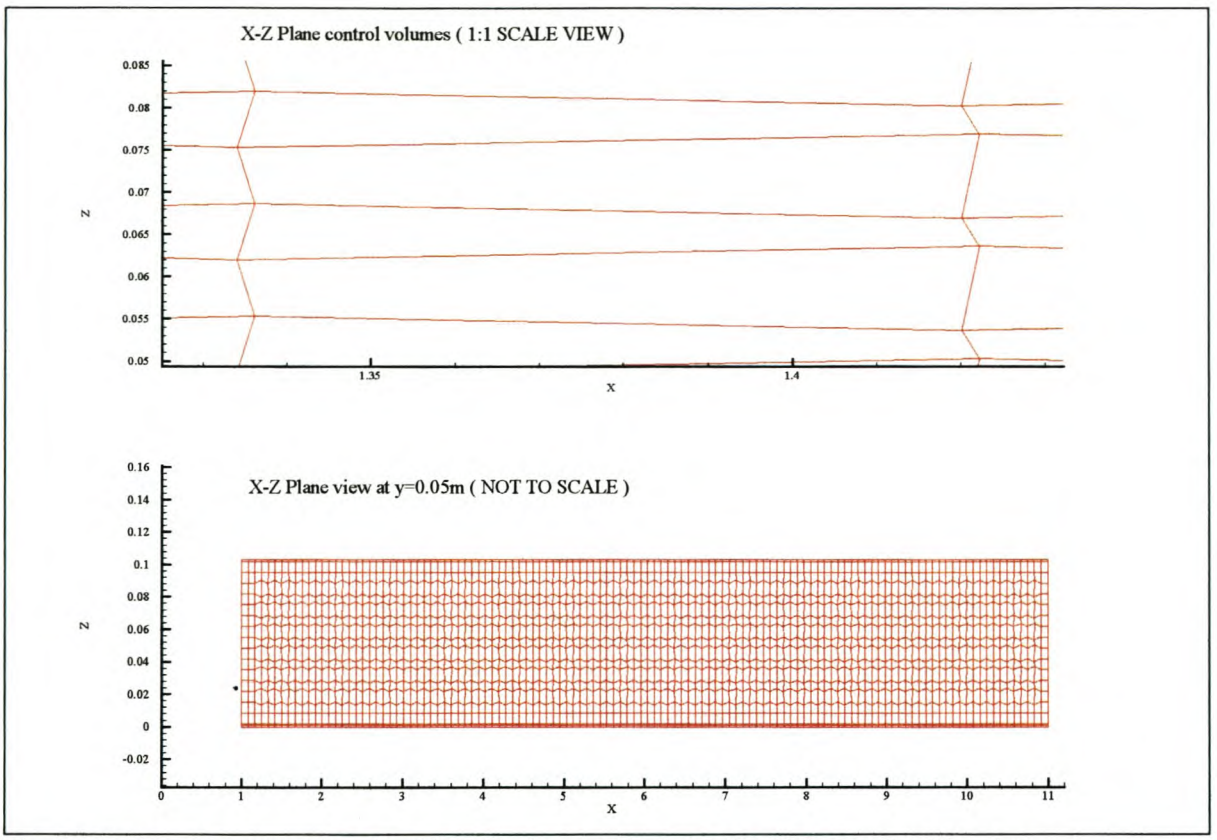

Figure 6.49. Computational grid X-Z plane at Y=0.05 for 121x3x17 grid points.

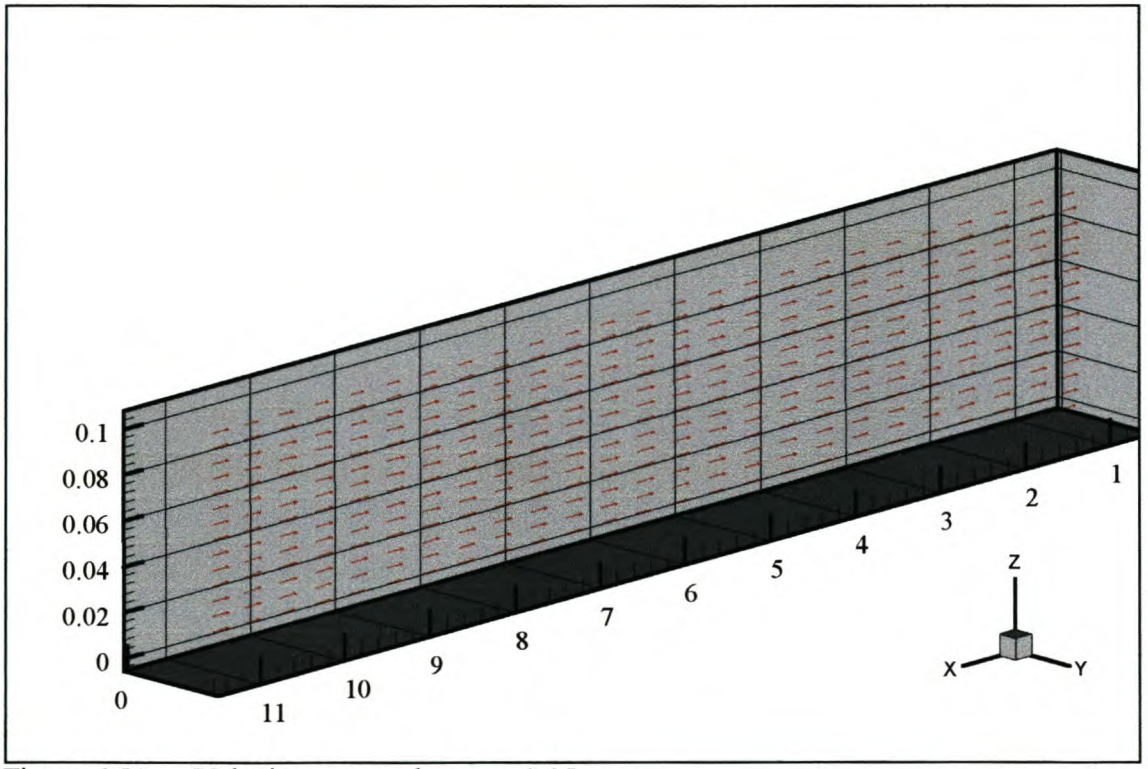

Figure 6.50. Velocity vector plot at y=0.05m

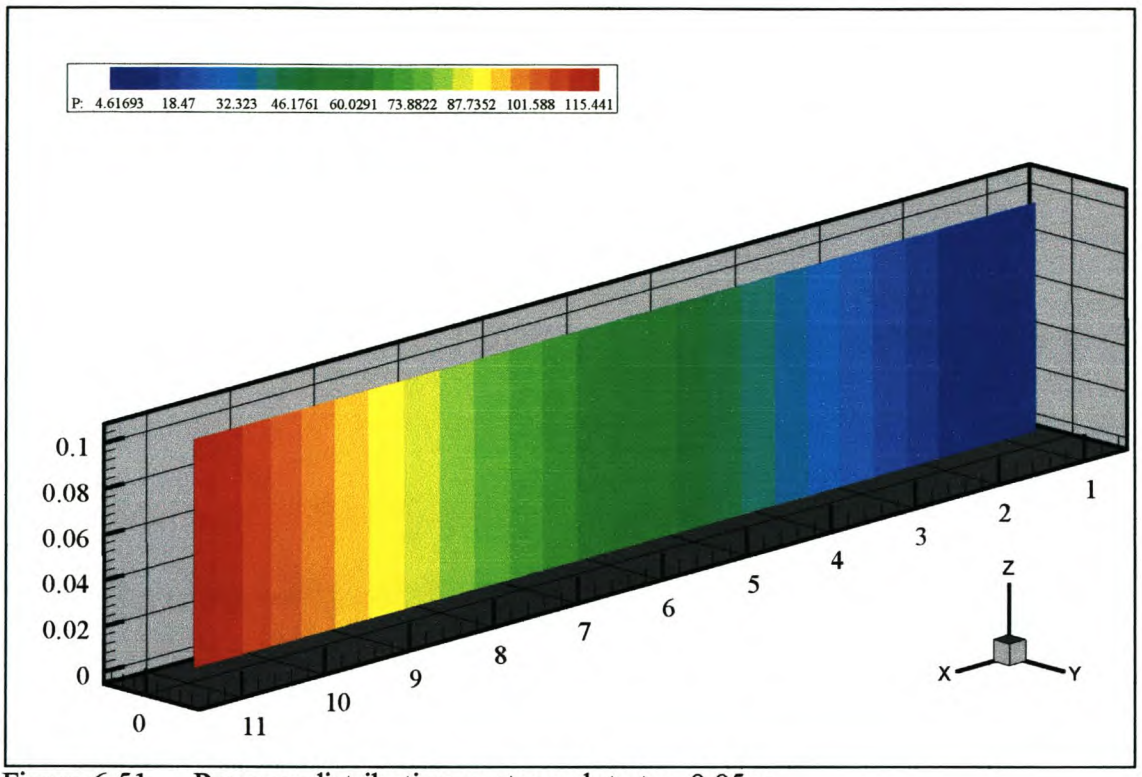

Figure 6.51. Pressure distribution contour plot at y=0.05m

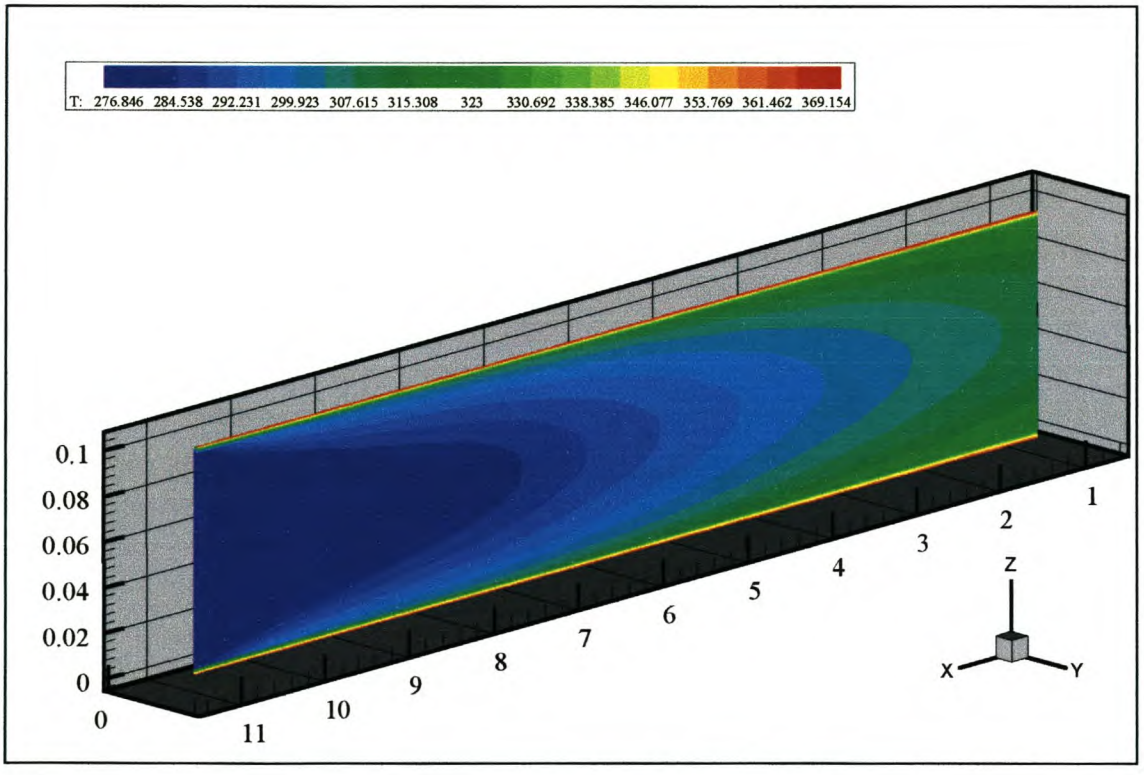

Figure 6.52. Temperature distribution contour plot at y=0.05m

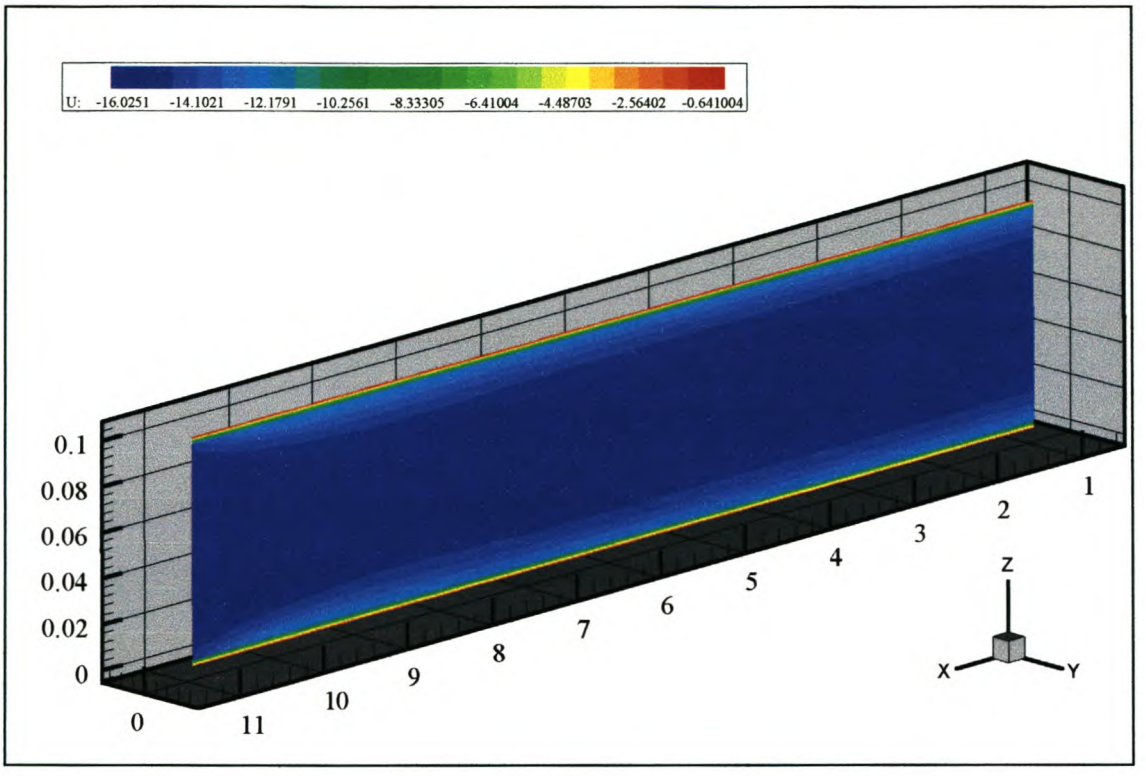

Figure 6.53. U-Velocity contour plot at y=0.05m

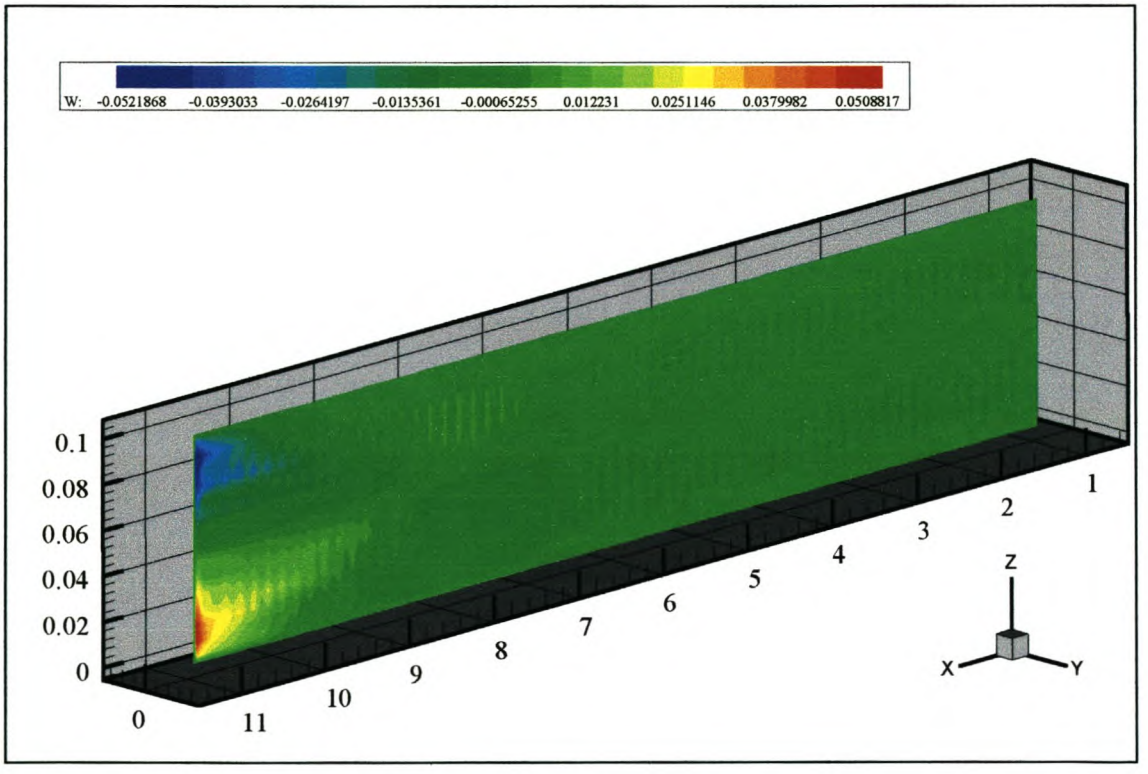

Figure 6.54. W-Velocity contour plot at y=0.05m

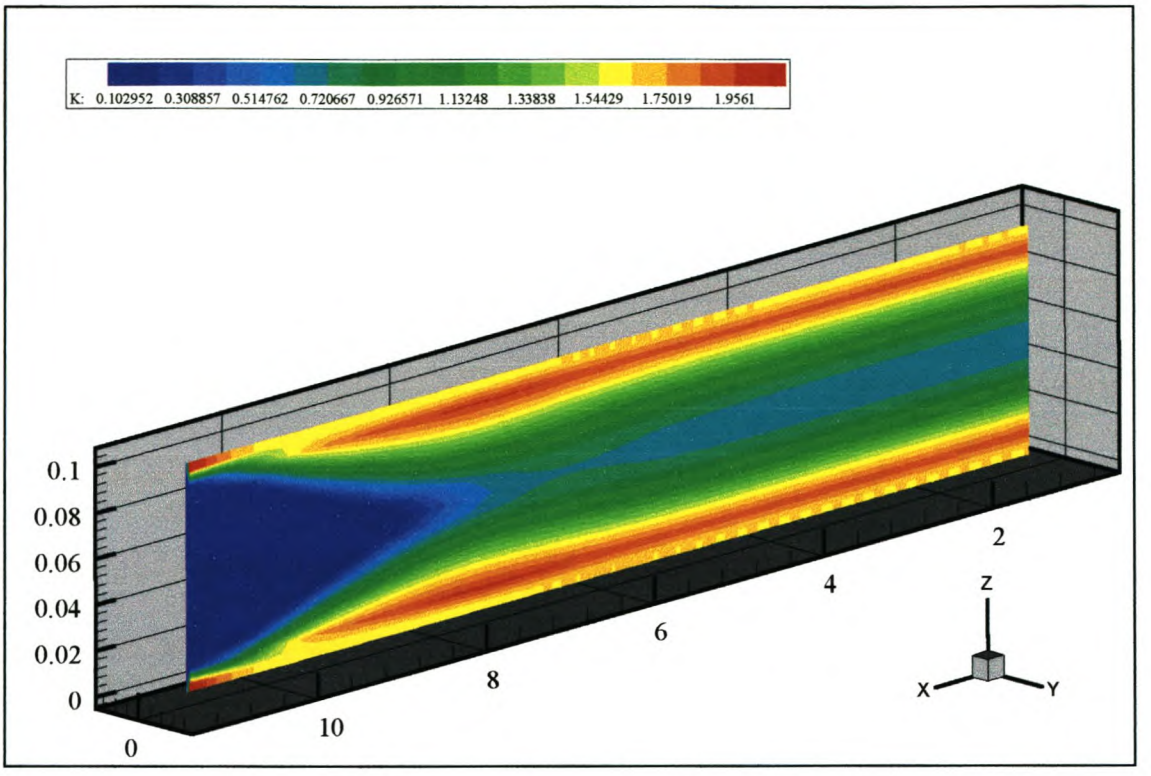

Figure 6.55. Turbulent kinetic energy contour plot at y=0.05m

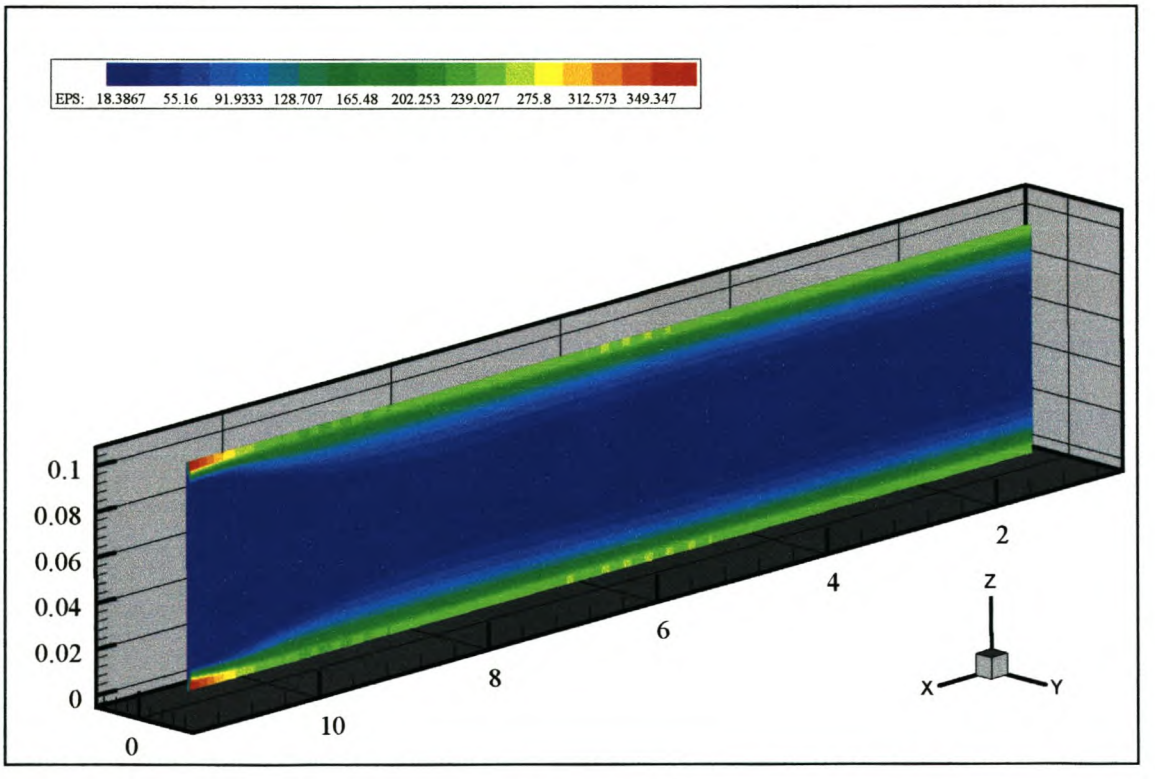

Figure 6.56. Dissipation rate contour plot at y=0.05m

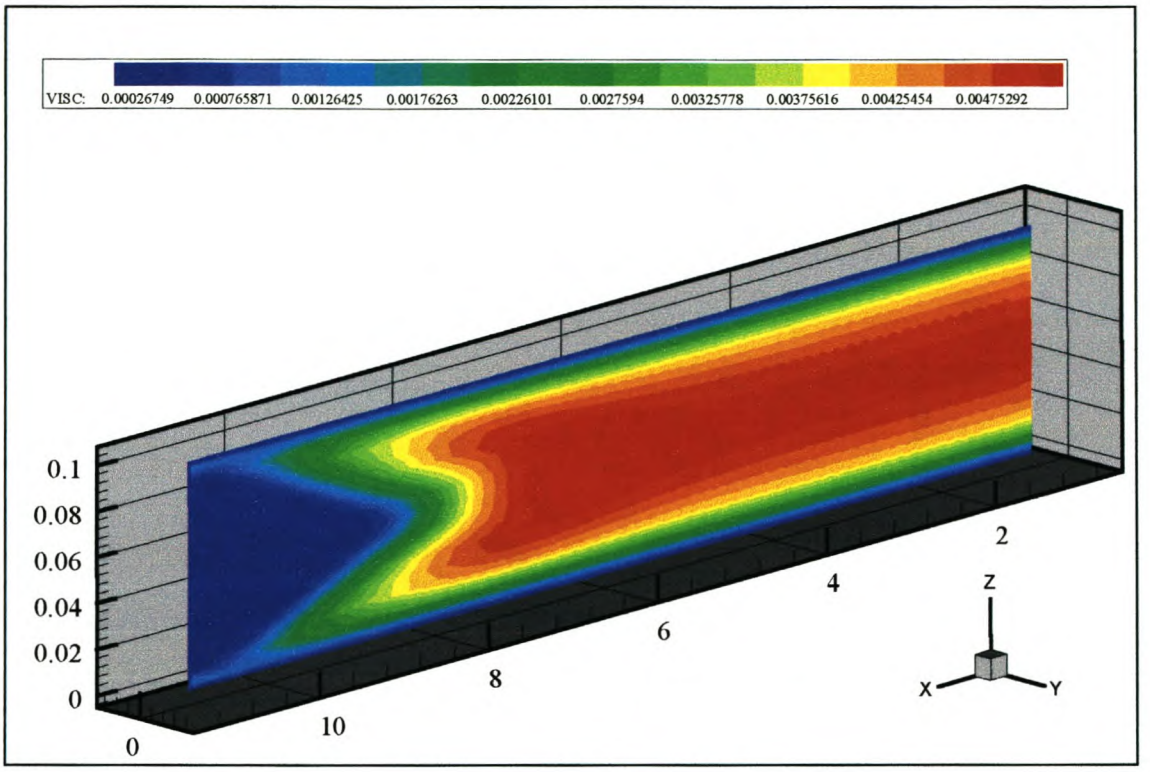

Figure 6.57. Effective viscosity contour plot at y=0.05m

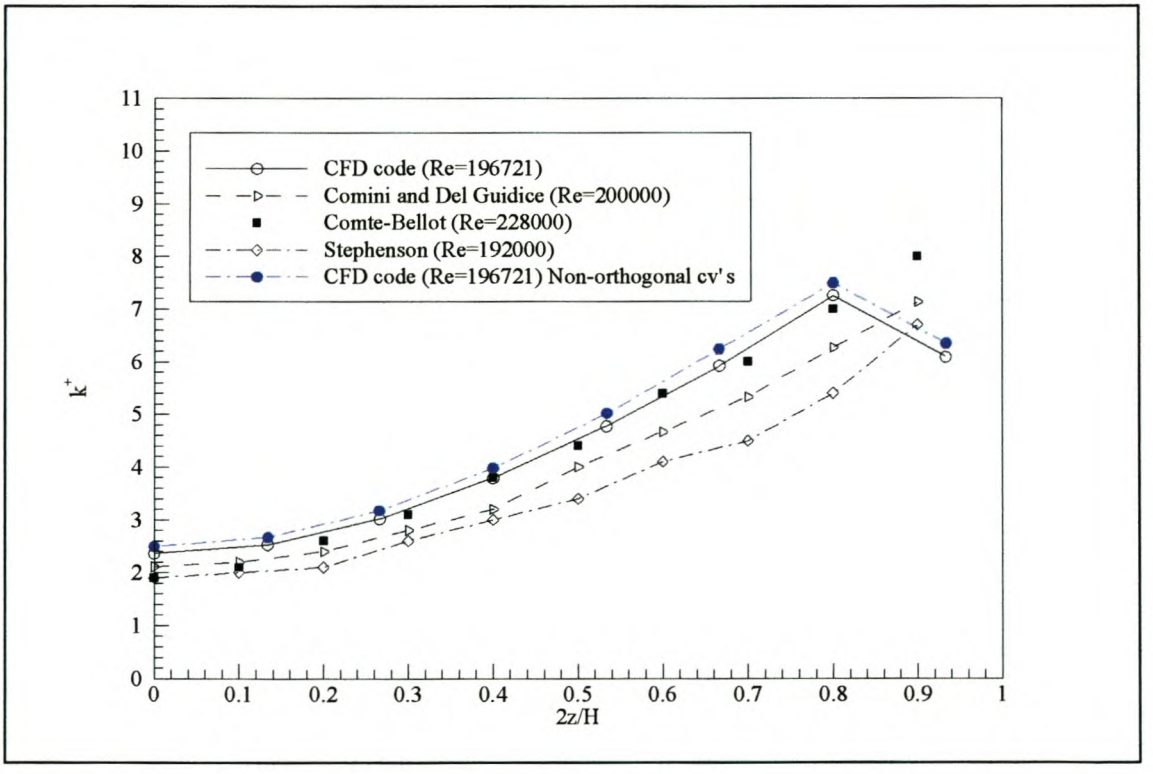

Figure 6.58. Dimensionless outlet turbulent kinetic energy distribution

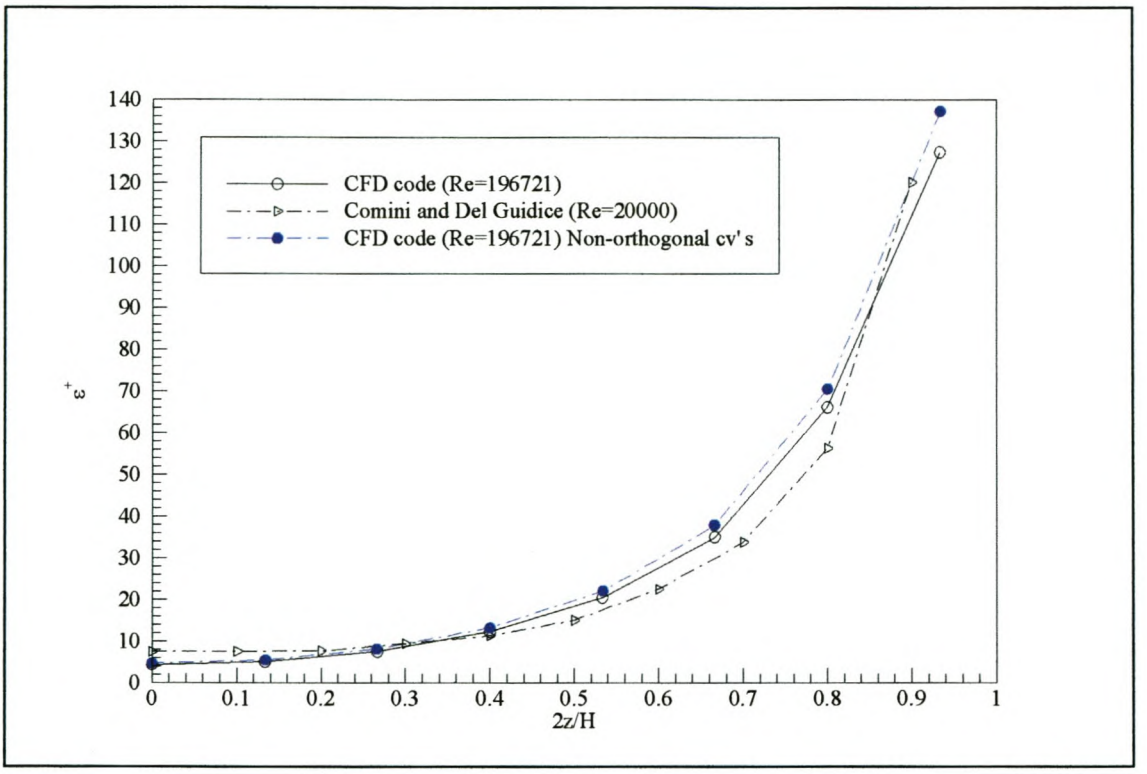

Figure 6.59. Dimensionless outlet dissipation rate distribution

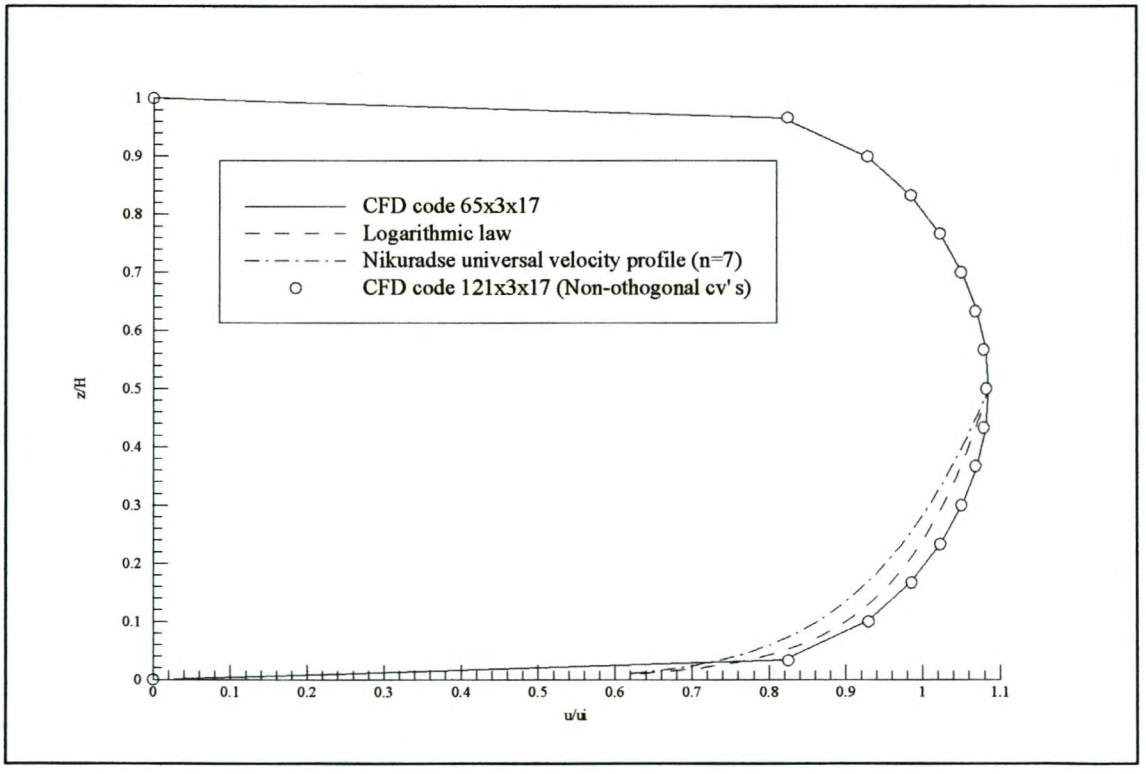

Figure 6.60. Normalised outlet axial velocity (u/u_i) distribution

6.5.3 Verification of results

From the code results presented in chapter 6.5.2 it is evident that the flow field results are similar to the results as found for the similar test case but employing orthogonal control volumes. The friction factor distribution along the length of the plates is shown in figure 6.60 for this non-orthogonal test case. The results compares favourably to the values for Re=196721 for the orthogonal control volumes.

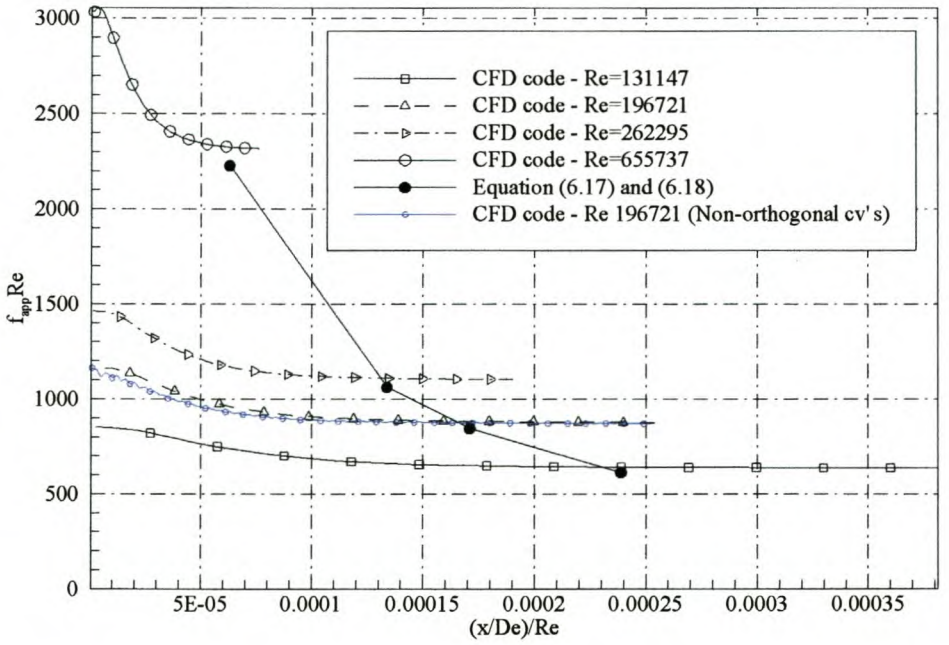

Figure 6.61 Friction factor distribution along the length of the plates. Comparison between results for Re=196721 for orthogonal and non-orthogonal control volumes.

For the purpose of the present study it was therefore accepted that the code formulation for non-orthogonal control volumes generates accurate results for friction factors and pressure drop for turbulent flows. No Reynolds numbers other than Re=196721 were evaluated.

The heat transfer characteristics are accurately predicted for the non-orthogonal control volume geometry as shown in figure 6.61. Again the results of the non-orthogonal test case

are compared to the earlier results from the orthogonal control volumes as presented and discussed in section 6.3.3.

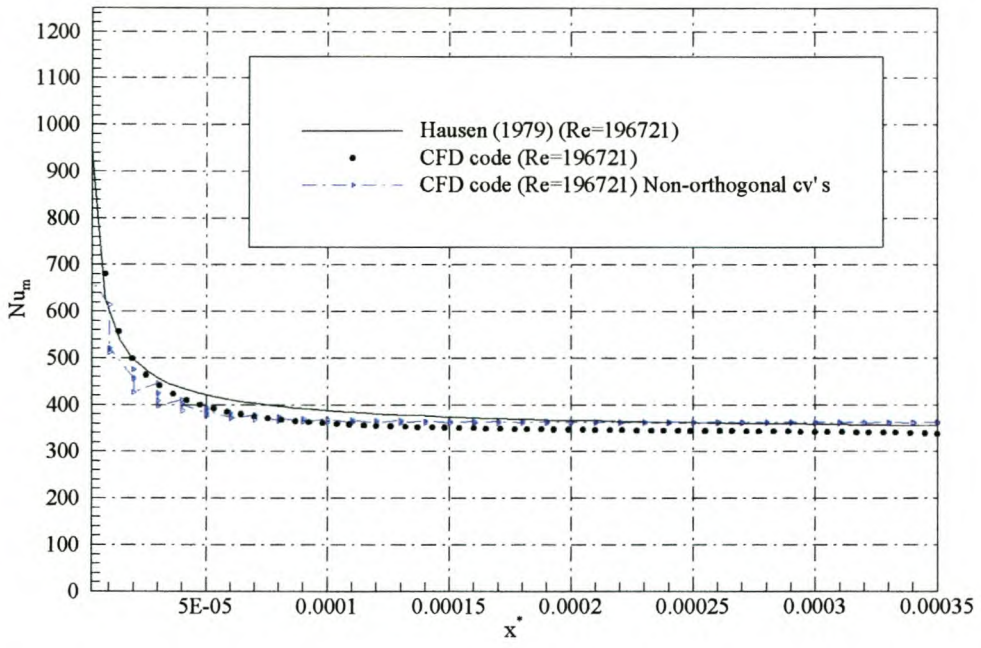

Figure 6.62 Nusselt number comparison for Re=196721 and non-orthogonal control volumes.

Figure 6.62 does indicate the presence of temperature oscillations near the entrance of the plates. This is due to the distorted control volumes in the region where the flow develops and would be eliminated by refining the grids in that area. However, these local entrance inaccuracies do not influence the final fully developed results downstream.

The above results indicate that the non-orthogonal control volume formulation as implemented in this study ensures accurate results and shows excellent agreement with results from similar but orthogonal test cases. It is therefore accepted that the formulation generates accurate results for the radial parallel plate geometry presented earlier. In these radial parallel plate problems non-orthogonal control volumes are generated in the radial direction since it is generated in a general global Cartesian coordinate frame and not in polar coordinates.

7. SOLAR CHIMNEY COLLECTOR

7.1 Introduction

The solar chimney power generating concept and principles were briefly discussed in chapter 2. As mentioned, one of the main components of a solar chimney plant is the solar collector. In general, the term solar collector defines a special kind of heat exchanger which transforms solar radiation or solar energy into heat, Duffie and Beckman (1991). The collector of the solar chimney plant is essentially a circular flat plate collector although the transparent roof cover may be raised towards the center of the collector to limit friction losses due to accelerating flows, as well as limiting separation of flow at the collector and chimney transition region, Schlaich (1995). Figure 7.1 illustrates the solar collector of a solar chimney power plant.

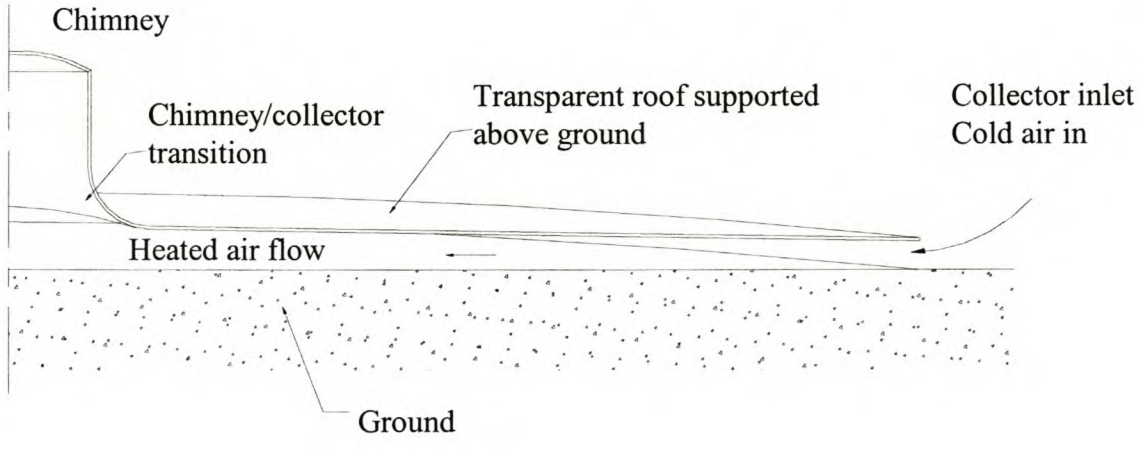

Figure 7.1 The solar chimney and collector

Air is heated inside the collector by the greenhouse effect and is subsequently drawn from the collector perimeter towards the centre. At the base of the chimney a turbine uses this mass flow of hot air exiting the collector, to generate electricity. Therefore, the collector initiates,

maintains and heats the mass flow of air by receiving or collecting solar energy. Due to various heat losses, not all of the solar radiation received, is available to heat the air. These energy losses include, among others, radiation losses from scattering of radiation as it passes through the atmosphere, losses from reflection of radiation from the glass roof and from the ground, conduction losses in the ground and roof, and convection losses from the top of the roof to the atmosphere. The radiation that is ultimately absorbed by the ground increases the soil temperature which in turns transfers heat to the air by means of convection. Considering an energy balance across the collector, the efficiency of the collector may be defined as the energy absorbed by the air divided by the total solar energy received i.e.

$$\eta = \frac{Q_{air}}{Q_{solar}} = \frac{\dot{m}C_p\left(T_{out} - T_{in}\right)}{GA_{coll}} \qquad (7.1)$$

where G may be the total available solar energy received by the collector. A_{coll} is the surface area of the collector, $\dot{m}$ denotes the mass flow rate of air through the collector and T_{out} and T_{in} are the bulk fluid temperatures at the outlet and inlet respectively. Schlaich (1995) and Haaf (1984) defines similar solar collector efficiencies.

As shown by Gannon and Von Backström (1999) their exists a strong coupling between the power output of the plant, the temperature rise in the collector and the mass flow rate of air through the plant. These parameters also influence the operating range of the turbine. Thus, the accurate prediction of the collector efficiency and the characteristics and properties of the air flow through the collector is an essential part of the solar chimney power plant feasibility study and design of an efficient solar chimney power plant and operating conditions. Some of the more important characteristics that need attention include the heat transfer from the heated ground to the air stream, the conduction of absorbed solar energy in the soil and subsequently the inherent thermal inertia of the system and the friction losses occurring in the flow. The present numerical evaluation of the solar collector intends to evaluate the resultant average air temperature rise established by the collector as well as to provide the two dimensional temperature, velocity and pressure profiles of the flow field within the collector.

The present study applies the numerical code to the solar collector as found in the Manzanares solar chimney pilot plant and for which operational principles and experimental data is

available Haaf (1984) and Haaf et al. (1983). The model assumes a flat plate circular air collector, similar to the test cases presented in chapter 6 and as shown in figure 7.2. The models consists of three regions namely the glass roof, the region of air flow and the soil region. The boundary conditions and fluid properties applicable to the model are also shown in figure 7.2. The flow through the collector is assumed to be incompressible and dry.

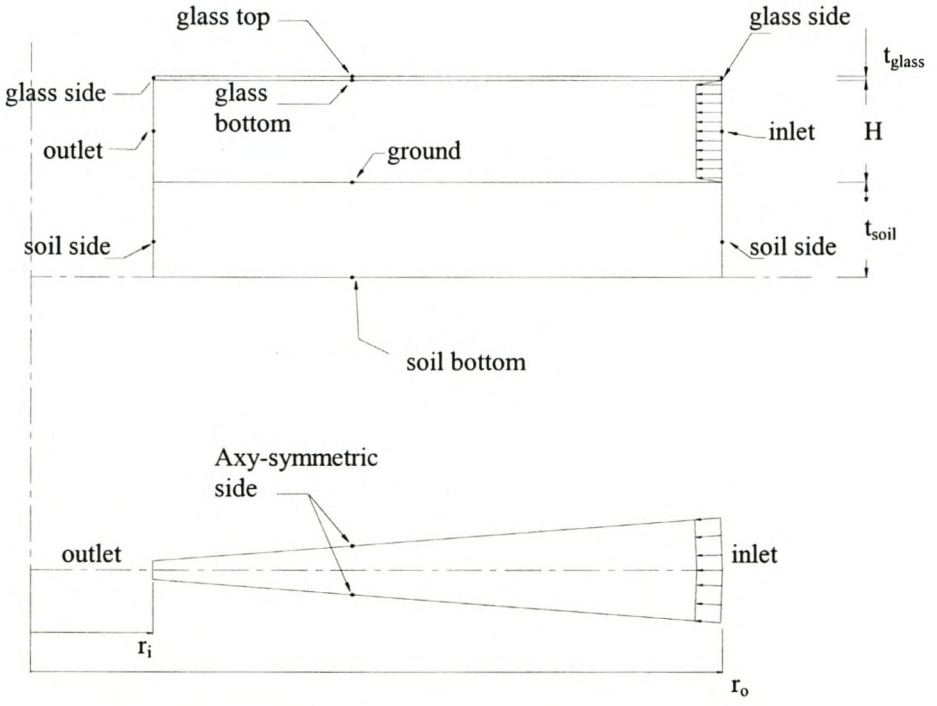

Figure 7.2. The solar collector model

The mass, momentum and energy conservation equations are solved for the air flow region while only the energy equation is applied to the glass and ground regions.

7.2 The Manzanares Solar Collector

7.2.1 The model

The model representing the solar collector for the pilot plant built in Manzanares has an outside diameter of d_o=245m and a chimney diameter of d_{chim}=10m. A collector inside diameter of d_i=30m. and a wedge included angle of θ=0.01 radians was used in this model. The transparent collector roof is raised H=2m above the ground. Typical operating values as measured at the plant as extracted from Haaf (1984) and Haaf et al (1983) were employed as boundary conditions for the model and the resultant numerical prediction of the temperature rise across the collector compared to these measured values. For 10:00am, a chimney outlet velocity of V=7.01m.s^{-1} was measured. The ambient temperature was T_a=20°C and the surface temperature of the ground was T_w=56°. The measured temperature rise in the collector was ΔT=14.59°C. The measured surface temperatures given by Haaf (1994), are, for the sake of simplicity, assumed constant throughout the collector. A solar radiation source term at the soil and fluid interface was excluded in this model since the surface temperatures for the soil is available and assumed constant. For simplicity, a zero temperature gradient roof/air boundary was used. The Reynolds number for these flow conditions, based on the average inlet velocity and an effective diameter of twice the roof height is Re=93718. The bottom soil was assumed to be rough and with an equivalent sand roughness height of k_s=5%H=0.1m. The glass surface was assumed to be smooth.

Initially, the above mentioned test case was evaluated on three grid configurations namely 65x7x23 grid points, 95x7x33 grid points and 165x7x23 grid points. This ensured that a grid independent solution was reached. The grid was refined towards the walls by employing a series expansion with expansion factor of 0.9. This ensured that the y^+ terms remain within the limits set for the turbulence model from the inlet to the outlet of the collector. The grid was also locally refined at the inlet and outlet. The inlet turbulent intensity value used was i_k=0.01.

The number of iterations required to decrease the normalised mass residuals below 0.2 on the finest grid is approximately 2000 with under-relaxation factors as per Table 7.1. The

convergence history is shown in figure 7.3. The computational speed was 0.0042 seconds/iteration/grid point.

Table 7.1 Solution parameters for the Manzanares solar collector model

Relaxation factors					
α_p	α_V	α_k	α_ε	α_T	γ
0.2	0.8	0.2	0.2	0.8	0.9

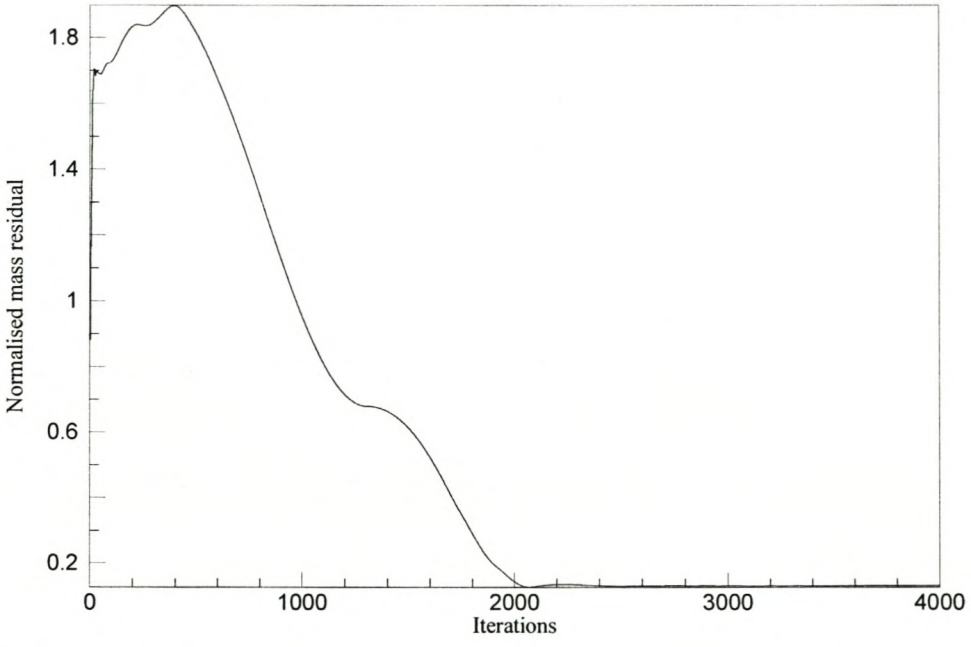

Figure 7.3. Manzanares model convergence history for 165x7x33 grid

7.2.2 Code results for the Manzanares collector

Figures (7.4) to (7.16) shows results from the CFD code solution for typical flow conditions and fluid properties as discussed.

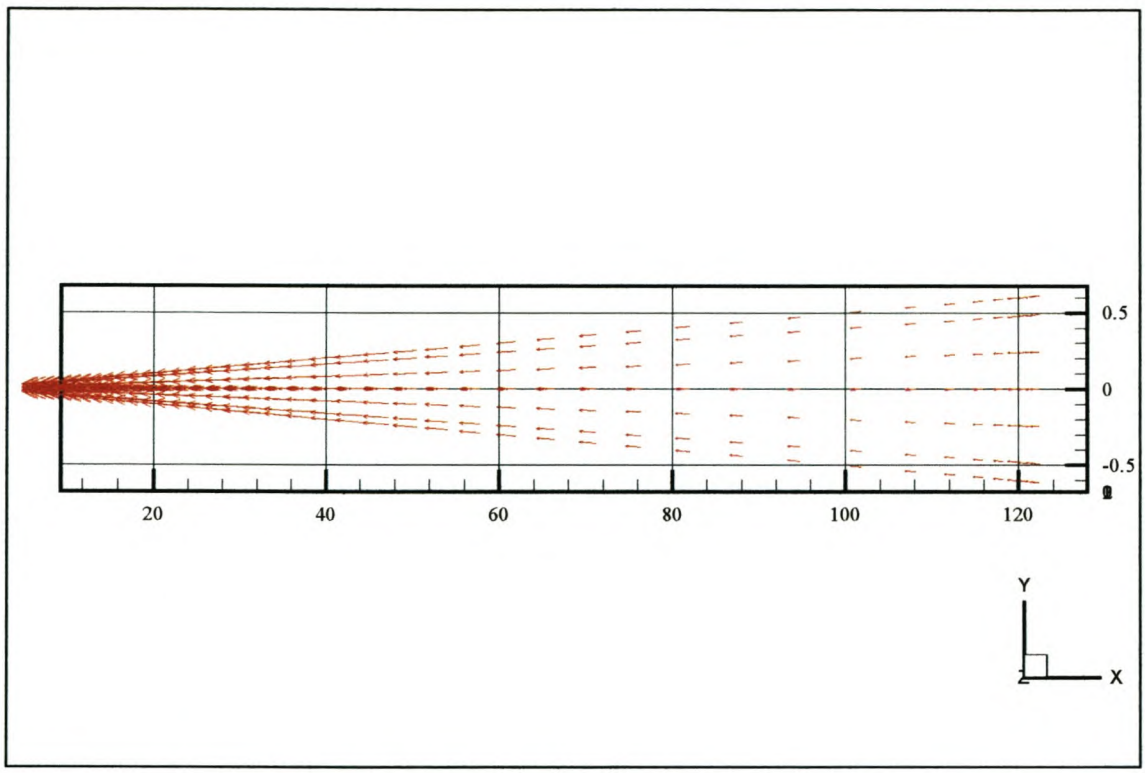

Figure 7.6. Velocity vector plot on plane z=1.00m

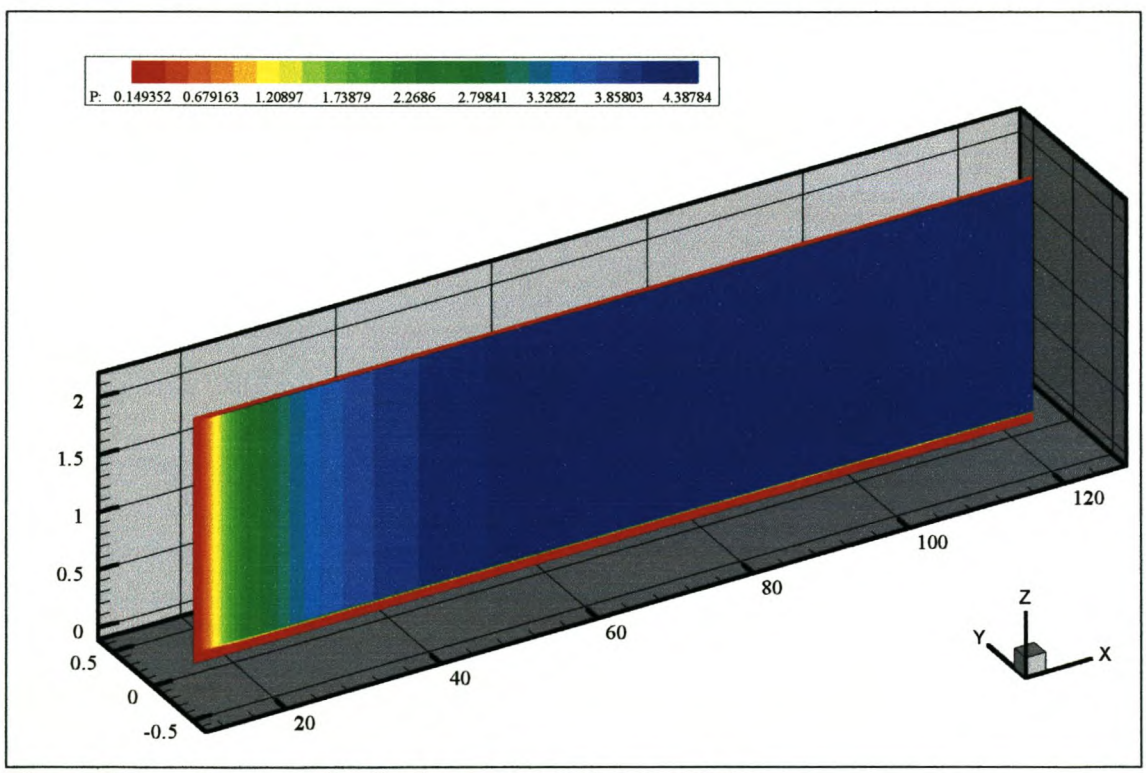

Figure 7.7. Pressure distribution contour plot at y=0.0m

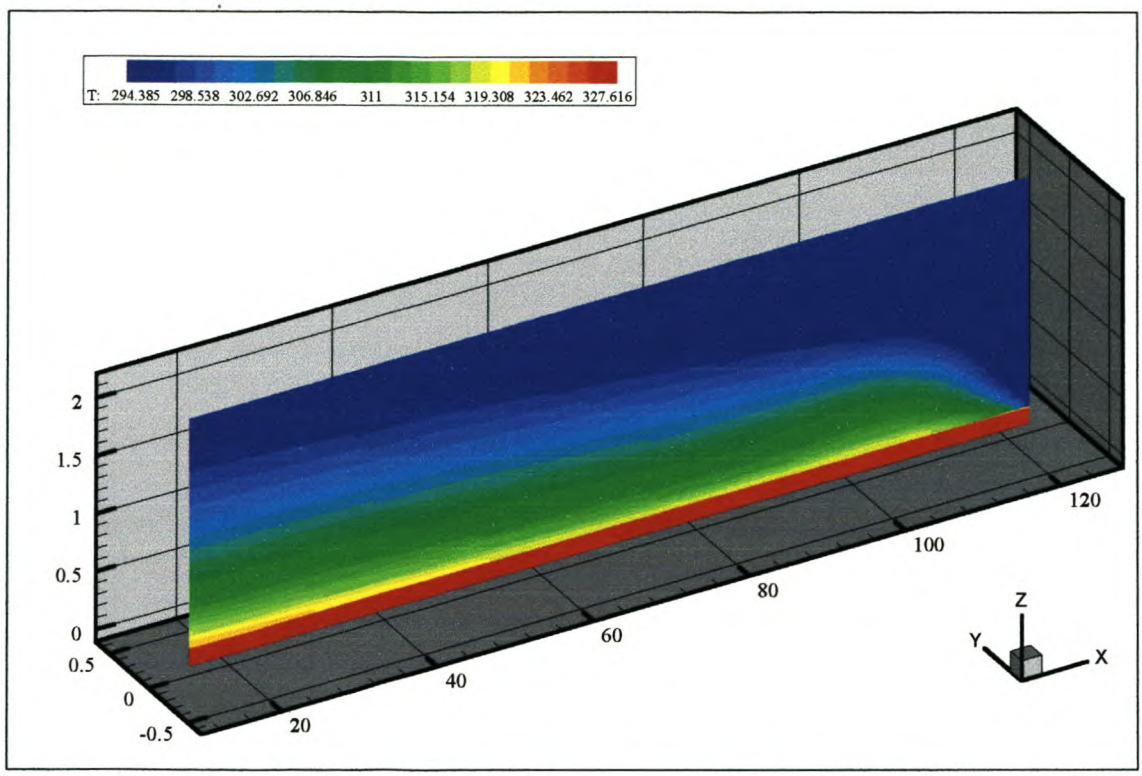

Figure 7.8. Temperature distribution contour plot at y=0.0m

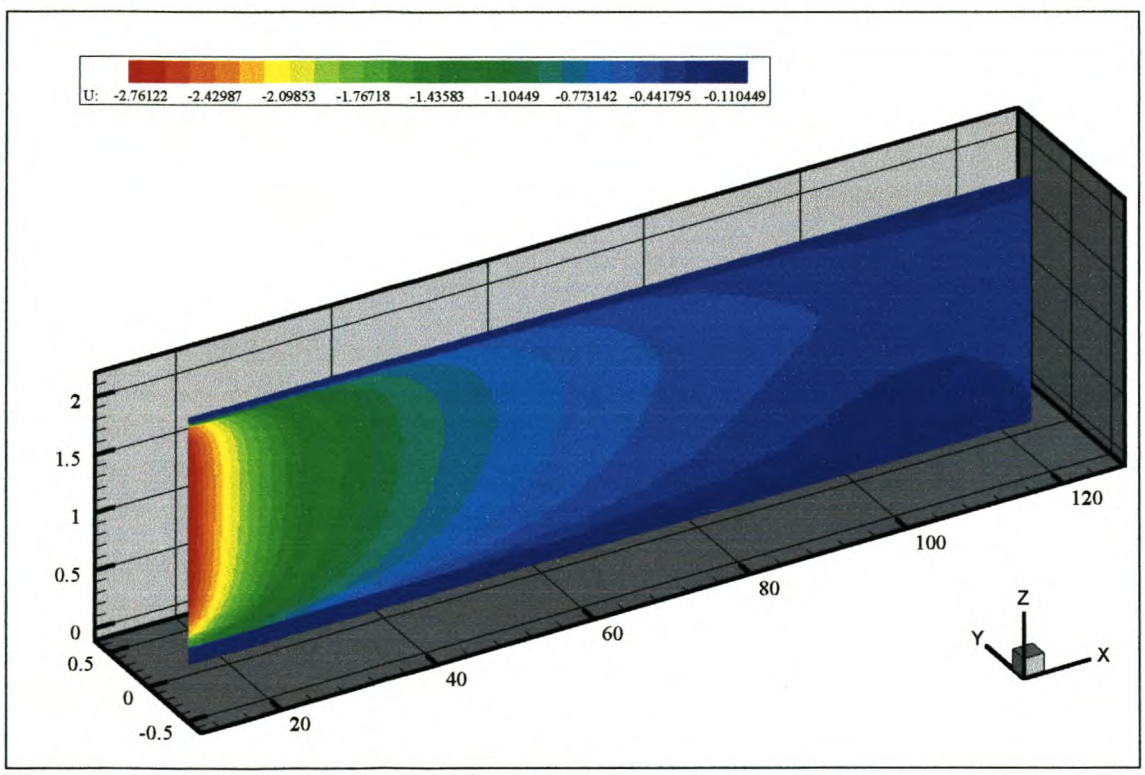

Figure 7.9. U-Velocity contour plot at y=0.0m

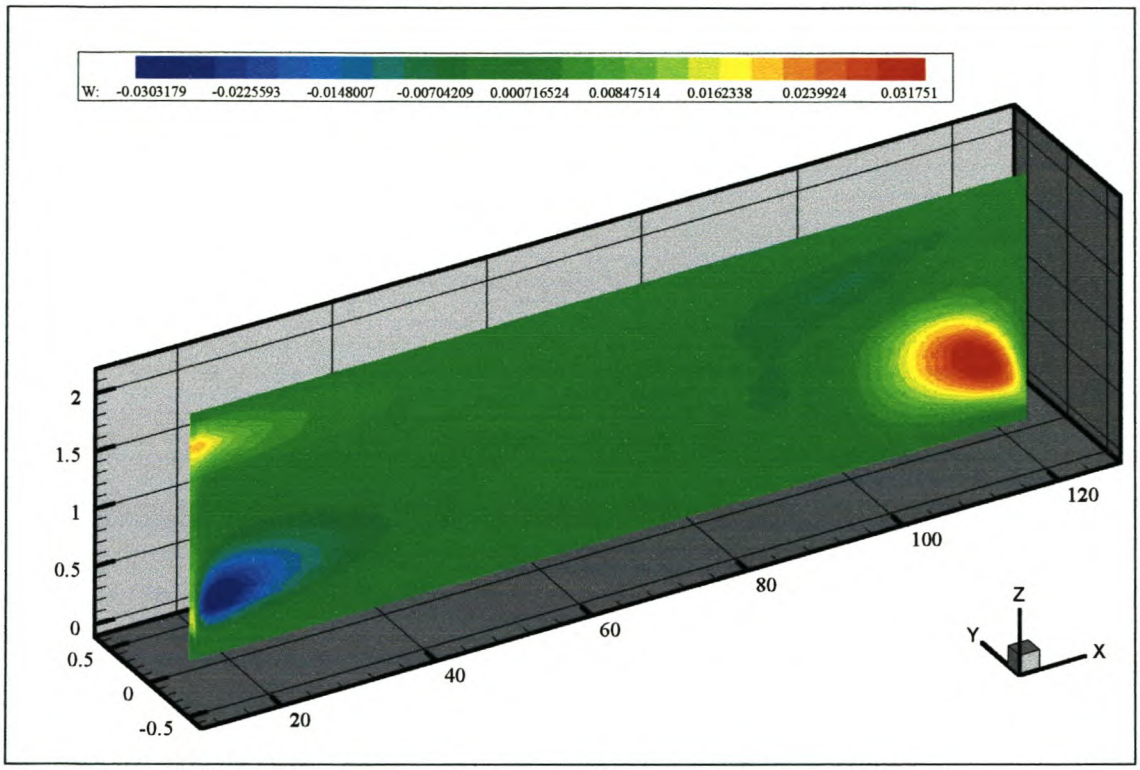

Figure 7.10. W-Velocity contour plot at y=0.0m

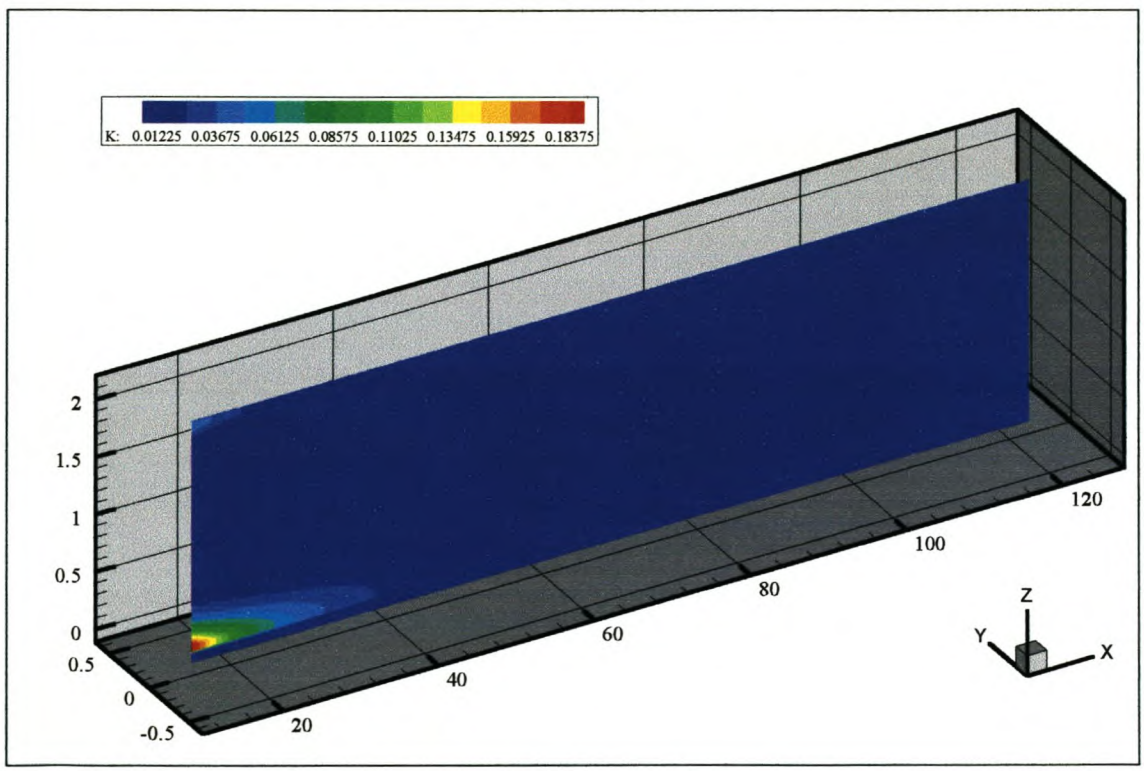

Figure 7.11. Turbulent kinetic energy contours plot at y=0.0m

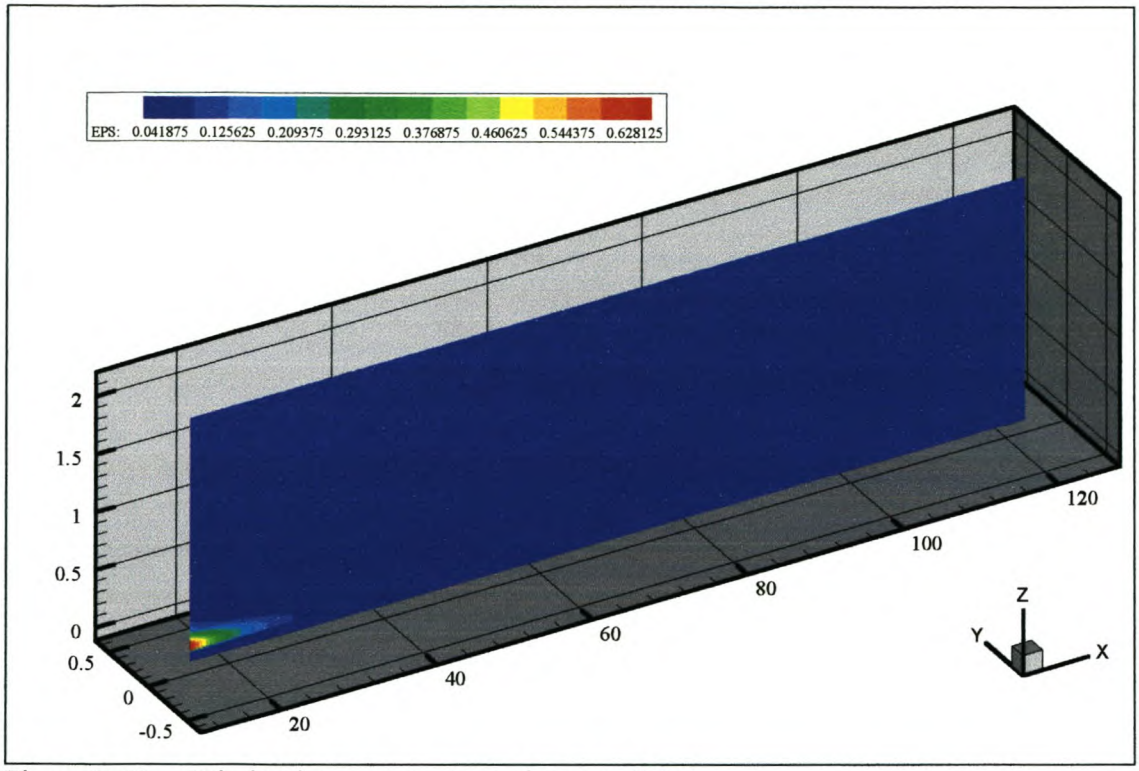

Figure 7.12. Dissipation rate contour plot at y=0.0m

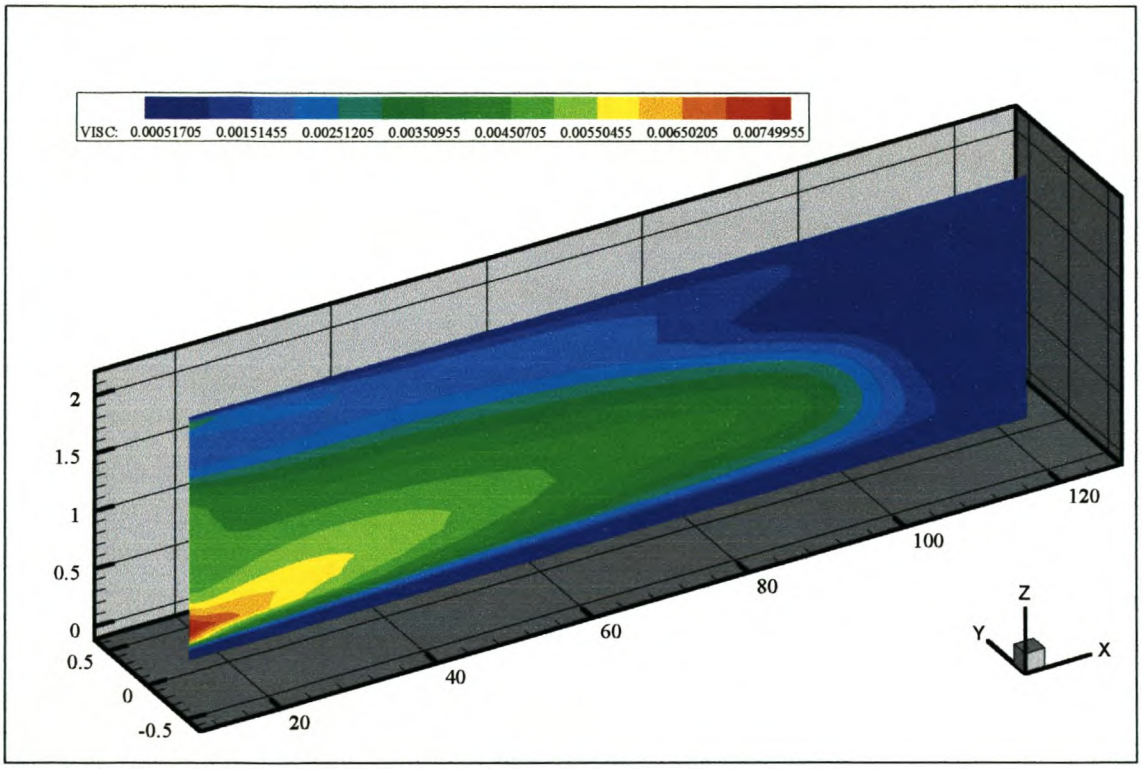

Figure 7.13. Effective viscosity contour plot at y=0.0m

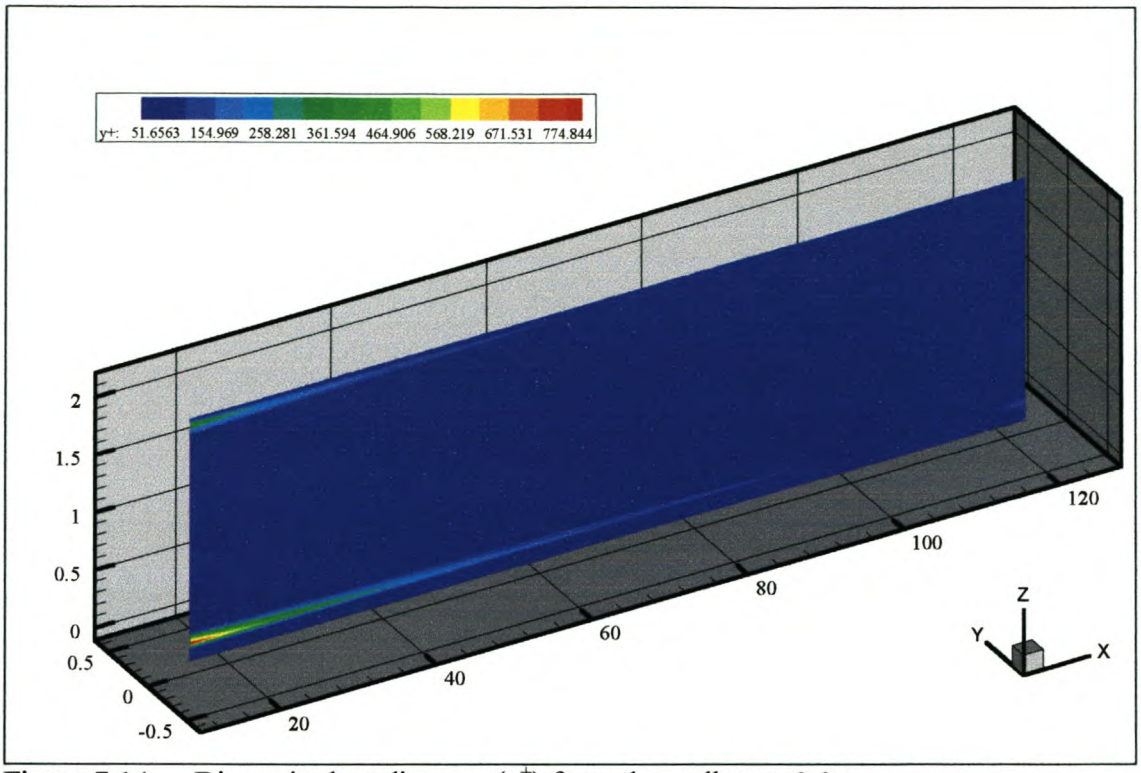

Figure 7.14. Dimensionless distance (y^+) from the wall at y=0.0m

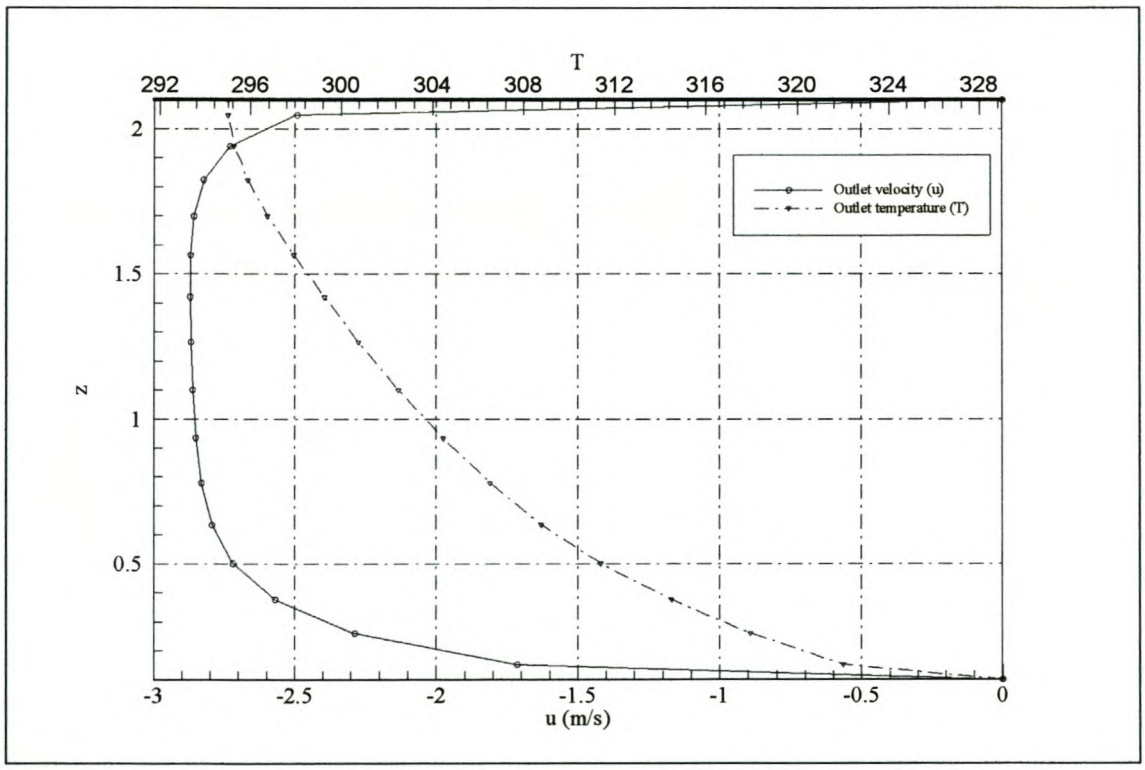

Figure 7.15. Outlet axial velocity (u) and temperature (T) distribution

7.2.3 Discussion of results

The flow of air through the collector is expected to behave similar to the air flow through the radial parallel plates as modeled and presented in chapter 6. We may also compare the frictional pressure drop and local heat transfer coefficients predicted by the present code with results found by using the equations derived by Kröger (1999). Figure 7.17 shows the local heat transfer coefficient at the rough ground surface as predicted by the code and compared to values found from equations (6.50) and (6.51). Again the code prediction in the entrance region compares well with results found from equations (6.50) and (6.51).

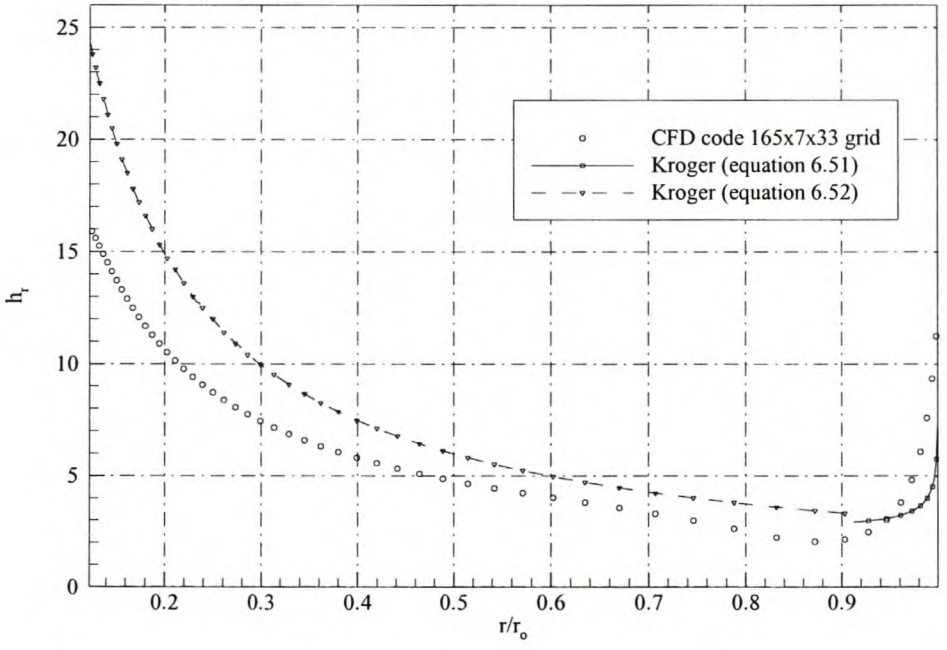

Figure 7.16. Rough ground surface local heat transfer coefficient prediction

Figure 7.16 indicates that the results from the code prediction of the heat transfer coefficient corresponds reasonably compared to values calculated by using equations (6.51) and (6.52). However, towards the outlet the difference between the code and the analytical results is as high as 30%. Presently these results only indicate that both the present code as well as the analytical equations from Kröger (1998), for radial developing and fully developed flows, predicts similar trends in the thermal behaviour of the air flow within the collector.

The code prediction of the bulk fluid temperature rise through the collector is shown in figure 7.17. The total bulk fluid temperature rise of 10.8K is lower than the value of 14.5K given by Haaf (1984). This may be attributed to various modeling assumptions and simplifications.

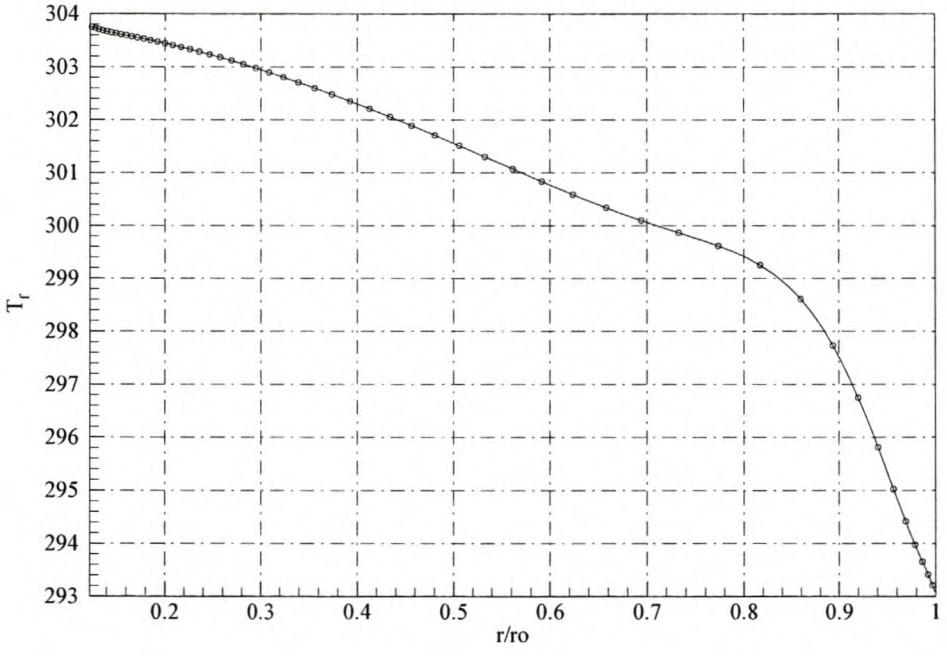

Figure 7.17. Code prediction of bulk air temperature rise through the collector.

The assumptions that may lead to the prediction of lower air temperatures are the exclusion of a radiative heat source in the glass roof and ground, the assumption that the glass roof is smooth and the unavailability of actual roughness parameters for the ground. It is also not clear from experimental data where the average temperature rise in the collector is measured and how the average temperature is determined.

Figure 7.18 shows the code prediction of the frictional pressure loss coefficient within the Manzanares solar air collector.

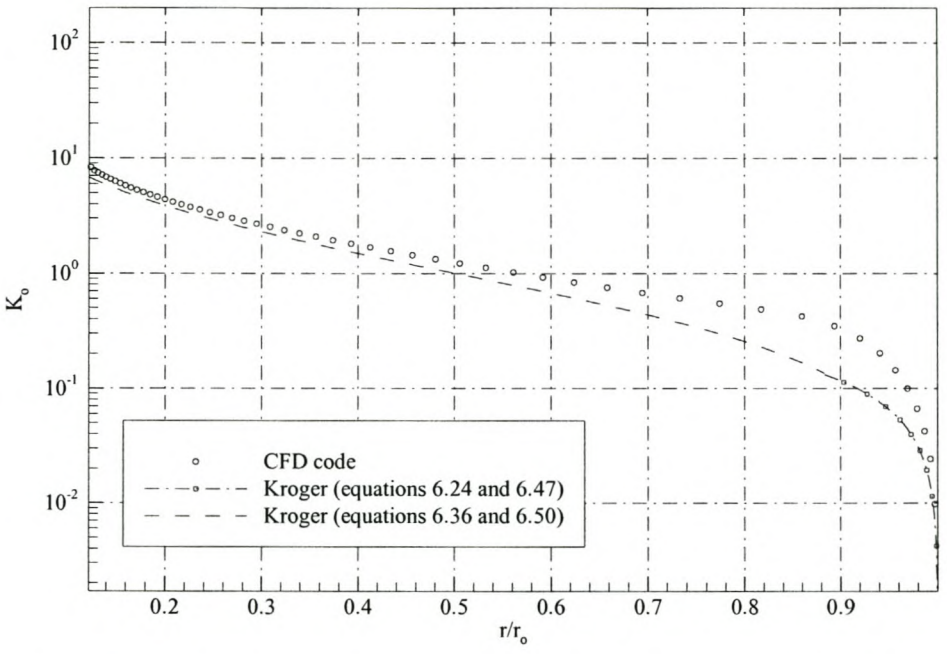

Figure 7.18. Frictional pressure loss coefficient for Manzanares solar collector

Since the glass roof is assumed smooth and the ground surface treated as rough, the frictional pressure loss coefficient was found from the average of the values found from equations (6.24) and (6.46) for the developing flow region and from the average of the values found from equations (6.36) and (6.49) for the fully developed region. Figure 7.18 indicates that the present code prediction of the pressure loss coefficient compares well with the values calculated as mentioned above.

8. COMPUTER PROGRAMS

8.1 Introduction

The code generated to solve the flow and heat transfer problems consists of four individual programs, each running separately but in succession. Similar modules as proposed by Harms (1995) are adopted. The FORTRAN 77 programming software was used on the DEC VAX system of the University of Stellenbosch. The programs produced are TOWER.FOR, GEOCALC.FOR, INIT.FOR and MAIN.FOR. This chapter describes the structure and primary subroutines contained in each. The information calculated in each program is stored in data files which is then read by the other programs. This saves processing time since, for example, one does not recalculate the grid geometry and geometrical parameters each time flow parameters are changed. These geometries are constant for a given computational domain or geometry and do not require amendment. Effectively, in order to calculate the flow field in any arbitrary domain one only needs to generate the control volume corner coordinates. Once this is achieved all the subsequent computations such as calculation of geometrical vectors and the solution of the field properties are processed automatically, except for the changing of under-relaxation parameters and boundary conditions. Simply put, if it becomes necessary to add a different more advanced grid generation package to the existing code, one simply replace program TOWER.FOR and ensures that the control volume central node and corner coordinates are stored in the same format as required by the subsequent programs.

The main geometrical and solver parameters are also stored in a text file, INPUT.DAT, from which each program reads the relevant information to either generate the geometry or to solve the flow field.

8.2 TOWER.FOR

This program is responsible for grid generation. The structure of the program is shown in figure 8.1.

The program TOWER.FOR reads information from INPUT.DAT in subroutine INPUTD, such as which geometry needs to be calculated and the number of nodes required in three dimensional space. The available geometries include a radial flat plate collector and flat parallel plates. Other geometries may be programmed or alternatively a more advanced grid generating program may be employed instead.

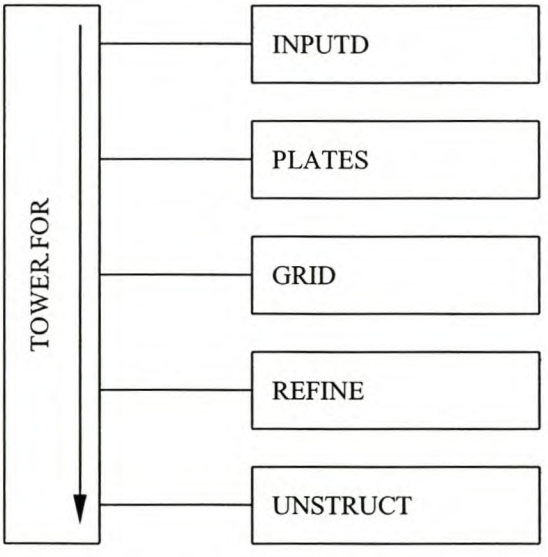

Figure 8.1. TOWER.FOR flow chart

Subroutine PLATES generates the flat parallel plates for the verification problems and subroutine GRID generates the radial parallel plates for the solar collector test cases. Each of the grid generators calculates the control volume corner coordinates and central node coordinates based on the geometry parameters and number of nodes required and as read in INPUTD. Subroutine REFINE applies local grid refinement, if required, by means of either a geometrical series or by dividing a line describing the length of a boundary into unevenly spaced or concentrated segments. The length of these segments may found from fitting a third order polynomial through three coordinates and two gradients at the first and last

coordinates. All coordinates are generated by sweeping the three dimensional domain (x,y,z) and subsequently storing the central node coordinates and control volume corner coordinates in structured three and four dimensional arrays, array(j,k,i) and array(n,j,k,i) respectively, where n defines a face number from one to six.

Subroutine UNSTRUCT sweeps through the three-dimensional arrays, assigns unstructured node numbers to each control volume central node and stores all information in unstructured one or two-dimensional arrays. Thus, all geometrical information may be retrieved by only sweeping from node 1 to the node N, the total number of nodes in the domain. The information is saved in a data file for subsequent retrieval.

8.3 GEOCALC.FOR

This program reads the control volume central node and corner coordinates generated and stored in program TOWER.FOR. Figure 8.2 shows a flow chart of the structure of the subroutines of GEOCALC.FOR.

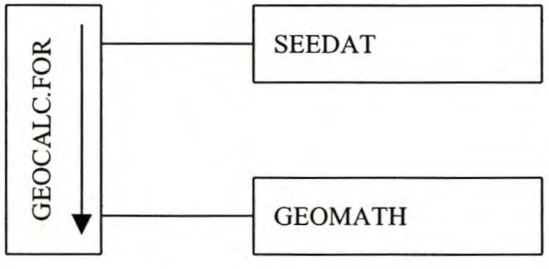

Figure 8.2. GEOCALC flow chart

Subroutine SEEDAT reads the coordinate data file generated by program TOWER.FOR. This information is used to calculate geometrical parameters such as the volume of each of the control volumes, the interfacial area vectors, interfacial interpolation factors and nodal vectors among others. These are calculated in subroutine GEOMATH. These parameters are constants and are only recalculated for different geometries. All the relevant information is stored in a data file for subsequent use by the program MAIN.FOR for the solution of the flow field.

8.4 INIT.FOR

This program initialises the flow field. It assigns the initial field flow conditions and initial properties of the fluid. The structure of the program is shown in figure 8.3.

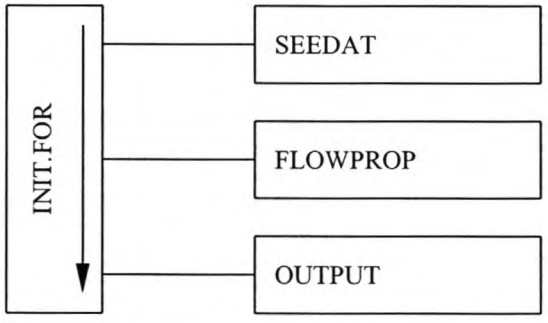

Figure 8.3 INIT.FOR flow chart

Again subroutine SEEDAT reads data files containing relevant nodal information generated by the previous programs. Subroutine FLOWPROP assigns initial values to each node such as U, V and W velocity values, temperature, density, viscosity and nodal pressure among others. Subroutine OUTPUT writes all these nodal value data to file for subsequent retrieval by program MAIN.FOR.

8.5 MAIN.FOR

This program is responsible for combining all the geometrical information and flow properties and calculates the flow field within given boundary conditions. The structure of the subroutines contained with MAIN.FOR is shown in figure 8.4

Firstly the geometrical information, initial flow conditions and flow solution parameters are retrieved from the relevant files in subroutines INPUTD and SEEDAT. This includes information such as the interfacial area vectors, nodal vectors, nodal gradient projection

factors, volumes, interpolation factors, relaxation factors, flux blending factors, number of iterations required, time step magnitude and other information.

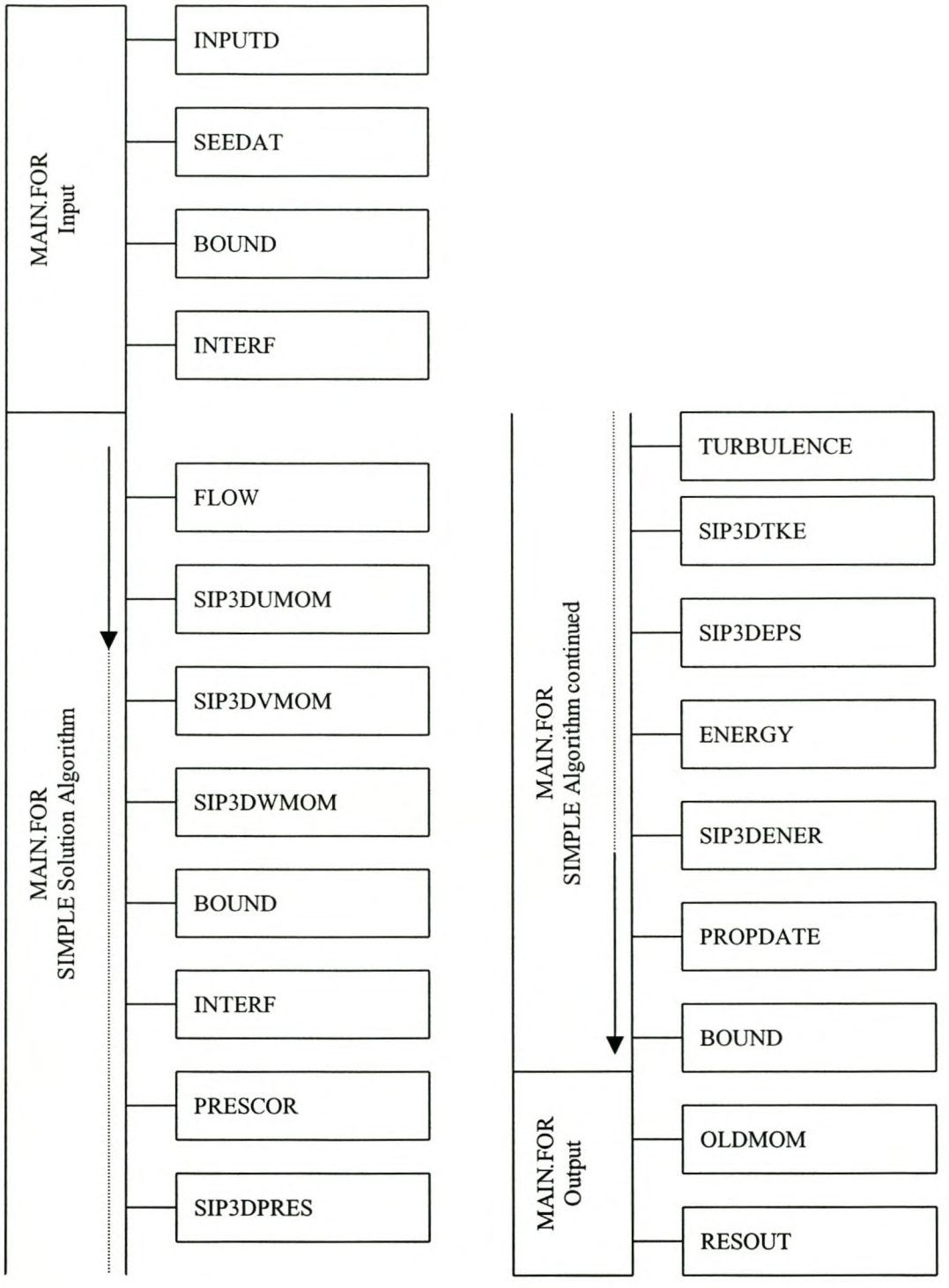

Figure 8.4. MAIN.FOR flow chart

The field is again initialised with subroutines BOUND and INTERF which calculated the initial boundary conditions and interfacial quantities required to calculate influence coefficients for the discretised governing equations.

The outer iteration of the solution algorithm is then started with subroutine FLOW, calculating the influence coefficients and source terms contained in the discretised three dimensional momentum conservation equations. The momentum conservation solution matrix is solved by means of the SIP solver in subroutines SIP3DUMOM, SIP3DVMOM and SIP3DWMOM resulting in a new velocity field.

The boundary conditions are applied in BOUND and the interfacial properties such as interfacial velocities are updated in subroutine INTERF.

The calculation of the influence coefficients and source terms required by the discretised pressure correction equation are calculated in subroutine PRESCOR. The pressure correction solution matrix is solved in SIP3DPRES after which the nodal pressure field as well as the interfacial velocity field are updated with pressure and velocity correction values.

If required, the influence coefficients and source terms present in the turbulent kinetic energy and dissipation rate equation are subsequently calculated in subroutine TURBULENCE and solved in subroutines SIP3DTKE and SIP3DEPS respectively. These values would later be used to update the effective viscosity and conductivity values.

If an energy field solution is required, the subroutine ENERGY calculates the influence coefficients and source terms required to solve a temperature field. The temperature field is subsequently solved in subroutine SIP3DENER.

The algorithm follows with subroutine PROPDATE which updates the effective viscosity and conductivity values in the case of a turbulent field solution and also, if required, recalculates fluid properties such as density from equations of state.

The boundary conditions are again applied in subroutine BOUND after which the convergence evaluation is made. If the convergence criteria are met or if the total number of iterations specified has been reached then the algorithm exits the outer loop and stores the results in data files for evaluation or restart purposes in subroutine RESOUT. If these conditions are not met, the algorithm returns to the subroutine FLOW for another outer iteration. If a transient solution is required, then once the convergence criteria are met for one time step, the algorithm exists the outer loop, writes the results to file, updates the "old" property values with the latest values in subroutine OLDMOM, resets the convergence criteria and outer loop iteration number and returns to subroutine FLOW for calculation of the filed at a new time step.

All resultant field data and residual error data are stored in the format specified by TECPLOT 7.5 for ease of evaluation and visualization.

9. CONCLUSIONS AND RECOMMENDATIONS FOR FUTURE WORK

During the course of this study a non-orthogonal three-dimensional finite volume code was established for the solution of incompressible, Newtonian, single phase fluid flows including turbulence and heat transfer effects. The discretisation of the governing equations pertaining to such fluids was formulated to complement this finite volume method in a general locally non-orthogonal coordinate frame. The flux blended interpolation scheme employed in the discretisation was found to be adequately robust.

The code generated was applied to simple test cases to evaluate the solution of laminar and turbulent thermo-flow problems. The code was also applied to calculate the thermo-flow field behaviour of the flow through a solar chimney collector. Although non-orthogonal contributions remained active during the evaluation of the code, they still requires extensive evaluation against benchmark problems and for flows in complex geometries where more severe control volume distortions are present.

The Rhie and Chow interface velocity interpolation method for a non-staggered grid arrangement was included in the discretisation and incorporated into the code. It was found that this greatly reduces the occurrence of pressure oscillations in the flow field. However, the limitations of the method still requires investigation and evaluation.

A strongly implicit solution procedure (SIP) was evaluated and incorporated in a SIMPLE algorithm. This procedure was found to be highly efficient for inner iterations but that problems in large computational domains and specifically ones with high aspect ratios still require many outer iterations. The addition of a multi-grid solution method should be investigated and incorporated into the existing implicit procedure to harness the full speed-up capabilities associated with these methods. Another solution algorithm such as SIMPLEC should be also be incorporated into the code.

The FORTRAN 77 code should be modified to run on FORTRAN 90 and the user interface changed to one operating on WINDOWS. It is suggested that the main code remains an executable FORTRAN code but these executables should be incorporated in a C++ or Delphi

program to utilise its more enhanced user interface capabilities. Typically the existing code could be upgraded to operate with software such as Pro-Fortran 6.0 of Absoft which can automatically build dynamic link libraries compatible with Delphi and Borland C++ programming software. The flow visualisation software TECPLOT 7.5 was employed. The use of this software should be extended by employing its macro capabilities in conjunction with the user interface considerations mentioned above.

All the additions and modifications proposed above would greatly increase the code efficiency to evaluate the flow phenomena present within the large scale solar collector. An increase in the calculation speed of the code would also enable the prediction of the transient flow phenomena such as the effects of thermal inertia on the collector efficiency. The addition of another turbulence model should also be evaluated for its applicability to the solar collector model. The code results shows a lack of penetration of heat into the free stream for the larger radial collector. This is a specific problem that requires clarification and other turbulence models should be investigated that may accurately predict turbulence quantities for accelerating flows.

APPENDIX A

FINITE VOLUME DISCRETIZATION OF MOMENTUM CONSERVATION EQUATIONS

When integrating the general orthogonal momentum conservation equation, equation (3.10) i.e.

$$\int_V \vec{\nabla} \cdot \vec{J}(\phi)\, dV = \int_A \vec{J}(\phi) \cdot \vec{n}\, dA = \int_V S(\phi)\, dV \qquad \text{(A. 1)}$$

over time and volume the flux vector is approximated as per equation (3.11) i.e.

$$\int_A \vec{J}(\phi) \cdot \vec{n}\, dA = \sum_{n=1}^{6} \vec{J}(\phi) \cdot \vec{n}\, A_n = \sum_{n=1}^{6} J_n^{\xi}(\phi)\, A_n^{\xi} \qquad \text{(A. 2)}$$

where

$$J_n^{\xi} = \rho_n V_n^{\xi} \phi_n + \Gamma_n \nabla \phi_n \qquad \text{(A. 3)}$$

The interfacial transported variable ϕ_n in the convection term of equation (A.3) is substituted with the flux blended interpolation formula given by equation (3.6) i.e.

$$\phi_n = \left[\left|V_n^{\xi};0.0\right|\right] \frac{1}{V_n^{\xi}} \phi_N + \left[\left|-V_n^{\xi};0.0\right|\right] \frac{1}{-V_n^{\xi}} \phi_{NN} + S_2 \qquad \text{(A. 4)}$$

Furthermore, the diffusion term in equation (A.3) is substituted with an approximation for the interfacial diffusion given by equation (3.13). After these substitutions equation (A.3) may be written as

$$J_n^{\xi} = \left[\rho_n V_n^{\xi} \left(\left[\left|V_n^{\xi};0.0\right|\right] \frac{1}{V_n^{\xi}} \phi_N + \left[\left|-V_n^{\xi};0.0\right|\right] \frac{1}{-V_n^{\xi}} \phi_{NN} + S_2 \right) - \Gamma_n \frac{\phi_{NN} - \phi_N}{d\xi} \right] \qquad \text{(A. 5)}$$

by grouping terms

$$J_n^{\xi} = \left[\left|Pe_n;0.0\right|\right] \frac{\Gamma_n}{d\xi} \phi_N - \left[\left|-Pe_n;0.0\right|\right] \frac{\Gamma_n}{d\xi} \phi_{NN} + \rho_n V_n^{\xi} S_2 - \Gamma_n \frac{\phi_{NN} - \phi_N}{d\xi} \qquad \text{(A. 6)}$$

By employing an artificial addition and subtraction one finds

$$J_n^{\xi} = \left(\left[|Pe_n;0.0|\right]+1.0\right)\frac{\Gamma_n}{d\xi}\phi_N + \overbrace{\left(-\left(\left[|-Pe_n;0.0|\right]+1.0\right)\frac{\Gamma_n}{d\xi}\phi_N + \left(\left[|-Pe_n;0.0|\right]+1.0\right)\frac{\Gamma_n}{d\xi}\phi_N\right)}^{\text{artificial subtraction and addition}}$$

$$-\left(\left[|-Pe_n;0.0|\right]+1.0\right)\frac{\Gamma_n}{d\xi}\phi_{NN} + \rho_n V_n^{\xi} S_2 \qquad \text{(A. 7)}$$

and since

$$\left[\left(\left[|Pe_n;0.0|\right]+1.0\right)-\left(\left[|-Pe_n;0.0|\right]+1.0\right)\right]\frac{\Gamma_n}{d\xi}\phi_N = \rho_n V_n^{\xi}\phi_N$$

one may re-write equation (A.7) as

$$J_n^{\xi} = \left(\left[|-Pe_n;0.0|\right]+1.0\right)\frac{\Gamma_n}{d\xi}\left(\phi_N - \phi_{NN}\right) + \rho_n V_n^{\xi}\phi_N + \rho_n V_n^{\xi} S_2 \qquad \text{(A. 8)}$$

Equation (A.8) is now the same as given by equation (3.14).When equation (A.8) is summed over the six faces of the hexahedral control volume one may assume that for the converged solution the continuity "like" term, $\sum_{n=1}^{6}\left(\rho_n V_n^{\xi} A_n^{\xi}\right)\phi_N$, disappears.

By combining equation (A.8) and equation (A.1) i.e.

$$\sum_{n=1}^{6}\left(\left[|-Pe_n;0.0|\right]+1.0\right)\frac{\Gamma_n}{d\xi}\phi_N A_n^{\xi} + \sum\left(\left[|-Pe_n;0.0|\right]+1.0\right)\frac{\Gamma_n}{d\xi}\phi_{NN} A_n^{\xi} + \rho_n V_n^{\xi} S_2 \qquad \text{(A. 9)}$$

and grouping terms one finds

$$a_N \phi_N = \sum_{n=1}^{6} a_{NN} \phi_{NN} + S_1 + S_2 \qquad \text{(A. 10)}$$

where

$$a_{NN} = \frac{\Gamma_n}{d\xi}\left(\left[\left|-Pe_n;0.0\right|\right] + 1.0\right) A_n^{\xi} \qquad \text{(A. 11)}$$

$$a_N = \sum_{n=1}^{6} a_{NN} \qquad \text{(A. 12)}$$

and where the primary and secondary source terms are S_1 and S_2 respectively.

APPENDIX B

DERIVATION OF THE NON-ORTHOGONAL PROJECTION EQUATIONS

The solution of the governing equations requires the approximation of the orthogonal global Cartesian gradients ($\frac{\partial \phi}{\partial x^i}$) of a transported scalar (ϕ) in terms of local non-orthogonal gradients. These local non-orthogonal gradients may be written by means of the chain rule in terms of orthogonal gradient contributions i.e.

$$\frac{\partial \phi}{\partial \xi} = \frac{\partial x}{\partial \xi}\frac{\partial \phi}{\partial x} + \frac{\partial y}{\partial \xi}\frac{\partial \phi}{\partial y} + \frac{\partial z}{\partial \xi}\frac{\partial \phi}{\partial z} \tag{B. 1}$$

$$\frac{\partial \phi}{\partial \zeta} = \frac{\partial x}{\partial \zeta}\frac{\partial \phi}{\partial x} + \frac{\partial y}{\partial \zeta}\frac{\partial \phi}{\partial y} + \frac{\partial z}{\partial \zeta}\frac{\partial \phi}{\partial z} \tag{B. 2}$$

$$\frac{\partial \phi}{\partial \eta} = \frac{\partial x}{\partial \eta}\frac{\partial \phi}{\partial x} + \frac{\partial y}{\partial \eta}\frac{\partial \phi}{\partial y} + \frac{\partial z}{\partial \eta}\frac{\partial \phi}{\partial z} \tag{B. 3}$$

where the local non-orthogonal coordinate system is denoted by (ξ, ζ, η). In tensor form equations (B.1) to (B.3) may be written as

$$\frac{\partial \phi}{\partial \xi^i} = \frac{\partial x^j}{\partial \xi^i}\frac{\partial \phi}{\partial x^j} \tag{B. 4}$$

The set of linear equations represented by equation (B.4) may also be written as

$$\frac{\partial \phi}{\partial \xi^i} = J^j_i \frac{\partial \phi}{\partial x^j} \tag{B. 5}$$

where J^i_j is the Jacobian matrix $\frac{\partial x^i}{\partial \xi^j}$ with the i and j indexes denoting matrix columns and rows respectively. Since the Jacobian matrix is square and the Jacobian determinant is non-zero one may prove from linear algebra, Greenberg (1998), that a unique solution,

$$\frac{\partial \phi}{\partial x^i} = \left(J^{-1}\right)_i^j \frac{\partial \phi}{\partial \xi^j} \tag{B. 6}$$

exists.

Equation (B.6) is easily simplified by employing Cramer's rule i.e.

$$\frac{\partial \phi}{\partial x^i} = \frac{\sum_j J_i^j \frac{\partial \phi}{\partial \xi^j}}{|J|} \tag{B. 7}$$

where the $|J| = \det\left(J_j^i\right)$ is the Jacobian determinant found by cofactor expansion as

$$|J| = \frac{\partial x}{\partial \xi}\left(\frac{\partial y}{\partial \zeta}\frac{\partial z}{\partial \eta} - \frac{\partial z}{\partial \zeta}\frac{\partial y}{\partial \eta}\right) + \frac{\partial x}{\partial \zeta}\left(\frac{\partial z}{\partial \xi}\frac{\partial y}{\partial \eta} - \frac{\partial y}{\partial \xi}\frac{\partial z}{\partial \eta}\right) + \frac{\partial x}{\partial \eta}\left(\frac{\partial y}{\partial \xi}\frac{\partial z}{\partial \zeta} - \frac{\partial z}{\partial \xi}\frac{\partial y}{\partial \zeta}\right) \tag{B. 8}$$

Thus all the global Cartesian gradients required so solve the governing equations may be found only in terms of approximations of local non-orthogonal gradients by employing equations (B.7) and (B.8).

APPENDIX C

AVERAGING OF PRIMARY FIELD VARIABLES

The primary variables found from the field solution of the governing equations need to be averaged to evaluate the results properly.

The average fluid velocity across an interface is found from

$$V_m = \frac{\dot{m}}{A_c \rho} = \frac{\int_{A_c} \rho u_c dA_c}{A_c \rho} \approx \frac{\sum_n V_n^{\xi} A_n}{A_c} \qquad \text{(C. 1)}$$

The average or bulk fluid temperature is found from the average thermal energy state of the fluid across the interface, Kays and Crawford (1993) i.e.

$$T_m = \frac{\int_{A_c} T_c \rho u_c C_p dA_c}{\dot{m} C_p} = \frac{\int_{A_c} T_c u_c dA_c}{\int_{A_c} u_c A_c} \approx \frac{\sum_n T_n V_n^{\xi} A_n^{\xi}}{\sum_n V_n^{\xi} A_n^{\xi}} \qquad \text{(C. 2)}$$

where u_c is the flow normal to the interface, T_c is the temperature at the interface, A_c is the cross sectional interfacial area, $\dot{m}$ is the mass flux crossing the interface and n is the interface numbering index.

The average pressure is also found from the energy flux crossing the interface i.e.

$$p_m = \frac{\int_{A_c} p_c u_c dA_c}{V_m A_c} \approx \frac{\sum_n p_n V_n^{\xi} A_n^{\xi}}{\sum_n V_n^{\xi} A_n^{\xi}} \qquad \text{(C. 3)}$$

where p_n is the control volume interfacial pressure.

APPENDIX D

DERIVATION OF AN APPROXIMATE EXPLICIT FORMULATION OF THE SHEAR VELOCITY FROM THE LOGARITHMIC LAW FOR THE VELOCITY DISTRIBUTION IN TURBULENT FLOWS.

The logarithmic law for the turbulent velocity distribution, equation (6.16), may be rewritten as

$$\frac{u_c(r)}{u_\tau} = \frac{1}{\kappa}\ln(Ey^+) \tag{D. 1}$$

where

$$y^+ = \frac{u_\tau y}{\nu} \tag{D. 2}$$

with the centreline velocity given by $u_c(r)$ at distance $y = H/2$. Thus one may find the shear velocity, u_τ, from the implicit equation (D.1) if the centreline velocity and the centreline height is known. By substituting the function

$$x = \frac{1}{u_\tau} \tag{D. 3}$$

into equation (D.1) one finds after some algebra a new relation

$$x \cdot e^{P(r)x} - Z = 0 = k(x) \tag{D. 4}$$

where

$$P(r) = u_c(r) \cdot \kappa \tag{D. 5}$$

and

$$Z = \frac{Ey}{\nu} \tag{D. 6}$$

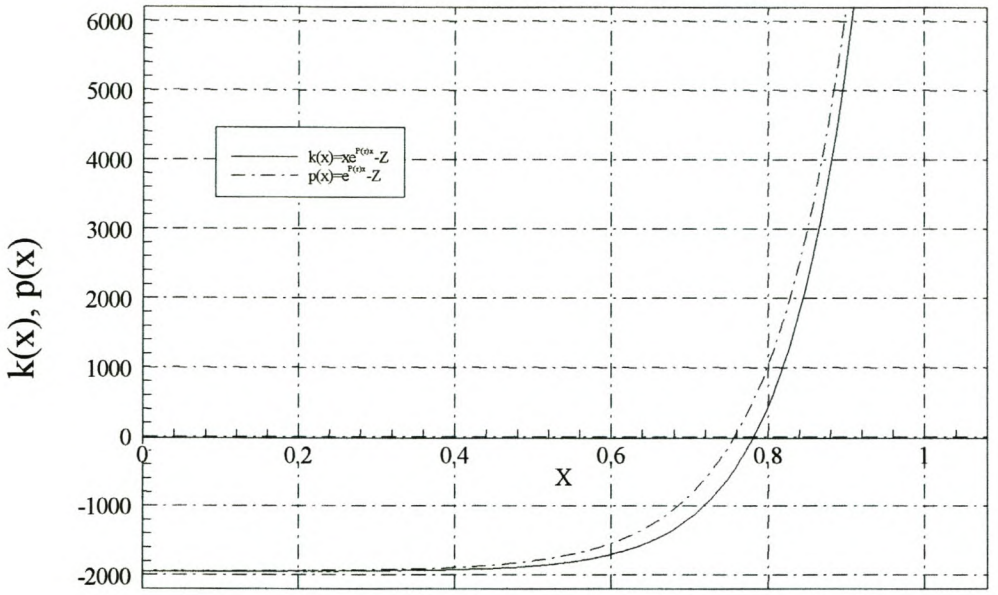

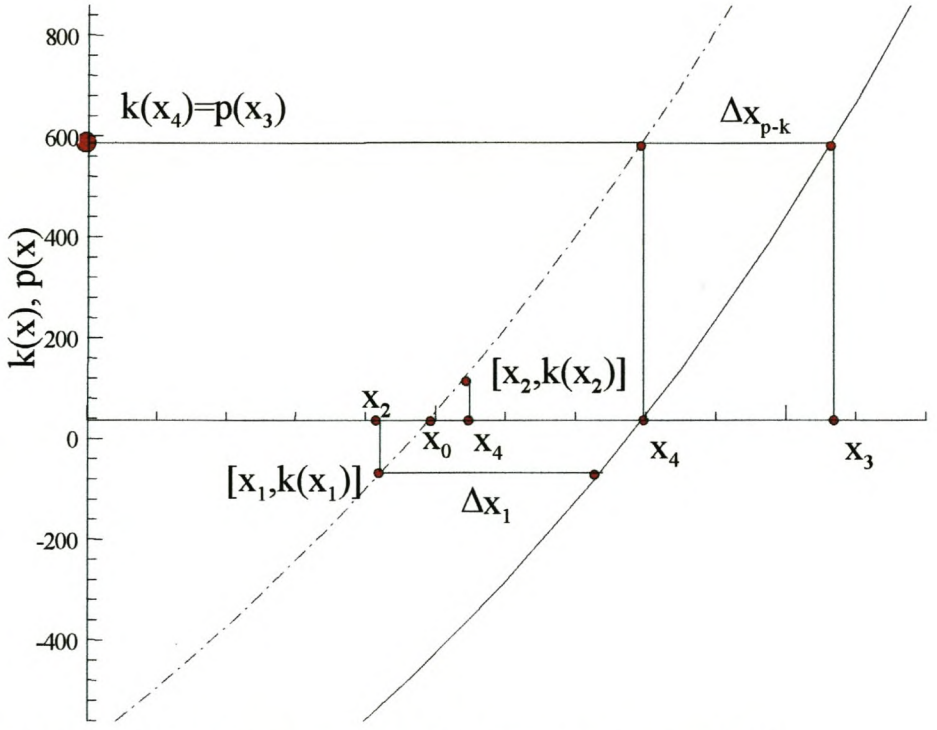

Figure D.1. Schematic diagram showing functions k(x) and p(x).

Thus the root, x_0, of $k(x_0)$ equals the inverse of the shear velocity. See figure D.1. A similar yet simpler equation

$$p(x) = e^{P(r)x} - Z \tag{D. 7}$$

yields its root, $p(x_1)=0$, at

$$x_4 = \frac{\ln(Z)}{P(r)} \tag{D. 8}$$

Substituting equation (D.8) into (D.4) one finds

$$k(x_4) = x_4 e^{P(r)x_4} - Z \tag{D. 9}$$

Setting equation (D.9) equal to equation (D.7) yields

$$x_3 = \frac{\ln\left(x_4 e^{P(r)x_4}\right)}{P(r)} \tag{D. 10}$$

Now, to find the difference in x-values where equation (D.7) equals (D.4) we have

$$p(x_p) - k(x_k) = 0 \tag{D. 11}$$

and after some algebra

$$\Delta x_{p-k} = \frac{\ln(x_k)}{P(r)} \tag{D. 12}$$

From equation (D.12) it is evident that the value

$$x_1 = x_4 - (x_3 - x_4) = 2x_4 - x_3$$

$$= \frac{\ln\left[\frac{ZP(r)}{\ln(Z)}\right]}{P(r)} \qquad \text{(D. 13)}$$

is near but not equal to the root, x_0, of equation (D.4). The actual difference in x value between p(x) and k(x) at x_1 may be found from equation (D.12) i.e.

$$\Delta x_1 = \frac{\ln(x_1)}{P(r)} = \frac{1}{P(r)} \ln\left[\frac{\ln\left(\frac{ZP(r)}{\ln(Z)}\right)}{P(r)}\right] \qquad \text{(D. 14)}$$

Using equation (D.14) one will again find that another x-value

$$x_2 = x_4 - \Delta x_1$$

$$= \frac{1}{P(r)}\left(\ln(Z) - \ln(x_1)\right) \qquad \text{(D. 15)}$$

will yield a value also near the root, x_0, of equation (D.4) but not equal to x_1. Since we now have 2 coordinates, $[x_1,k(x_1)]$ and $[x_2,k(x_2)]$, near the root, $[x_0,k(x_0)]$, we find that a straight line fit between the two coordinates yields at root of the straight line at

$$x_0 \approx \frac{-\left(x_1 e^{P(r)x_1} - Z\right)(x_1 - x_2)}{\left(x_1 e^{P(r)x_1} - x_2 e^{P(r)x_2}\right)} + x_1 \qquad \text{(D. 16)}$$

which in turn gives a good explicit approximation of the shear velocity from equation (D.3).

REFERENCES

Burns, A.D. Wilkes, N.S., (1987) A Finite Difference Method for the Computation of Fluid Flows in Complex Three Dimensional Geometries, Oxfordshire, U.K.: Harwell Laboratory, AERE R 12342, pp. 1-30.

Chien, K.Y. (1982) Predictions of channel and boundary-layer flows with low-Reynolds-number turbulence model, AIAA Journal, vol. 20, no. 1, pp. 33-38.

Comini, G. and Del Guidice, S. (1985) A (k-ε) model of turbulent flow, Numerical Heat Transfer, vol. 8, pp. 133-147.

Comte-Bellot, G. (1965) Ecoulement turbulent entre deux parois paralleles, Publications Scientifique et Technique Du Ministere de l'Air, no. 419.

Deisler, R.G. (1955) Turbulent heat transfer and friction in the entrance regions of smooth passages, Transactions of the ASME, November, pp.1221-1233

Du Plessis, J.P. and Collins, M.R. (1992) A new definition for laminar flow entrance lengths of straight ducts, South African Institution of Mechanical Engineers R + D Journal, pp. 11-16.

Duffie, J.A., and Beckman, W.A (1991) Solar Engineering of Thermal Processes, 2nd ed., New York: John Wiley & Sons.

Ferziger, J.H. and Perić, M. (1996) Computational Methods for Fluid Dynamics, 1st ed., Berlin: Springer-Verlag.

Frederick, D and Chang, T.S. (1972) Continuum Mechanics, 1st ed., Cambridge: Scientific Publishers, Inc.

Gannon, A.J. and von Backström, T.W. (2000) Solar chimney cycle analysis with system losses and solar collector performance, Proceedings International Conference on Applied Mechanics, pp. 403-410.

Greenberg, M.D. (1998) Advanced Engineering Mathematics, 2nd ed., New Jersey: Prentice-Hall.

Haaf, W. (1984) Part II: Preliminary test results from the Manzanares pilot plant, Int. J. Solar Energy, vol. 2, pp. 141-161.

Haaf, W., Friedrich, K., Mayer, G. and Schlaich, J. (1983) Part I: Principle and construction of the pilot plant in Manzanares, Int. J. Solar Energy, vol. 2, pp. 3-20.

Haaland, S.E. (1983) Simple and explicit formulas for the friction factor in turbulent pipe flow, Trans. ASME J. Fluid Engineering, vol. 105, no. 3, pp. 89-90.

Han, L.S. (1960) Hydrodynamic entrance lengths for incompressible laminar flow in rectangular ducts, Journal of Applied Mechanics, September, pp. 403-409.

Harms, T.M. (1995) A finite volume method for the analysis of flow fields with complex boundaries, Ph.D thesis, University of Stellenbosch, Stellenbosch, South Africa.

Harms, T.M., von Backström, T.W. and du Plessis, J.P. (1997) Comparison of three finite-volume interpolation schemes, R&D Journal, vol. 13(1), pp. 20-30.

Hausen, H. (1974) Extended equation for heat transfer in tubes at turbulent flow, Wärme und stoffübertragung, vol. 7, pp. 222-225.

Henkes, R.A.W.M. (1998) Scaling of turbulent boundary layer along flat plate according to different turbulence models, Int. J. of Heat and Fluid Flow, vol. 19, pp. 338-347.

Jasak, H. (1996) Error analysis and estimation for the finite volume method with applications to fluid flows, Ph.D thesis, University of London, London, United Kingdom.

Kays, W.M. and Crawford, M.E. (1993) Convective heat and mass transfer, 3rd ed., New York, McGraw-Hill.

Khosla, P.K. and Rubin, S.G. (1974) A diagonally dominant second-order accurate implicit scheme, Computer and Fluids, vol. 2, pp. 207-209.

Kreyzig, E. (1988) Advanced engineering mathematics, 6th ed., New York, Wiley.

Kröger, D.G. (1998) Air cooled heat exchangers and cooling towers, 1st ed., Begell House, New York.

Kröger, D.G. and Buys, J.D. (1999) Radial flow boundary layer development analysis, R&D Journal, vol. 9, no. 3, pp.95-102.

Lakehal, D. (1999) Computation of turbulent shear flows over rough-walled circular cylinders, J. of Wind Engineering and Industrial Aerodynamics, vol. 80, pp. 47-88

Launder, B.E. and Spalding, D.B. (1974) The numerical computation of turbulent flows, Computer Methods in Applied Mechanics and Engineering, vol. 3, pp. 269-289.

Leister, H.J. and Perić, M. (1994) Vectorized strongly implicit solving procedure for a seven-diagonal coefficient matrix, Int. J. Num. Meth Heat Fluid Flow, vol. 4, pp. 159-172.

Mohammadi, B., and Pironneau, O. (1994) Analysis of the k-epsilon turbulence model, Research in Applied Mathematics, Paris: Masson and Chichester, John Wiley and Sons.

Nikuradse, J. (1933) Strömungsgesetze in rauhen rohren, Forsch.Arb.Ing.-Wes, no. 361.

Nisizima, S. and Yoshizawa, A. (1986) Turbulent channel and couette flows using anisotropic $k-\varepsilon$ model, AIAA Journal, vol. 25, no. 3, pp. 414-420.

Patankar, S.V. and Spalding, D.B. (1972) A calculation procedure for heat, mass and momentum transfer in three-dimensional flows. Int. Journal Heat Mass Transfer, vol. 15, pp. 1787-1806.

Patankar, S.V. (1980) Numerical Heat Transfer and Fluid Flow, 1st ed., Washington: Hemisphere.

Perić, M. (1985) A finite volume method for the prediction of three-dimensional fluid flow in complex ducts, Ph.D thesis, University of London, London, United Kingdom.

Prandtl, L. (1925) Uber ein ausgebildete Turbulenz, ZAMM, vol. 5, pp. 136-139.

Reynolds, O. (1874) On the Extent and Action of the Heating Surfaces for Steam Boilers, Manchester Lit. Phil. Soc., vol. 14, pp.7-12.

Rhie, C.M. and Chow, W.L. (1983) Numerical study of turbulent flow past an airfoil with trailing edge separation, AIAA Journal, no, 11, pp. 1525-1532.

Rohsenow, W.M., and Choi, H.Y. (1961) Heat, Mass and Momentum transfer, 1st ed, New Jersey, Prentice-Hall.

Rohsenow, W.M., Hartnett, J.P. and Ganic, E.N. (1985) Handbook of heat transfer fundamentals, Revised ed., New York, McGraw-Hill.

Sajjadi, S.G. and Waywell, M.N. (1997) Application of roughness-dependent boundary conditions to turbulent oscillatory flows, Int. J. of Heat and Fluid Flow, vol. 18, pp. 368-375.

Sajjadi S.G. and Aldridge, J.N. (1995) Prediction of turbulent flow over rough asymmetrical bed forms, Appl. Math. Modeling, vol. 19, pp. 139-152

Sarkar, A. and So, R.M.C. (1997) A critical evaluation of near-wall two-equation models against direct numerical simulation data, Int. J. Heat and Fluid Flow, vol. 18, no. 2, pp.197-208.

Schlaich, J. (1995) The solar chimney – electricity from the sun, 1st ed., Stuttgart: Axel Menges.

Schlichting, H. (1968) Boundary layer theory, 6th ed., New York: McGraw-Hill Book Company.

Shah, R. K. and London, A. L. (1978) Laminar flow forced convection in ducts, New York: Academic.

So, R.M.C. Zhang, H.S. and Speziale, C.G. (1991) Near-wall modeling of the dissipation rate equation, AIAA Journal, vol. 29, no. 12, pp. 2069-2076.

Stephan, K. (1959) Wärmeübergang und Druckabfall bei nicht ausgebildeter Laminarströmung in Rohren und in ebenen Spalten, Chem.-Ing.-Techn., vol. 31, pp. 773-778.

Stephenson, P. L. (1976) A theoretical study of heat transfer in two-dimensional turbulent flow in a circular pipe and between parallel and diverging plates, Int. J. Heat Mass Transfer, vol. 19, pp. 413-423.

Stone, H.L. (1968) Iterative solution of implicit approximations of multidimensional partial differential equations, SIAM Journal for Numerical Analysis, vol. 5, no. 3, pp. 530-558.

Thiart, G.D. (1990) A numerical procedure for predicting the effects of distorted inflow conditions on the performance of axial flow fans, Ph.D. thesis, University of Stellenbosch, Stellenbosch, South Africa.

Thiart, G.D. (1998) Kursusnotas vir Gevorderde Vloeidinamika 874, Universiteit van Stellenbosch, Stellenbosch, Suid-Afrika.

Timin, T. and Esmail, N. (1983) A comparative study of central and upwind difference schemes using the primitive variables, Int. J. for Numerical Methods in Fluids, vol. 3, pp. 295-305.

Ubbink, O. (1997) Numerical prediction of two fluid systems with sharp interfaces, Ph.D thesis, University of London, London, United Kingdom.

Von Backström, T.W. (1999) Presentation on the solar chimney cycle analysis, University of Stellenbosch, Stellenbosch, South Africa.

White, F.M. (1991) Viscous Fluid Flow, 2nd ed., New York: McGraw-Hill.

White, F.M. (1994) Fluid Mechanics, 3rd ed, New York: McGraw-Hill.

Wilcox, D.C. (1994) Turbulence modeling for CFD, 1st ed., California: DCW Industries.

Yoon, J.Y. and Patel, V.C. (1996) Numerical model of turbulent flow over sand dune, J. of Hydraulic Engineering, vol. 122, no. 1, pp. 10-18.

Yoon, J.Y., Patel, V.C. and Ettema, R. (1996) Numerical model of flow in ice-covered channel, J. of Hydraulic Engineering, vol. 122, no. 1, pp. 19-26.

BIBLIOGRAPHY

Bernard, P.S. (1986) Limitations of the near-wall k-ε turbulence model, AIAA Journal, vol. 24, no. 4, pp. 619-622.

Biringen, S. and Cook, C. (1988) On pressure boundary conditions for the incompressible Navier-Stokes equations using non-staggered grids, Numerical Heat Transfer, vol. 13, pp. 241-252.

Bredell, M. (1998) Berekenings vloei meganika, element ontwerp, B. Ing. Skripsie, Universiteit van Stellenbosch, Stellenbosch, Suid-Afrika.

Bückle, U. and Peric, M. (1992) Numerical simulation of buoyant and thermo-capillary convection in a square cavity, Numerical Heat Transfer, pt. A vol. 21, pp. 121-141.

Caretto, L.S., Gosman, A.D., Patankar, S.V. and Spalding, D.B. (1972) Two calculation procedures for steady, three-dimensional flows with recirculation, Proceedings of the 3rd International Conference on Numerical Methods in Fluid Dynamics, Springer-Verlag, pp. 60-68.

Choi, S.K. and Chen, C.J. (1991) Navier-Stokes solution of complete turbulent flow past finite axisymmetric bodies, AIAA Journal, vol. 29, no. 6, pp. 998-1001.

Chui, E.H. and Raithby. G.D. (1993) Computation of radiant heat transfer on a nonorthogonal mesh using the finite-volume method, Numerical Heat Transfer, part B, vol. 23, pp. 269-288.

Demirdzic', I., Lilek, Z. and Peric', M. (1992) Fluid flow and heat transfer test problems for non-orthogonal grids: bench-mark solutions, International Journal for Numerical Methods in Fluids, vol. 15, pp. 329-354.

Demirdzic', I., Gosman, A.D., Issa., R.I. and Peric', M. (1987) A calculation procedure for turbulent flow in complex geometries, Computers and Fluids, vol. 15, no.3, pp. 251-273.

Elkaim, D., Reggio, M. and Camarero, R. (1992) Simulating two-dimensional turbulent flow by using the k-ε model and the vorticity-streamfunction formulation, International Journal for Numerical Methods in Fluids, vol. 14, pp. 961-980.

Ellis, T.M.R. (1982) A structured approach to FORTRAN 77 programming, 1st ed., London: Addison-Wesley.

Gauthier, C., Lacroix, M. and Bernier, H. (1997) Numerical simulation of soil heat exchanger-storage systems for greenhouses, Solar Energy, vol. 60, no. 6, pp. 333-346.

Goyal, R.K. and Tiwari, G.N. (1996) Parametric study of a reverse flat plate absorber cabinet dryer: a new concept, Solar Energy, vol. 60, no. 1, pp. 41-48.

Han, L.S. (1960) Hydrodynamic entrance lengths for incompressible laminar flow in rectangular ducts, Journal of Applied Mechanics, September, pp. 403-409.

Harlow, F.H. and Welch, J.E. (1965) Numerical calculations of time-dependant viscous incompressible flow of fluid with free surface, The Physics of Fluids, vol. 8, no. 12, pp. 2182-2189.

Hattersley, L. (1999), Electric dreams, New Scientist, 6 March, pp. 30-33.

Huang, P.G., Launder, B.E. and Leschziner, M.A. (1985) Discretization of non-linear convection processes: A broad range comparison of four schemes. Computer Methods in Applied Mechanics and Engineering, vol. 48, pp. 1-24.

Jaluria, Y and Torrance, K.E. (1986) Computational heat transfer, 1st ed., Berlin, Springer-Verlag.

Jannot, Y. and Coulibaly, Y. (1997) Radiative heat transfer in a solar air heater covered with a plastic film, Solar Energy, vol. 60, no. 1, pp. 35-40.

Kotake, S. and Hijikata, K (1993) Numerical simulation of heat transfer and fluid flow, 1st ed., Amsterdam, Elsevier.

Majumdar, S. (1988) Role of underrelaxation in momentum interpolation for calculation of flow with nonstaggered grids, Numerical Heat Transfer, vol. 13, pp 125-132.

Maliska, C.R. and Raithby, G.D. (1984) A method for computing three dimensional flows using non-orthogonal boundary fitted coordinates, International Journal for Numerical Methods in Fluids, vol. 4, pp. 519-537.

Metais, B. and Eckert, E.R.G. (1964) Forced, mixed and free convection regimes, J. Heat Transfer, vol. 86, pp. 295-296.

Mihalakakou, G., Santamouris, M., Lewis, J.O. and Asimakopoulos, D.N. (1997) On application of the energy balance equation to predict ground temperature profiles, Solar Energy, vol. 60, no. 4-3, pp. 181-190.

Mohamad, A.A. (1997) High efficiency solar heater, Solar Energy, vol. 60, no. 2, pp. 71-76.

Noll, B. and Wittig, S. (1991) Generalized conjugate gradient method for the efficient solution of three-dimensional fluid flow properties, Numerical Heat Transfer, vol. 20. Pp. 207-221.

Ong, K.S., (1995) Thermal performance of solar air heaters: Mathematical procedure and solution procedure, Solar Energy, vol 55, no. 2, pp 93-109.

Perić, M. (1987) Efficient semi-implicit solving algorithm for nine-diagonal coefficient matrix, Numerical Heat Transfer, vol. 11, no. 3, pp. 251-279.

Poulikakos, D. (1994) Conduction Heat Transfer, 1st ed, New-Jersey, Prentice-Hall

Pulliam, T.H. (1986) Artificial Dissipation Models for the Euler Equation, AIAA Journal, vol. 24, no. 12, pp. 1931-1940.

Ratti, C. and Mujumdar, A.S. (1997) Solar drying of foods: modeling and numerical simulation, Solar Energy, vol. 60, no. 3-4, pp. 151-157.

Reuss, M., Beck, M. and Mueller, J.P. (1997) Design of a seasonal thermal energy storage in the ground, Solar Energy, vol. 59, no. 4-6, pp. 247-257.

Schlaich, J. (1991) World energy demand, population explosion and pollution: could solar energy utilisation become a solution, The Structural Engineer, vol. 69, no. 10, pp. 189-192.

Siegel, R. (1960) Heat transfer for laminar flow in ducts with arbitrary time variations in wall temperature, Journal of Applied Mechanics, June, pp. 241-249

Spalart, P.R. (1988) Direct simulation of a turbulent boundary layer up to $Re_\theta = 1410$, J. Fluid. Mech., vol. 187, pp. 61-98.

Spalding, D.B. (1972) A novel finite difference formulation for differential expressions involving both first and second derivatives, Int. J. for Numerical Methods in Engineering, vol. 4, pp. 551-559.

Stinnes, W.W. (1998) Presentation on the solar chimney development in South Africa, University of Stellenbosch, Stellenbosch, South Africa.

Thomas, L.H. (1945) Elliptic Problems in Linear Difference Equations of a Network, Watson Science Computer Laboratory Report, Columbia University, New York, as quoted by Anderson et al. (1984) - unobtainable.

Thompson, J.F., Warsi, Z.U.A. and Wayne Mastin, C. (1985) Numerical Grid Generation, 1st ed. New York: North-Holland.

Van Doormaal, J.P. and Raithby, G.D. (1984) Enhancements of the SIMPLE method for predicting incompressible fluid flows, Numerical Heat Transfer, vol. 7, pp. 147-163